The Effects of Supersymmetric Particle Decays and Annihilations on Big-Bang Nucleosynthesis

A DISSERTATION
SUBMITTED TO THE FACULTY OF THE GRADUATE SCHOOL
OF THE UNIVERSITY OF MINNESOTA
BY

Feng Luo

IN PARTIAL FULFILLMENT OF THE REQUIREMENTS
FOR THE DEGREE OF
Doctor of Philosophy

Advisor: Keith A. Olive

August, 2012

Acknowledgements

My deepest gratitude is to my advisor, Keith Olive. His intuition and passion on physics, and his insistence on the correctness of research, made him a perfect model I should follow. I can feel his wisdom in each of our conversation, and I hope I have caught some of it in the past five years, although I am sure I will still have a lot to learn from him even if I would stay another five years in graduate school. Fortunately, there is Skype, and I think I will take every chance to talk to him when we meet in conferences.

I would like to thank my committee, who give me valuable suggestions on my oral and final exam, and help me to identify my shortage in physics.

I would like to thank my collaborators. This thesis would not have been possible without them.

I thank all my professors and friends, who have taught me, supported me, and helped me in various occasions. They made my years here so memorable.

I thank all the people in the FTPI, where I hear jokes, enjoy cookies, and get advice on both academics and life.

Finally, I thank my parents, for their endless support, love and care. I thank my fiancée, Xiaoyi, for being my sole-mate, loving me unconditionally, and helping me to be a better person.

The research conducted which leads to this thesis was supported in part by DOE grant DE–FG02–94ER–40823 at the University of Minnesota, Physics Department Fellowship and Doctoral Dissertation Fellowship.

Abstract

Many extensions of the Standard Model of particle physics predict the existence of massive unstable or metastable particles. If the Standard Model secondaries induced by the decays of these particles have not been thermalized by the background cosmic plasma before the start of Big-Bang nucleosynthesis (BBN), the decay showers may alter the primordial abundances of the light elements through non-thermal electromagnetic and hadronic interactions with the background nuclei. The concordance of the BBN predictions and observations can thus constrain the abundance, lifetime and decay spectra of the decaying particle. On the other hand, the decays of heavy particles may help drive the concordance in a favorable direction. In particular, depending on the analysis of the observational data adopted, there is a factor of $2-4$, or $4-5\sigma$ discrepancy between the predicted and observationally inferred primordial ^{7}Li abundance, and this is known as the '^{7}Li problem'.

We study the effects on the light-element abundances of the decays of massive gravitinos in neutralino dark matter scenarios within the constrained minimal supersymmetric extension of the Standard Model (CMSSM). When the ^{7}Li constraint is disregarded, for discrete choice of the gravitino mass, we present upper limits on the gravitino abundance for CMSSM parameters along the WMAP strips where the lightest neutralino provides all of the cold dark matter. For some CMSSM benchmark points, we explore the possibility of the effects of the decays of gravitinos as a solution to the ^{7}Li problem, and we find a narrow range for the gravitino mass and abundance where the ^{7}Li problem is alleviated or even marginally solved.

We consider the effects of uncertainties in nuclear reaction rates on the cosmological constraints on the decays of massive particles during or after BBN. We identify the nuclear reactions due to non-thermal hadrons that are the most important in perturbing standard BBN, then quantify the uncertainties in these reactions and in the resulting light-element abundances. Applying this analysis to models with unstable gravitinos decaying into neutralinos, we calculate the likelihood function for the light-element abundances measured currently, taking into account the current experimental errors in the determinations of the relevant nuclear reaction rates. We find a region of the

gravitino mass and abundance in which the abundances of deuterium, ^{4}He and ^{7}Li may be fit with $\chi^2 = 5.5$, compared with $\chi^2 = 31.7$ if the effects of gravitino decays are unimportant. The best-fit solution is improved to $\chi^2 \sim 2.0$ when the lithium abundance is taken from globular cluster data.

We also study the effects of the residual late-time dark matter particle annihilations during and after BBN on the predicted cosmological abundances of the light elements. Within the CMSSM and its one or two more parameter extensions, with a neutralino lightest supersymmetric particle (LSP), we find negligible effects on the abundances of deuterium, ^{3}He, ^{4}He and ^{7}Li predicted by homogeneous BBN, but potentially a large enhancement in the predicted abundance of ^{6}Li.

Contents

List of Tables

List of Figures

Chapter 1

Introduction

The Standard Model of particle physics (SM), augmented by neutrino masses, has been remarkably successful at describing phenomena at or below the weak scale. However, we know it cannot be the final story of particle physics. In addition to the primary theoretical motivations, namely, resolving the hierarchy problem [1] and unifying the gauge couplings [2], to explain the existence of dark matter, which makes up approximately one quarter of the energy density of the universe [3] and for which evidence is available from a wide range of observation data [4, 5, 6] (see [7] for a review), requires that we go beyond the Standard Model.

One of the best available candidates for physics beyond the Standard Model is supersymmetry (SUSY) (for reviews, see, e.g., [8] - [15]). It transforms bosons into fermions and vice versa, and such a 'boson $\leftrightarrow$ fermion' symmetry provides exactly the necessary condition to resolve the hierarchy problem. Its minimal version, namely, the minimal supersymmetric extension of the Standard Model (MSSM), provides the right numbers and types of particles to achieve the unification of gauge couplings. Moreover, by imposing a discrete symmetry called R-parity so that the interaction terms which lead to unacceptable large proton decay rate are excluded, the MSSM predicts that the lightest supersymmetric particle (LSP) is absolutely stable, and if the LSP is color and electrically neutral, it can be a promising candidate of dark matter particle. Indeed, many ground-based and satellite-based experiments are searching for these dark matter particles, and at the same time, people are also looking for signals of supersymmetry in particle accelerators [16].

Besides helping to solve the dark matter problem, supersymmetry has other important implications in cosmology. One of the prominent achievements of the Big Bang model is that it offers an explanation of the origin of the light elements. In a process called Big-Bang nucleosynthesis (BBN) [17] which happened during the first several minutes after the Big Bang (corresponding to temperature scales between ~ 1 MeV to ~ 0.1 MeV), protons combined with neutrons to form mostly helium, deuterium and lithium. Apart from the input nuclear cross sections, the standard BBN theory contains only a single parameter, namely the baryon-to-photon ratio, η, and even that has been fixed by the measurement of fluctuations in the cosmic microwave background radiation (CMB) [3]. It is quite impressive that the overall agreement on the abundances of the light elements between the essentially parameter-free BBN theoretical predictions and the values inferred from astronomical observations is valid for the various light elements with the abundances of which span nine orders of magnitude – from ^{4}He/H ~ 0.08 down to ^{7}Li/H $\sim 10^{-10}$ (ratios by number), and this concordance makes BBN one of the cornerstones of the Big Bang model [18, 19].

BBN predictions of the light-element abundances are based on Standard Model calculation, therefore good concordance between the theories and observations may potentially put strong constraints on any new particle physics theory beyond the Standard Model.

Many extensions of the Standard Model of particle physics predict the existence of new stable or unstable (or metastable) particles. If the new particle is massive and stable (or very long lived), it might be put in the candidate list of cold dark matter particles, provided that the particle is weakly coupled and it would not result in an unacceptable large Hubble expansion rate (or, put it in a commonly used but not accurate statement, namely, it would not overclose the universe) [18]. A good example of this kind of particles is the lightest neutralino when it is the LSP in the R-parity conserved MSSM.

If the new particle is light and can be treated as a radiation component during BBN, it would speed up the expansion rate of the universe and hence lead to more ^{4}He [20]. For example, using the baryon-to-photon ratio determined by WMAP [3], BBN constrains the number of additional effectively massless ($m \ll 1$ MeV) left-handed neutrino flavors cannot be more than 1 [21, 22].

If the new particle is massive and unstable (or metastable), it may decay during or

after BBN, and its decay products may alter the abundances of light nuclei by photo- and hadro-dissociation processes due to the non-thermal electromagnetic and hadronic interactions between the decay products with the background nuclei. These non-thermal interactions will either destroy or create light element species, so that the concordance between BBN predictions and measurements will set an upper limit on the possible abundance of the massive unstable particle as a function of its mass (or equivalently, lifetime), when the decay spectra of this heavy particle is determined from the theory under consideration. These limits have been the subject of many previous studies that have modeled both the electromagnetic and hadronic components of the showers induced by the decays of such heavy particles [23] - [45]. At the same time, bearing in mind that the light nuclei could either be destroyed or created by these non-thermal processes, one may want to try to explore whether some parameter space of the theory could help to cure the '^{7}Li problem', namely, the observational abundance of ^{7}Li is substantially lower than the standard BBN prediction by a factor of a few [46].

We revisit these constraints using a new interlocking suite of codes to model the decay spectra of the heavy particle, the evolution of the induced electromagnetic and hadronic showers in the early universe and their impact on BBN [47]. These suite of codes are potentially relevant to any extension of Standard Model that predicts the existence of massive unstable or metastable particles with a large range of lifetimes. As an example, we study the effects on the light-element abundances of the decays of massive gravitinos in neutralino dark matter scenarios within the constrained minimal supersymmetric extension of the Standard Model (CMSSM) [48].

In previous analyses of the CMSSM with a neutralino LSP, cosmological constraints on the decays of the metastable gravitino have usually been ignored. Essentially, it has been assumed implicitly that the gravitino is so heavy, and hence its lifetime is so short, that its decays take place so early in the history of the universe that they do not affect light-element abundances. However, from a theoretical point of view, a large hierarchy between the gravitino and LSP masses may appear unlikely. Indeed, in minimal supergravity (mSUGRA) and related models [49], it is usually the case that the gravitino is not much heavier than the LSP, if it is not the LSP itself. Therefore, it is important to analyze the case when the decays of gravitinos *do* affect the light-element abundances, and evaluate the resulting constraint on the primordial gravitino

abundance as a function of its mass. Indeed, an upper limit on the gravitino abundance may, in some circumstances, constrain severely the maximum temperature reached in the universe, e.g., following an early inflationary epoch [50] - [58].

We calculate all the two-body and the dominant three-body gravitino decay modes, so that we can get the gravitino lifetime and its decay spectra once the gravitino mass is given and the masses and couplings of the supersymmetric particles (sparticles) are determined by running down the renormalization group equations for a given set of CMSSM input parameters. The electromagnetic and hadronic showers induced by the decays of gravitinos and the secondary unstable particles are simulated using `PYTHIA` [59], and the evolution of the showers in the cosmological plasma and their interactions with the background nuclei are studied. When the ^{7}Li constraint is disregarded, for discrete choice of the gravitino mass, we present upper limits on the gravitino abundance for CMSSM parameters along the 'WMAP strips' where the lightest neutralino provides all of the cold dark matter. We are able to set firm upper limits on the possible abundance of the gravitino as a function of its mass and the CMSSM parameters. For some CMSSM benchmark points, we explore the possibility of the effects of the decays of gravitinos as a solution to the ^{7}Li problem, and we find a narrow range for the gravitino mass and abundance where the ^{7}Li problem is alleviated or even marginally solved.

The above work demonstrate the importance of the non-thermal interactions between the decay induced showers with the background nuclei in constraining new physics and solving the ^{7}Li problem. An accurate calculation of the constraints imposed by astrophysical observations on the abundance of a late-decaying massive particle requires taking into account not only the uncertainties in the astrophysical observations but also the uncertainties in the nuclear reaction rates that contribute to the production of light elements in both standard and modified BBN scenarios. However, due to the paucity of the measured cross-section data over the energy ranges of interest, the uncertainties of some non-thermal interaction rates can be large and need to be considered. In a follow-up work [60], we consider the effects of uncertainties in nuclear reaction rates on the cosmological constraints on the decays of unstable particles during or after BBN. We identify the most important non-thermal nuclear reactions for which improved nuclear experimental data would allow different light-element abundances to be determined more accurately, thereby making possible more precise probes of BBN and evaluations

of the cosmological constraints on unstable particles.

In addition to decays, the late-time annihilations of cold dark matter may also affect the abundances of the light elements [27, 37, 38, 61, 62]. In particular, these annihilations may have a significant effect on the abundance of ^{6}Li [38]. Indeed, in addition to the ^{7}Li problem, there are suggestions that the primordial ^{6}Li abundance might be about 1000 times higher than the standard BBN prediction [63, 64, 65, 66]. The debates on the interpretation of the observational data which leads to this '^{6}Li problem' have not been settled [67, 68], nevertheless in cold dark matter scenarios it is possible that the non-thermal particles injected by residual late-time dark matter annihilations during and after BBN may have a significant effect on the abundance of ^{6}Li, which, therefore, could serve as a constraint at the very least, or even a probe to new physics if future observations confirm the ^{6}Li problem. In [38] it was argued that ^{6}Li production may occur if the s-wave annihilation cross-section is sufficiently large, and it was assumed that the relic density of the annihilating dark matter particles is controlled largely by the s-wave part of the cross-section. However, in supersymmetric models where the LSP is a neutralino, such as the CMSSM, the relic density is in fact largely determined by the p-wave part of the cross-section, which by the time of BBN is essentially ineffective. Therefore, a reanalysis of the suggestion of [38] in the context of the CMSSM and related models is timely, and we study this effect in the CMSSM and the non-universal Higgs mass model (NUHM [69, 70, 71], which has one (NUHM1) or two (NUHM2) more input parameters as compared to the CMSSM). We find that residual neutralino dark matter annihilations could enhance the abundance of ^{6}Li up to two orders of magnitude while leaving the abundances of deuterium, ^{3}He, ^{4}He and ^{7}Li almost unaffected [72], in regions of parameter space which survive the available theoretical, phenomenological, experimental and cosmological constraints.

The layout of this thesis is as follows. In Chapter 2 we discuss the CMSSM, the main theoretical framework which we use to study gravitino decays and residual late-time neutralino dark matter annihilations. We also discuss the interactions between gravitino and the MSSM fields [73], collecting all the single gravitino-MSSM vertices in Appendix A. In Chapter 3 we summarize the cosmological data used in our analysis, and special emphasis is given to the lithium problems. In Chapter 4, we explain our treatment of the evolution of the hadronic and electromagnetic showers initiated by the decays of generic

metastable particles or residual annihilations of cold dark matter, and their effects on the primordial light-element abundances. In Chapter 5 we turn to the specific case in which the gravitino is the metastable particle, putting the detail results of the gravitino decay amplitudes used in the calculations in Appendix B. We discuss the resulting constraints on the abundance of a metastable neutral particle, under plausible assumptions on its dominant decay modes. We also consider constraints as a function of a generic particle lifetime, as well as constraints on the gravitino abundance in specific CMSSM scenarios with a neutralino LSP. In Chapter 6 we consider the effects of uncertainties in non-thermal nuclear reaction rates on the cosmological constraints on the decays of massive gravitinos during or after BBN. In Chapter 7 we discuss the effects of residual late-time neutralino dark matter annihilations on the ^{6}Li abundance. We summarize our conclusions in Chapter 8.

Chapter 2

Theoretical Framework: the CMSSM and the Gravitino

2.1 The CMSSM

The R-parity conserving MSSM [12, 13, 14] is specified by the superpotential

$$W = y_{\rm u}^{ij}\bar{u}_i Q_j \cdot H_{\rm u} - y_{\rm d}^{ij}\bar{d}_i Q_j \cdot H_{\rm d} - y_{\rm e}^{ij}\bar{e}_i L_j \cdot H_{\rm d} + \mu H_{\rm u} \cdot H_{\rm d}\,, \tag{2.1}$$

where the y's are the same Yukawa couplings entering in the SM, i and j $(= 1, 2, 3)$ are flavor indices, and we have suppressed the color indices. The '$\cdot$' means the SU(2)-invariant coupling of two doublets, and the 'bar' (in some literatures 'c' is used) on the fields signifying 'antiparticle', since in the MSSM the right-handed (chirality) particle fields are regarded as the charge conjugates of the corresponding left-handed antiparticle fields. The μ in the last term is the Higgs mixing parameter, which is the only new parameter introduced in the MSSM if supersymmetry is not broken. The various fields in eq. (2.1) are the chiral superfields, and their corresponding supermultiplet fields are listed in Table 2.1 [14], where the 'tilde' on the fields signifying sparticles. The other fields content of the MSSM are the gauge supermultiplet fields, and they are listed in Table 2.2.

Without imposing R-parity conservation, one could enlarge eq. (2.1) by adding terms which are also gauge-invariant and renormalizable, but violate lepton or baryon number

Table 2.1: Chiral supermultiplet fields in the MSSM.

Names		spin 0	spin 1/2	$SU(3)_c$, $SU(2)_L$, $U(1)_y$
squarks, quarks	Q	$(\tilde{u}_L, \tilde{d}_L)$	(u_L, d_L)	**3**, **2**, 1/3
($\times$ 3 families)	$\bar{u}$	$\tilde{\bar{u}}_L (\equiv \tilde{u}_R^*)$	$\bar{u}_L$	$\bar{\mathbf{3}}$, **1**, -4/3
	$\bar{d}$	$\tilde{\bar{d}}_L (\equiv \tilde{d}_R^*)$	$\bar{d}_L$	$\bar{\mathbf{3}}$, **1**, 2/3
sleptons, leptons	L	$(\tilde{\nu}_{eL}, \tilde{e}_L)$	(ν_{eL}, e_L)	**1**, **2**, -1
($\times$ 3 families)	$\bar{e}$	$\tilde{\bar{e}}_L (\equiv \tilde{e}_R^*)$	$\bar{e}_L$	**1**, **1**, 2
Higgs, Higgsinos	H_u	(H_u^+, H_u^0)	$(\tilde{H}_u^+, \tilde{H}_u^0)$	**1**, **2**, 1
	H_d	(H_d^0, H_d^-)	$(\tilde{H}_d^0, \tilde{H}_d^-)$	**1**, **2**, -1

Table 2.2: Gauge supermultiplet fields in the MSSM.

Names	spin 1/2	spin 1	$SU(3)_c$, $SU(2)_L$, $U(1)_y$
gluinos, gluons	$\tilde{g}$	g	**8**, **1**, 0
winos, W bosons	$\tilde{W}^{\pm}, \tilde{W}^0$	$W^{\pm}$, W^0	**1**, **3**, 0
bino, B boson	$\tilde{B}$	B	**1**, **1**, 0

conservations:

$$W_{\Delta L=1} = \lambda_e^{ijk} L_i \cdot L_j \bar{e}_k + \lambda_L^{ijk} L_i \cdot Q_j \bar{d}_k + \mu_L^i L_i \cdot H_u \tag{2.2}$$

and

$$W_{\Delta B=-1} = \lambda_B^{ijk} \bar{u}_i \bar{d}_j \bar{d}_k \,. \tag{2.3}$$

These terms are phenomenologically dangerous, because, for example, they could make proton decay with a rate far larger than the experimental upper limit, if the couplings in the terms are not extremely small. However, by introducing a new quantum number called R-parity, which is multiplicatively conserved, and is defined by $R \equiv (-1)^{3B+L+2s}$, where B, L and s are the baryon number, the lepton number and the spin of the particle, respectively, the terms in eq. (2.2) and (2.3) are forbidden, while all the terms in eq. (2.1) are allowed. One can easily check that R is +1 for all the SM particles (also for the two Higgs boson multiplets in the MSSM), and -1 for all the sparticles (due to the $(-1)^{2s}$ factor). As a bonus, the R-parity conservation makes the LSP absolutely stable, because it can not decay into anything else without violating this symmetry.

The superpotential (eq. (2.1)) only specifies the SUSY-invariant part of the MSSM Lagrangian. However, we know SUSY must be broken, otherwise the sparticles would have had the same masses as their superpartners and therefore had already been detected long ago. In lacking of knowledge and the consensus on how 'best' to break SUSY spontaneously, in practice it is useful to parameterize the SUSY-breaking by introducing terms which break SUSY explicitly. These so called soft SUSY-breaking terms are as follows.

(a) Gaugino mass terms for each gauge group:

$$-\frac{1}{2}(M_3\tilde{g}^\alpha\tilde{g}^\alpha + M_2\tilde{W}^\alpha\tilde{W}^\alpha + M_1\tilde{B}\tilde{B} + \text{h.c.})\,, \tag{2.4}$$

where the index α runs from 1 to 8, and 1 to 3 in the gluino and wino terms, respectively.

(b) Squark (mass)^2 terms:

$$-m^2_{\tilde{\mathrm{Q}}ij}\tilde{Q}_i^\dagger\cdot\tilde{Q}_j - m^2_{\tilde{\bar{\mathrm{u}}}ij}\tilde{\bar{u}}_i^\dagger\tilde{\bar{u}}_j - m^2_{\tilde{\bar{\mathrm{d}}}ij}\tilde{\bar{d}}_i^\dagger\tilde{\bar{d}}_j\,. \tag{2.5}$$

(c) Slepton (mass)^2 terms:

$$-m^2_{\tilde{\mathrm{L}}ij}\tilde{L}_i^\dagger\cdot\tilde{L}_j - m^2_{\tilde{\bar{\mathrm{e}}}ij}\tilde{\bar{e}}_i^\dagger\tilde{\bar{e}}_j\,. \tag{2.6}$$

(d) Higgs (mass)^2 terms:

$$-m^2_{\mathrm{H_u}}H_{\mathrm{u}}^\dagger\cdot H_{\mathrm{u}} - m^2_{\mathrm{H_d}}H_{\mathrm{d}}^\dagger\cdot H_{\mathrm{d}} - (B\mu H_{\mathrm{u}}\cdot H_{\mathrm{d}} + \text{h.c.})\,. \tag{2.7}$$

(e) Triple scalar coupling terms:

$$-a_{\mathrm{u}}^{ij}\tilde{\bar{u}}_i\tilde{Q}_j\cdot H_{\mathrm{u}} + a_{\mathrm{d}}^{ij}\tilde{\bar{d}}_i\tilde{Q}_j\cdot H_{\mathrm{d}} + a_{\mathrm{e}}^{ij}\tilde{\bar{e}}_i\tilde{L}_j\cdot H_{\mathrm{d}} + \text{h.c.}\,. \tag{2.8}$$

When all the fields in the MSSM are considered, these soft SUSY-breaking terms introduce more than a hundred new parameters. Fortunately, extensive regions of the parameter space are in fact excluded by phenomenological consideration, since most of the new parameters imply flavor mixing or CP violating processes of the types that are severely restricted by experiment. Motivated by these constraints and the possible GUT-scale origin of the soft SUSY-breaking terms, the parameters in eq. (2.4) - (2.8) may take a particularly simple form at the GUT scale:

$$M_3 = M_2 = M_1 = m_{1/2}\,, \tag{2.9}$$

$$\mathbf{m}^2_{\tilde{\mathrm{Q}}} = \mathbf{m}^2_{\tilde{\mathrm{u}}} = \mathbf{m}^2_{\tilde{\mathrm{d}}} = \mathbf{m}^2_{\tilde{\mathrm{L}}} = \mathbf{m}^2_{\tilde{\mathrm{e}}} = m_0^2\,\mathbf{1}\,, \tag{2.10}$$

where the **1** stands for the unit matrix in flavor space, and

$$\mathbf{a}_{\mathrm{u}} = A_0\mathbf{y}_{\mathrm{u}},\ \mathbf{a}_{\mathrm{d}} = A_0\mathbf{y}_{\mathrm{d}},\ \mathbf{a}_{\mathrm{e}} = A_0\mathbf{y}_{\mathrm{e}}\,, \tag{2.11}$$

where the $\mathbf{y}$ matrices are those appearing in eq. (2.1). If we further require

$$m^2_{\mathrm{H_u}} = m^2_{\mathrm{H_d}} = m_0^2\,, \tag{2.12}$$

then these universality conditions, namely, eq. (2.9) - (2.12), form the basis of the CMSSM [48], which is described by four parameters and a sign: the universal gaugino, scalar, and trilinear masses, $m_{1/2}$, m_0, and A_0, respectively, the ratio of the two Higgs vacuum expectation values, $\tan\beta$, and the sign of the Higgs mixing parameter, μ. Note that the parameter B appearing in eq. (2.7), the absolute value of μ, and the other combination of the two Higgs vacuum expectation values, are not independent parameters after the consideration of electroweak symmetry breaking. For each point in the CMSSM parameter space (the four parameters and the sign of μ), the sparticle masses and couplings at low energy scale are determined by running down the renormalization group equations (RGEs) from the GUT scale. An example of the running of the mass parameters in the CMSSM is shown in Fig. 2.1 [13].

After electroweak symmetry breaking, mixing will in general occur among fields which have the same color, charge and spin. So the fields which are the interaction eigenstates listed in Table 2.1 and 2.2 are needed to be rearranged to be the mass eigenstates when calculating the various decay rates or annihilation cross sections. For the four neutralino mass eigenstates $\tilde{\chi}^0_{1,2,3,4}$, they are the linear combinations of the bino $\tilde{B}$, neutral wino $\tilde{W}^0$ and neutral Higgsinos $\tilde{H}^0_{\mathrm{u}}$ and $\tilde{H}^0_{\mathrm{d}}$. Similarly, the charginos $\tilde{\chi}^{\pm}_{1,2}$ are the linear combinations of the charged winos $\tilde{W}^{\pm}$, and charged Higgsinos $\tilde{H}^+_{\mathrm{u}}$ and $\tilde{H}^-_{\mathrm{d}}$. In principle, the u-type squarks ($\tilde{u}_{\mathrm{L}}$, $\tilde{u}_{\mathrm{R}}$, $\tilde{c}_{\mathrm{L}}$, $\tilde{c}_{\mathrm{R}}$, $\tilde{t}_{\mathrm{L}}$, $\tilde{t}_{\mathrm{R}}$) will lead to a 6×6 mixing problem, and similarly for d-type squarks and the charged sleptons, while the sneutrinos lead to a 3×3 mixings. Fortunately, in the CMSSM the universality conditions eq. (2.10) and (2.11) guarantee the suppression of many unwanted interfamily mixing terms. Moreover, by considering the fact that the Yukawa couplings appearing in eq. (2.1) and (2.8) (see also eq. (2.11)) are proportional to the quark and lepton

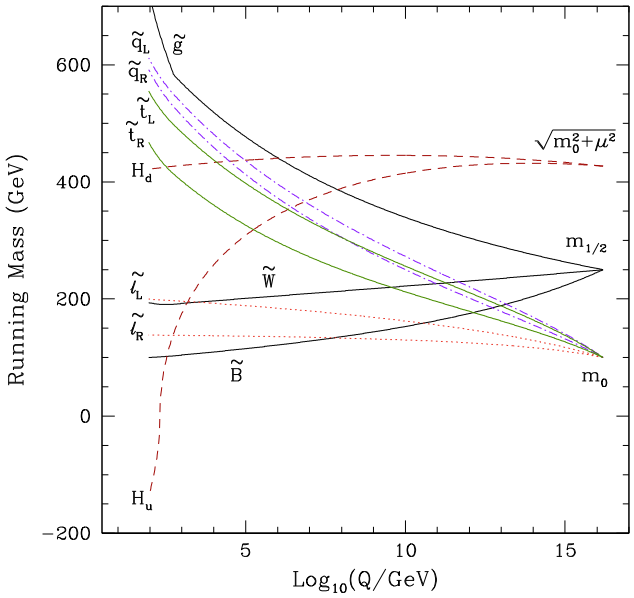

Figure 2.1: RG evolution of the mass parameters in the CMSSM. Here, $m_{1/2} = 250$ GeV, $m_0 = 100$ GeV, $\tan\beta = 3$, $A_0 = 0$, and $\mu < 0$ are chosen. Notice that the negative sign in the figure refers to the sign of $(mass)^2$, and $m^2_{\mathrm{H_u}}$ goes negative triggering electroweak symmetry breaking.

masses, of which the ones in the third family are considerably larger than the ones in the first two families, for a good approximation we can only include the terms of the third family in these two equations. These arguments ensure that we only need to deal with the left-right mixing for the third family in our consideration of the mixings in the squark and slepton sectors. We denote the mass eigenstates of the stop to be $\tilde{t}_{1,2}$, which are the linear combinations of the $\tilde{t}_{\mathrm{L,R}}$, similarly for the sbottom and stau we denote the mass eigenstates to be $\tilde{b}_{1,2}$ and $\tilde{\tau}_{1,2}$, respectively. For the Higgs sector, due to the Higgs mechanism three degrees of freedom of the four complex scalars H^+_{u}, H^0_{u}, H^0_{d} and H^-_{d} become the longitudinal modes of the $W^\pm$ and Z bosons, while the other five degrees of freedom lead to the mass eigenstates, namely, CP-even Higgs $H^0_{1,2}$, CP-odd Higgs H^0_3 and charged Higgs $H^\pm$. The gluinos $\tilde{g}$ cannot mix with any other fields, since they are

the only color octet fermions.

Finally, we briefly comment on the NUHM1 and NUHM2 models [69, 70, 71]. Comparing to the other universality conditions, there is less reason to postulate universality between the Higgs fields and the sfermions (squarks and sleptons). The full universality, postulated in the CMSSM, would occur in mSUGRA scenarios [49], but not in more general effective no-scale supergravity theories such as those derived from string models [74]. If we loose the condition eq. (2.12) to

$$m^2_{\mathrm{H_u}} = m^2_{\mathrm{H_d}} \tag{2.13}$$

at the GUT scale, we get the NUHM1 scenario, that is, there is universality for the two Higgs doublets alone, but not between the Higgs fields and the sfermions. If we further discard eq. (2.13) so that there is even no universality for the two Higgs doublets, we get the NUHM2 scenario.

2.2 Interactions between a single gravitino and the MSSM fields

By promoting global SUSY transformations to local ones, the gauge field of SUSY, namely, the gravitino field, which is the superpartner of the graviton, is introduced. The interaction vertices between a single gravitino and the MSSM fields are obtained from the interaction Lagrangian

$$\begin{aligned}
\mathcal{L}_{\mathrm{int}} &= -\frac{i}{\sqrt{2}\,M_P}\,\bar{\psi}_\mu\,S^\mu_{\mathrm{MSSM}} + \mathrm{h.\,c.} \\
&= -\frac{i}{\sqrt{2}M_P}\left[\mathcal{D}^{(\alpha)}_\nu \phi^{*i}\overline{\psi}_\mu\gamma^\nu\gamma^\mu\chi^i_L - \mathcal{D}^{(\alpha)}_\nu\phi^i\overline{\chi}^i_L\gamma^\mu\gamma^\nu\psi_\mu\right] \\
&\quad -\frac{i}{8M_P}\overline{\psi}_\mu[\gamma^\rho\,,\gamma^\sigma]\gamma^\mu\lambda^{(\alpha)}F^{(\alpha)}_{\rho\sigma} \quad ,
\end{aligned} \tag{2.14}$$

where, following the notation of [75], ψ_μ denotes the gravitino field, ϕ and χ_L the scalar and fermion components of the chiral MSSM superfields, $F_{\rho\sigma}$ is the field strength of a gauge boson field, and λ is the corresponding gaugino. We denote $\chi_L = P_L\chi$ and $\overline{\chi}_L = \overline{\chi}P_R$, where P_L and P_R are the usual chiral projectors. M_P is the reduced Planck mass defined as $M_P = 1/\sqrt{8\pi G_N}$, where G_N is the Newton gravitational constant. The indices i and (α) label the chiral and gauge multiplets, respectively (notice that we

are implicitly summing over all the MSSM chiral and gauge multiplets). The covariant derivative of a scalar field is

$$\mathcal{D}_\mu^{(\alpha)}\phi^i \equiv \partial_\mu \phi^i + i\, g_{(\alpha)}\, A_\mu^{(\alpha)a}\, \left(T^{(\alpha)a}\,\phi\right)^i \,. \tag{2.15}$$

In the first line of (2.14), $S^\mu_{\rm MSSM}$ denotes the contribution from the MSSM fields to the supercurrent and contains only terms from the SUSY-invariant part of the MSSM Lagrangian. Specifically, under a supersymmetry transformation, any MSSM field (of any spin) Φ_i transforms as $\Phi_i \to \Phi_i + \delta\Phi_i$, while the SUSY-invariant part of the MSSM Lagrangian transforms as $\mathcal{L}_{\rm susy} \to \mathcal{L}_{\rm susy} + \partial_\mu K^\mu$. Then, the supercurrent is

$$\epsilon\, S^\mu_{\rm MSSM} \;\equiv\; \frac{\partial \mathcal{L}_{\rm susy}}{\partial\left(\partial_\mu \Phi_i\right)}\,\delta\Phi_i - K^\mu \,, \tag{2.16}$$

where ϵ is the supersymmetry variation parameter. The explicit expression for the supercurrent can be found for example in [76].

At the energy scales of BBN, electroweak symmetry breaking has already happened. We want to single out the gravitino interactions that arise due to the breaking of the electroweak symmetry. Following [77], we denote the two Higgs doublets as

$$H_1 \equiv \begin{pmatrix} H_1^1 \\ H_1^2 \end{pmatrix} \;\;,\;\; H_2 \equiv \begin{pmatrix} H_2^1 \\ H_2^2 \end{pmatrix} \;\;, \tag{2.17}$$

and we denote their vacuum expectation values (vevs) as $\langle H_1^1\rangle \equiv v_1$, $\langle H_2^2\rangle \equiv v_2$, $\langle H_1^2\rangle = \langle H_2^1\rangle = 0$ (Note that the H_1 here is the same as the $H_{\rm d}$ used in section 2.1, and H_2 is the same as $H_{\rm u}$. Correspondingly, v_1 is often denoted as $v_{\rm d}$ in the literature, and v_2 is often denoted as $v_{\rm u}$). We denote the corresponding Higgsino fields as

$$\tilde{H}^1_{1\,L} \equiv P_L\,\tilde{H}_1 \;\;,\;\; \tilde{H}^2_{1\,L} \equiv P_L\,\tilde{H}^- \;\;,\;\; \tilde{H}^1_{2\,L} \equiv P_L\,\tilde{H}^+ \;\;,\;\; \tilde{H}^2_{2\,L} \equiv P_L\,\tilde{H}_2 \;\;, \tag{2.18}$$

where $\tilde{H}^- = \left(\tilde{H}^+\right)^c$, and the superscript '$c$' means charge conjugation.

Then the interaction term we are interested in is

$$\begin{aligned}\mathcal{L}_{\rm int} \;\supset\; -\frac{g}{M_P}\,\bar{\psi}_\mu \Big[& v_1\, W^{\mu+}\, P_L\tilde{H}^- + v_2\, W^{\mu-}\, P_L\tilde{H}^+ \\ & + \frac{Z^\mu}{\sqrt{2}\,\cos\theta_w}\,\left(v_1\, P_L\tilde{H}_1 - v_2\, P_L\tilde{H}_2\right)\Big] + \text{h.c.}\end{aligned} \tag{2.19}$$

(where we have used $\bar{\psi}_\mu\gamma^\mu = 0$, and where the gauge fields are defined in the standard way, see for instance [10]). We rewrite these interactions in terms of the chargino

($\tilde{\chi}_j$,$j = 1, 2$) and neutralino ($\tilde{\chi}_i^0$,$i = 1, \ldots, 4$) mass eigenstates, using the rotation formulae [77]

$$\begin{aligned} P_L\,\tilde{H}^+ = V_{j2}^*\,P_L\,\tilde{\chi}_j \quad &, \quad P_L\,\tilde{H}^- = U_{j2}^*\,P_L\,\tilde{\chi}_j^c \quad , \\ P_L\,\tilde{H}_1 = N_{i\,3}^*\,P_L\,\tilde{\chi}_i^0 \quad &, \quad P_L\,\tilde{H}_2 = N_{i\,4}^*\,P_L\,\tilde{\chi}_i^0 \quad . \end{aligned} \tag{2.20}$$

We also rewrite the two Higgs vevs in terms of the (tree level) M_W and M_Z, using the notation [77]: $M_W^2 = g^2\left(v_1^2 + v_2^2\right)/2$ and $\tan\beta \equiv v_2/v_1$. We end up with

$$\begin{aligned} \mathcal{L}_{\rm int} \quad \supset \quad -\frac{1}{M_P}\,\bar{\psi}_\mu\,P_L\Big[\sqrt{2}\,M_W\left(\cos\beta\,U_{j2}^*\,W^{\mu+}\tilde{\chi}_j^c + \sin\beta\,V_{j2}^*\,W^{\mu-}\tilde{\chi}_j\right) \\ + M_Z\left(\cos\beta\,N_{i3}^* - \sin\beta\,N_{i4}^*\right)Z^\mu\,\tilde{\chi}_i^0\Big] + \text{h.c.}\,. \end{aligned} \tag{2.21}$$

The remaining interactions between the gravitino and MSSM fields coming from (2.14), can be found in [75] using MSSM gauge eigenstates in the absence of electroweak symmetry breaking. In Appendix A, we rewrite the gravitino-MSSM interactions in terms of the MSSM mass eigenstates, including the effects of electroweak symmetry breaking in the rotation matrices (between gauge and mass eigenstates) [73]. These results are used to calculate the gravitino decay amplitudes.

Chapter 3

Cosmological Data

The abundances of the light elements D and ^{4}He predicted by BBN theory agree quite well with the values determined by observation, if the baryon-to-photon ratio η is that inferred from CMB measurements [3, 78]. This concordance provides the basis for the constraints on metastable particle decays or residual late-time dark matter annihilations to be discussed in this thesis. However, there is known to be an issue regarding the abundance of ^{7}Li, and there might also be a problem for the abundance of ^{6}Li.

3.1 Deuterium, ^{3}He and ^{4}He abundances

Deuterium provides a powerful constraint, as it is very sensitive to the baryon content in the universe, and thus offers by itself a measure of η. Local deuterium that is measured in the solar neighborhood in the interstellar medium provides a strong lower limit on the cosmological abundance, given that astrophysical effects destroy more deuterium than they produce [79]. Recent observations by FUSE show a wide dispersion in the deuterium abundance in local gas seen via its absorption, $(\mathrm{D/H})_{\text{local gas}} = (0.5 - 2.2) \times 10^{-5}$[80]. This surprisingly large spread, taken together with the positive correlation of D/H with temperature and metallicity along various sightlines, led [80] to suggest that deuterium may suffer significant and preferential depletion onto dust grains. In this case the true local interstellar D/H value would lie at the upper limit of the observed values, giving $(\mathrm{D/H})_{\mathrm{ISM}} \gtrsim (2.31 \pm 0.24) \times 10^{-5}$. However, extracting a primordial deuterium value requires a Galactic chemical evolution model (e.g., [81]), whose model dependences

yield uncertainties in the determination of the primordial deuterium abundance.

A high-redshift, metal-poor system is free of many such model uncertainties. In particular, observing the absorption features of quasar light due to a dense high-redshift cloud can be used to determine the primordial deuterium abundance. We use the deuterium abundance as determined in several high-redshift quasar absorption systems, which have a weighted mean abundance [82] - [88]

$$\left(\frac{\mathrm{D}}{\mathrm{H}}\right)_p = (2.82 \pm 0.21) \times 10^{-5}\,, \tag{3.1}$$

where the uncertainty includes a scale factor of 1.7 due to the dispersion found in these observations. Since the D/H ratio shows considerable scatter, it is likely that systematic errors dominate the uncertainties. In this case it may be more appropriate to derive the uncertainty using sample variance (see e.g. [89]) which gives a more conservative range $\mathrm{D/H} = (2.82 \pm 0.53) \times 10^{-5}$. We will comment further on this in Chapter 6 when we discuss the effects of uncertainties in non-thermal nuclear reaction rates. We use 3.2×10^{-5} as our fiducial upper limit on the D/H abundance, but we also illustrate the effect of significant variations in D/H around this value. The standard BBN result for D/H at the WMAP value for η [3] is $(2.52 \pm 0.17) \times 10^{-5}$, showing potentially a slight discrepancy with the observed value, unless one adopts the larger uncertainty.

Since ^{3}He is also quite sensitive to the baryon density, one might hope that it too could be used as a baryometer. Observations of HII regions in our own Galaxy yield values of the ^{3}He/H ratio that are compatible with calculations of the primordial value [90, 91]. However, the extrapolation from the observations to a primordial abundance is complicated by the unknown chemical evolution of ^{3}He. Indeed, one does not even know whether ^{3}He/H is increasing or decreasing with cosmic time. Thus, a primordial extrapolation yields only an order-of-magnitude range of allowable values of ^{3}He/H [92]. However, if we use the results of [79, 93] that the deuterium abundance is always decreasing with time, and assume that ^{3}He changes relatively slowly, we can adopt their ratio:

$$\left(\frac{^3\mathrm{He}}{\mathrm{D}}\right)_p < 1.0 \tag{3.2}$$

as a conservative constraint on the primordial ^{3}He/D ratio.

The ^{4}He abundance is determined from observations of extragalactic HII regions.

These abundance determinations are known to suffer from large systematic uncertainties [94, 95]. A recent analysis found [96]

$$Y_p = 0.256 \pm 0.011, \tag{3.3}$$

and a similar central value was found in [97]. The standard BBN result for Y_p at the WMAP value for η [3] is 0.2487 ± 0.0002, which is consistent with observations, given the error in (3.3). In our subsequent analysis, we adopt the lower limit $Y_p > 0.240$.

3.2 The ^{7}Li problem

The ^{7}Li abundance is derived from observations of low-metallicity halo dwarf stars. Some $\gtrsim 100$ such stars show a plateau [98] in (elemental) lithium versus metallicity, with a small scatter consistent with observational uncertainties. This insensitivity of Li/H to (proto)-Galactic metal content and thus stellar nucleosynthesis indicates that lithium in these stars has a primordial or at least pre-Galactic origin. An analysis [99] of field halo stars gives a plateau abundance of

$$\left(\frac{\mathrm{Li}}{\mathrm{H}}\right)_{\mathrm{halo}\star} = (1.23^{+0.34}_{-0.16}) \times 10^{-10}, \tag{3.4}$$

where the errors include both statistical and systematic uncertainties. As in the case of ^{4}He, the errors are dominated by systematic uncertainties. For example, the lithium abundance in several globular clusters, tends to be somewhat higher [100] - [105], and we will make some comparisons in Chapter 6 to the result found in [105] of $^7\mathrm{Li/H} = (2.34 \pm 0.05) \times 10^{-10}$. However, the standard BBN result for ^{7}Li/H at the WMAP value for η [3] is $(5.12^{+0.71}_{-0.62}) \times 10^{-10}$, which differs significantly from both sets of the observed value. This discrepancy is known as the 'lithium problem' or more specifically the '^{7}Li problem' [46]. Note that the central values for the BBN abundances used here differ slightly from those in [46], primarily due to the small shift in η as reported in [3]. In our later analysis, we adopt $^7\mathrm{Li/H} < 2.75 \times 10^{-10}$ as our fiducial upper limit on the cosmological ^{7}Li abundance.

The existence of the ^{7}Li problem, and the nature of its solution, both have a direct impact on our analysis. It is possible that the problem points to new physics, in particular if the observations and standard theory are both correct with accurate error estimates. If SUSY were to lead to a solution of the ^{7}Li problem, this would tie

together a wide array of particle astrophysics experiments and observations. Indeed, it has been suggested [37, 38, 39] that the ^{7}Li problem could be solved by hadronic decays of a metastable neutral particle X with lifetime $\tau_X \sim 10^3$ sec. We will directly address and update this issue below. It is also possible that the ^{7}Li problem might have a more banal solution, such as the existence of a suitable carbon, boron or beryllium resonance [106]. On the other hand, it remains possible that the standard BBN light-element abundance predictions remain correct. Rather, it could be that the ^{7}Li problem instead reflects astronomical observational systematics in recovering a Li/H abundance from stellar spectra, though a recent study [107] of the effective temperature of metal poor stars confirmed the use of relatively low temperatures and a Li abundance in the range Li/H $= (1.3 - 1.4 \pm 0.2) \times 10^{-10}$. The ^{7}Li problem may also reflect astrophysical systematics due to Li depletion via circulation and nuclear burning over the > 10 Gyr lifetime of metal-poor stars [108], though the lack of star-to-star scatter in Li/H suggests the depletion could be negligibly small [99]. If there is depletion, for our problem the correct procedure would be to use the initial, undepleted Li/H abundances. However, since these cannot be determined accurately, we do not adopt a quantitative constraint for this possibility. That is, if the decaying particle scenario does not solve the ^{7}Li problem, we do not use ^{7}Li as a constraint on the decaying particle parameter space. Instead, we consider the limits on unstable particles when the ^{7}Li problem is assumed to be solved and thus the ^{7}Li constraints are ignored.

3.3 The ^{6}Li problem

^{6}Li has been observed in some halo stars [65] with [Fe/H] $\sim$ -2, and with an isotopic ratio that is

$$\left(\frac{^6\mathrm{Li}}{^7\mathrm{Li}}\right)_{\mathrm{halo}*} \sim 0.05. \tag{3.5}$$

These observations are consistent with the results of Galactic cosmic-ray (GCR) nucleosynthesis [64, 109, 110], though see below for results at lower metallicity. This confirms that most of the lithium is in the form of ^{7}Li, leaving unscathed the cosmological ^{7}Li problem.

However, a recent paper has reported the presence of a similar isotopic abundance in halo stars over a broad range of metallicities that extends to significantly lower values

([Fe/H] $\sim$ -1 to -3) [65, 66]. The inferred plateau ^{6}Li/H ratio $\sim$ (6 to 25)$\times 10^{-12}$ is about 1000 times higher than the ^{6}Li/H ratio predicted by standard homogeneous BBN [63, 64], namely ^{6}Li/H $\sim 10^{-14}$. The isotopic ratio (3.5) cannot be explained by conventional GCR nucleosynthesis, at the lowest metallicities: this is the cosmological ^{6}Li problem. The reliability of the ^{6}Li plateau at very low metallicity has been questioned [67, 68], so the ^{6}Li problem should be taken with a grain of salt. But in any case, these exciting if controversial results demonstrate that ^{6}Li abundances at levels ^{6}Li/H $\lesssim$ few $\times 10^{-12}$ are at or near the reach of present observational techniques.

Thus the current observational situation is evolving, but without question is interesting: at the very least, the present results serve as upper limits to primordial ^{6}Li, and impose bounds on non-standard BBN. At most, current data may already point to a primordial ^{6}Li problem which would *demand* new BBN physics, and probe its details.

It has been proposed that some decaying-particle scenario might produce ^{6}Li at the plateau level with some destruction of ^{7}Li [37, 43], [111] - [115], offering the possibility of solving both Lithium problems simultaneously. However, we note that solving the ^{6}Li problem would use up only a small fraction of the ^{7}Li whose destruction would be needed to solve the ^{7}Li problem, leading one to consider separate solutions for the two lithium problems. It is also possible that the ^{6}Li problem might be explained by nucleosynthesis due to cosmological cosmic rays produced at the epoch of structure formation [116]. In principle, it may be possible to destroy ^{6}Li through depletion. However, if ^{6}Li is destroyed through dilution along with ^{7}Li, then the ratio is unaffected. If instead, ^{6}Li is preferentially destroyed though nuclear processes, then typically it is so severely destroyed that it would be unobservable [117]. Therefore, we interpret eq. (3.5) as a firm upper limit on any primordial ^{6}Li [66, 67] when we consider the BBN constraints on metastable particle decays.

3.4 Baryon density

The baryon-to-photon ratio $\eta \equiv n_{\rm B}/n_\gamma \equiv 10^{-10}\eta_{10}$ is related to the present baryon density parameter $\Omega_{\rm B} = \rho_{\rm B}/\rho_{\rm crit}$ by $\Omega_{\rm B}h^2 = \eta_{10}/274$. Adopting the value of $\Omega_{\rm B}h^2$ indicated by the WMAP 5-year CMB data [78] gives the following estimate of the

baryon-to-photon ratio:

$$\eta_{10} = 6.23 \pm 0.17. \tag{3.6}$$

This is the default value we assume later in our BBN analysis for the constraints on massive particle decays in Chapter 5. The central value and error range here correspond to WMAP data combined with large-scale structure information, in a framework for which the primordial power spectrum is a simple power law with fixed index. Similar but slightly different values would result from, e.g., a running spectral index.

In Chapter 6 and 7, we take the value

$$\eta_{10} = 6.19 \pm 0.15 \tag{3.7}$$

indicated by the 7-year WMAP data [3], which is available at the time of the works presented in Chapter 6 and 7 were doing.

Chapter 4

Code Description: Incorporating Non-Thermal Reactions in BBN

Particle decays or annihilations during BBN generally have two main effects [23, 118]. First, they change the cosmic expansion rate due to the injection of additional relativistic species. This effect is model-independent, in that it is insensitive to the details of the decays or annihilations, beyond the assumption that the particles produced are relativistic [26]. Secondly, they introduce new, non-thermal decay or annihilation products – possibly electromagnetic and/or hadronic – which can interact with the background thermal nuclei and change the final light-element abundances. The branching ratios and spectra of hadronic and electromagnetic decay or annihilation particles and energies are model-dependent. While both effects occur in principle, the expansion effects are negligible for the decay or annihilation parameters of practical interest to us, and the non-thermal interaction effects are the dominant perturbations to the abundances. Consequently, we focus on these effects, and henceforth neglect the perturbation to the expansion rate.

Since the propagation of the non-thermal particles produced by dark matter annihilations is the same as the ones produced by heavy particle decays, we illustrate the code below by assuming the decay scenario, and we point out the necessary changes needed for the annihilation scenario at the end.

We consider decays of some generic massive unstable particle X, with total decay

rate Γ_X so that the lifetime $\tau_X = \Gamma_X^{-1}$. We quantify the X abundance as the ratio of its number density to background baryon

$$Y_X \equiv n_X/n_B. \tag{4.1}$$

Due to decays, we have $Y_X(t) = Y_X^{\rm init} e^{-t/\tau_X}$; our constraints will be on the initial, pre-decay abundance $Y_X^{\rm init}$, and this should be understood hereafter whenever we write Y_X.

We are interested in both hadronic and electromagnetic decays of the heavy particles X. We denote the electromagnetic branching ratio of X by $B_{\rm EM} = \Gamma_{X\to{\rm EM}}/\Gamma_X$. The abundance perturbations from electromagnetic decays, and thus the constraints on such decay modes, scale with the product of $B_{\rm EM}$ and the decay energy release per photon:

$$\zeta_X \equiv \frac{m_X n_X}{n_\gamma} = m_X Y_X \eta, \tag{4.2}$$

where the X abundance is evaluated prior to decay. As emphasized particularly by [39], electromagnetic decays inevitably accompany hadronic decays, and so both sets of decay products and interactions need to be included. Electromagnetic decays were discussed in detail in [111]; we include those processes here, incorporating the treatment described in [111]. However, the analysis there assumed that the electromagnetic decays occurred entirely after the usual BBN thermonuclear reactions have run to completion, i.e., the decays were treated as a 'post-processing' modification after the usual light-element abundances had been established. Here, we supplement the previous treatment by including electromagnetic decay effects consistently throughout BBN.

We quantify generic decays $X \to h$ of a particle X into a hadronic species h as follows. We write the h production rate per unit volume, and daughter kinetic energy ϵ as $q_h(\epsilon)$. The total X decay rate per baryon is $\Gamma_X Y_X$ and the total X decay rate per volume is $q_{X,{\rm tot}} = \Gamma_X Y_X n_{\rm B}$. It will be convenient to isolate the h production per X decay as $Q_h(\epsilon) = q_h(\epsilon)/q_{X,{\rm tot}}$, so that we have

$$q_h(\epsilon) \equiv \Gamma_X Y_X n_{\rm B} Q_h(\epsilon). \tag{4.3}$$

We refer to $Q_h(\epsilon)$ as the spectrum of X decays, which gives the number of h particles produced per X decay per energy interval. The integral $B_h \equiv \int Q_h(\epsilon)\, d\epsilon$ gives the

total number of h per X decay, and thus represents a multiplicity-weighted hadronic branching ratio.

We denote the abundance of the light element ℓ as $Y_\ell \equiv n_\ell/n_B$, which changes with time according to

$$\partial_t Y_\ell = (\partial_t Y_\ell)_{\rm SBBN} + (\partial_t Y_\ell)_{\rm EM} + (\partial_t Y_\ell)_{\rm had}\,, \tag{4.4}$$

where $(\partial_t Y_\ell)_{\rm SBBN}$ denotes the usual rate of change of ℓ in standard BBN due to thermonuclear reactions. The second term on the right-hand side of (4.4) accounts for non-thermal electromagnetic interactions due to X decays, either directly from the decays of X to photons or leptons, or through electromagnetic secondaries in the hadronic showers. These are treated as in [36], but are not dominant when hadronic branchings are significant. The final term on the right-hand side of (4.4) represents the non-thermal hadronic interactions.

The inclusion of hadronic decays in BBN requires a detailed evaluation of the rates for such interactions. For each background light nuclide species ℓ, we can write the hadronic contributions to $\partial_t Y_\ell$ as

$$(\partial_t Y_\ell)_{\rm had} = -\Gamma_{\ell\to{\rm inel}} Y_\ell + \sum_{hb} \Gamma_{hb\to\ell} Y_b. \tag{4.5}$$

The first term accounts for ℓ destruction by hadro-dissociation, where $\Gamma_{\ell\to{\rm inel}}$ is the total rate (per unit of the species ℓ) of all inelastic interactions of shower particles with ℓ. The second term accounts for production due to hadro-dissociation of heavier background species (e.g., deuteron production via helium erosion $p_{\rm shower}\alpha_{\rm bg} \to d + \cdots$). The sum of inelastic rates $\Gamma_{hb\to\ell}$ producing ℓ runs over shower species h and background targets b. In the particular case of lithium isotopes, production occurs via the interaction of energetic (i.e., non-thermal) mass-3 dissociation products with background ^{4}He, e.g., $^3{\rm He} + \alpha \to {}^{6,7}{\rm Li} + \cdots$.

Non-thermal particle propagation in the cosmic plasma is determined by competition among the various interactions that lead to particle losses – continuous energy losses as well as elastic and inelastic collisions. These loss processes are always rapid compared to the cosmic expansion rate. Thus, to a good approximation the non-thermal particle spectra are set by an equilibrium between injection and losses. These propagated, equilibrium spectra then determine the rates of non-thermal interactions with light nuclei via convolution with the relevant cross sections. That is, for the process $hb \to \ell$

of a non-thermal hadron interacting with a thermal background species b to produce light element ℓ, the interaction rate per target b is

$$\Gamma_{hb\to\ell} = \int N_h(\epsilon)\ v\ \sigma_{hb\to\ell}(\epsilon)\ d\epsilon \quad , \tag{4.6}$$

where $N_h(\epsilon)$ is the spectrum of non-thermal h having kinetic energy ϵ, v is the relative velocity between the projectile and the background target, and $\sigma_{hb\to\ell}$ is the cross section for the process at hand. The non-thermal processes considered here are listed in Table 4.1.

In evaluating the second and third term on the right-hand side of (4.4), we need to consider the interactions of multiple generations of non-thermal electromagnetic and hadronic showers with the background nuclei, that is, photo- and hadro-dissociation, and also to take into account the energy losses of the showers due to their interactions with the photon and electron-positron background. The method to study the evolution of these non-thermal showers is similar to the well-studied treatment of the cosmic-ray induced showers in the atmosphere, and the details are given in Appendix of A of [47].

So now the last piece of information needed to complete the calculation of eq. (4.4), so that to know the impact on BBN due to massive unstable particle decays, is the trigger of the non-thermal showers. This comes from the decay spectra of the massive unstable particle, determined by new theory, and will be illustrated in Chapter 5 for the case of gravitino decays in the context of the CMSSM. The decay spectra are interfaced with an event generator, in our case `PYTHIA` [59], to model the evolution of the decay products, namely, daughter particle decays and hadronization of quarks and gluons into mesons and baryons, before they interact with the background.

The description above is also applicable to the dark matter annihilation scenario, once one makes the appropriate substitution of abundances $n_X \to n_{\rm DM}$ and of annihilation rate for decay rate: $\Gamma_X = \tau_X^{-1} \longrightarrow \Gamma_{\rm ann}$.

Table 4.1: Nuclear reactions of non-thermal particles, including the most important of the estimated uncertainties in the cross sections.

Code	Reaction	Uncertainty ϵ	Reference
1	$p^4\mathrm{He} \rightarrow d^3\mathrm{He}$		Meyer [119]
2	$p^4\mathrm{He} \rightarrow np^3\mathrm{He}$	20%	Meyer [119]
3	$p^4\mathrm{He} \rightarrow ddp$	40%	Meyer [119]
4	$p^4\mathrm{He} \rightarrow dnpp$	40%	Meyer [119]
5	$d^4\mathrm{He} \rightarrow {}^6\mathrm{Li}\gamma$		Mohr [120]
6	$t^4\mathrm{He} \rightarrow {}^6\mathrm{Li}n$	20%	Cyburt et al. [36]
7	${}^3\mathrm{He}^4\mathrm{He} \rightarrow {}^6\mathrm{Li}p$	20%	Cyburt et al. [36]
8	$t^4\mathrm{He} \rightarrow {}^7\mathrm{Li}\gamma$		Cyburt [121]
9	${}^3\mathrm{He}^4\mathrm{He} \rightarrow {}^7\mathrm{Be}\gamma$		Cyburt and Davids [122]
10	$p^6\mathrm{Li} \rightarrow {}^3\mathrm{He}^4\mathrm{He}$		Cyburt et al. [36]
11	$n^6\mathrm{Li} \rightarrow t^4\mathrm{He}$		Cyburt et al. [36]
12	$pn \rightarrow d\gamma$		Ando, Cyburt, Hong, and Hyun [123]
13	$pd \rightarrow {}^3\mathrm{He}\gamma$		Cyburt et al. [36]
14	$pt \rightarrow n^3\mathrm{He}$		Cyburt [121]
15	$p^6\mathrm{Li} \rightarrow {}^7\mathrm{Be}\gamma$		Cyburt et al. [36]
16	$p^7\mathrm{Li} \rightarrow {}^8\mathrm{Be}\gamma$		Cyburt et al. [36]
17	$p^7\mathrm{Be} \rightarrow {}^8\mathrm{B}\gamma$		Cyburt et al. [47]
18	$np \rightarrow d\gamma$		Ando, Cyburt, Hong, and Hyun [123]
19	$nd \rightarrow t\gamma$		Cyburt et al. [36]
20	$n^4\mathrm{He} \rightarrow dt$		Meyer [119]
21	$n^4\mathrm{He} \rightarrow npt$	20%	Meyer [119]
22	$n^4\mathrm{He} \rightarrow ddn$	40%	Meyer [119]
23	$n^4\mathrm{He} \rightarrow dnnp$	40%	Meyer [119]
24	$n^6\mathrm{Li} \rightarrow {}^7\mathrm{Li}\gamma$		Cyburt et al. [36]
25	n (thermal)		—
26	$n^7\mathrm{Be} \rightarrow p^7\mathrm{Li}$		Cyburt et al. [36]
27	$n^7\mathrm{Be} \rightarrow {}^4\mathrm{He}^4\mathrm{He}$		Cyburt et al. [47]
28	$p^7\mathrm{Li} \rightarrow {}^4\mathrm{He}^4\mathrm{He}$		Cyburt et al. [36]
29	$n\pi^+ \rightarrow p\pi^0$		Meyer [119]
30	$p\pi^- \rightarrow n\pi^0$		Meyer [119]
31	$p^4\mathrm{He} \rightarrow ppt$	20%	Meyer [119]
32	$n^4\mathrm{He} \rightarrow nn^3\mathrm{He}$	20%	Meyer [119]
33	$n^4\mathrm{He} \rightarrow nnnpp$		Meyer [119]
34	$p^4\mathrm{He} \rightarrow nnppp$		Meyer [119]
35	$p^4\mathrm{He} \rightarrow N^4\mathrm{He}\pi$		Meyer [119]
36	$n^4\mathrm{He} \rightarrow N^4\mathrm{He}\pi$		Meyer [119]

Chapter 5

Nucleosynthesis Constraints on a Massive Gravitino in Neutralino Dark Matter Scenarios

5.1 Gravitino decays

As an application to the code described in Chapter 4, we study the massive unstable gravitino decays. We work in the context of the CMSSM. As we discussed in Section 2.1, the CMSSM is described by four parameters: universal gaugino, scalar, and trilinear masses, $m_{1/2}, m_0, A_0$, and the ratio of the two Higgs vacuum expectation values, $\tan\beta$, along with the sign of the Higgs mixing parameter, μ. Motivated by $g_\mu - 2$ and $b \to s\gamma$, we restrict our attention to $\mu > 0$ and, for simplicity, we consider only $A_0 = 0$. We consider scenarios in which the lightest neutralino is the LSP, but the gravitino is not assumed necessarily to be the next-to-lightest supersymmetric particle (NLSP). For fixed values of $\tan\beta$, the regions of parameter space for which the relic density of neutralinos is computed to lie within the range $0.0975 < \Omega_{\rm CDM}h^2 < 0.1223$ determined by WMAP [78] and other observations for cold dark matter form narrow strips that foliate the $(m_{1/2}, m_0)$ plane [124, 125]. These strips correspond to regions where there are enhanced annihilation cross sections that reduce the neutralino relic density to acceptable

values. These strips occur when the neutralino is nearly degenerate with some other supersymmetric particle such as the partner of the tau lepton (coannihilation strip), when the neutrino is close to half the mass of the heavy Higgs scalar and pseudoscalar boson so that rapid s-channel annihilation occurs (the funnel region), or at large values of m_0 when the renormalization-group evolution drives the value of μ to low values so that the neutralino acquires a significant Higgsino component and new final-state channels become important (the focus-point strip). Our analysis is based on the WMAP strips for two representative values of $\tan\beta = 10, 50$. For $\tan\beta = 10$ one strip follows the coannihilation corridor, and for $\tan\beta = 50$ this strip also includes the funnel at larger values of $m_{1/2}$. We also consider the focus-point strips for both values of $\tan\beta$.

In the scenario under study the gravitino decays into lighter sparticles, including the neutralino LSP but also others in general. We take into account all the dominant decay channels of the gravitino into (s)particles, including the complete set of two-body decays of the gravitino into Standard Model particles and their spartners. These fall into the following main categories: $\widetilde{G} \to \tilde{f}\, f$, $\widetilde{G} \to \tilde{\chi}^+ W^-(H^-)$, $\widetilde{G} \to \tilde{\chi}_i^0 \gamma(Z)$, $\widetilde{G} \to \tilde{\chi}_i^0 H_i^0$ and $\widetilde{G} \to \tilde{g}\, g$. Analytical expressions for these amplitudes can be found in Appendix B. In addition, we include the dominant three-body decays $\widetilde{G} \to \tilde{\chi}_i^0 \gamma^* \to \tilde{\chi}_i^0 q\overline{q}$, $\widetilde{G} \to \tilde{\chi}_i^0 W^+W^-$, which are also discussed in Appendix B. In principle, one should also include $q\overline{q}$ pair production through the virtual Z-boson channel $\widetilde{G} \to \tilde{\chi}_i^0 Z^* \to \tilde{\chi}_i^0 q\overline{q}$ [41] and the corresponding interference term. However, this process is suppressed by a factor of M_Z^4 with respect to $\widetilde{G} \to \tilde{\chi}_i^0 \gamma^* \to \tilde{\chi}_i^0 q\overline{q}$, and the interference term is also suppressed by M_Z^2. These contributions are therefore not very important, and we drop these amplitudes in our calculation. We also drop the corresponding amplitudes for Higgs and squark exchange. We calculate the lifetime of the gravitino by first calculating the partial widths of its dominant relevant decay channels, and then summing them. Typical results are shown in Fig. 5.1, where we see that the lifetimes for $\tan\beta = 50$ (right panels) are typically longer than those for $\tan\beta = 10$ (left panels), particularly for larger $m_{1/2}$. On the other hand, the lifetimes in the coannihilation/funnel regions (top panels) are quite similar to those in the focus-point regions (bottom panels).

In order to calculate the resulting electromagnetic (EM) and hadronic (HD) spectra, we first calculate the EM and HD decay spectra of the different gravitino decay modes, and then weight them by the corresponding branching ratios. The decay products

that yield EM energy obviously include directly-produced photons, but also indirectly-produced photons, charged leptons (electrons and muons) and neutral pions (π^0), which are produced via the secondary decays of unstable heavy particles such as gauge and Higgs bosons. Hadrons (nucleons and mesons such as the K_L^0, $K^\pm$ and $\pi^\pm$) are also usually produced through the secondary decays of heavy particles, as well as (for the mesons) via the decays of the heavy τ lepton. It is important to note that strange mesons and neutral pions decay before interacting with the hadronic background [35, 126, 127]. Hence they are relevant to BBN processes and to our analysis only via their decays into photons and charged leptons, which contribute to the EM component of the decay showers. Therefore, the HD injections that concern us are those that produce nucleons, via the decays of heavy particles such as gauge and Higgs bosons and quark-antiquark pairs and to a lesser extent charged pions.

After calculating the partial decay widths and branching ratios, we then employ the `PYTHIA` event generator [59] to model both the EM and the HD decays of the direct products of the gravitino decays. We first generate a sufficient number of spectra for the secondary decays of the gauge and Higgs bosons and the quark pairs. Then, we perform fits to obtain the relation between the injected energy of the decaying particle, that we call E_{inj}, and the quantity that characterizes the hadronic spectrum, namely Q_h, the number of produced nucleons as a function of the nucleon energy, for various values of the E_{inj}. We have performed fits that cover the range $200\,\mathrm{GeV} < E_{inj} < 20\,\mathrm{TeV}$. In Table 5.1 we present a representative set of fitting parameters for $E_{inj} = 1000\,\mathrm{GeV}$. Then, using the equation

$$Q_h(\epsilon_h) = \frac{\epsilon_h}{E_{\rm inj}^2}\,\frac{1}{x}\,\tilde{Q}_h(x)\,, \tag{5.1}$$

the spectrum distribution $Q_h(\epsilon_h)$ is computed using the function $\tilde{Q}_h(x) = Q_h(\epsilon_h)d\epsilon_h/dx$, with $x = \sqrt{\epsilon_h^2 - m_h^2}/E_{inj}$. Some typical spectra for gravitino decays into protons are shown in Fig. 5.2. These spectra and the fraction of the energy of the decaying particle that is injected as EM energy are then used to calculate the light-element abundances. We stress that this procedure is repeated separately for each point sampled in the supersymmetric parameter space. That is, given a set of parameters $m_0, m_{1/2}, A_0, \tan\beta$, $\mathrm{sgn}(\mu)$, and $m_{3/2}$, after determining the sparticle spectrum, all of the relevant branching

fractions are computed, and the hadronic spectra and the injected EM energy determined case by case. Thus, in our analysis, Q_p (Q_n) and hence the total number of protons (neutrons) per gravitino decay, B_p (B_n), varies between different points in the parameter space, and Fig. 5.3 illustrates this variation in B_p (and B_n) across the supersymmetric parameter space we sample.

Table 5.1: The values of the parameters A, B, C, D and E used in fitting `PYTHIA` hadronic decay spectra. We use the function $Y \equiv \log_{10}(\tilde{Q}(x))$ parametrized via $Y = A\,X^4 + B\,X^3 + C\,X^2 + D\,X + E$, where $X \equiv \log_{10}(x)$, and the scaling parameter x is defined as $x = \sqrt{\epsilon_h^2 - m_h^2}/E_{inj}$. The values of this table correspond to $E_{inj} = 1\,\text{TeV}$.

decaying particles	inj. species	A	B	C	D	E
Z	p	0.000	0.000	-1.230	-4.823	-3.401
	n	0.000	0.000	-1.281	-4.917	-3.418
h	p	0.000	0.000	-1.011	-4.302	-3.071
	n	0.000	0.000	-0.850	-3.628	-2.499
H	p	0.000	0.000	-0.647	-3.398	-2.154
	n	0.000	0.000	-0.644	-3.414	-2.230
A	p	0.000	0.000	-0.633	-3.356	-2.133
	n	0.000	0.000	-0.637	-3.377	-2.179
$q\bar{q}$	p	-0.065	-0.551	-2.007	-4.326	-2.602
	n	-0.033	-0.195	-0.603	-2.039	-1.327
$W^+\,W^-$	p	0.000	0.000	-1.146	-5.180	-4.036
	n	0.000	0.000	-1.107	-4.936	-3.742

The relative sizes of the gravitino partial widths and the locations of the various particle thresholds help us to understand the lifetime and the hadronic spectra curves. In general, the two-body channels $\widetilde{G} \to \tilde{\chi}_i^0\,\gamma$; $\tilde{f}\,f$; $\tilde{g}\,g$; $\tilde{\chi}^+\,W^-$ dominate the $\widetilde{G}$ decays. In particular, the decay to $\tilde{\chi}_i^0\,\gamma$ yields the bulk of the injected EM energy. However, the decays to sfermions, gluinos and charginos become of the same order of magnitude as the $\widetilde{G} \to \tilde{\chi}_i^0\,\gamma$ channel whenever they are kinematically possible. Also, when the $\widetilde{G}$ is heavy enough to decay into a real Z boson, the channel $\widetilde{G} \to \tilde{\chi}_i^0\,Z$ is the dominant channel for producing HD injections. When kinematically allowed, $\widetilde{G} \to \tilde{\chi}^+\,W^-$ and $\widetilde{G} \to \tilde{g}\,g$ are also important in producing HD injections. The Higgs boson channels are smaller by

a few orders of magnitude (due to couplings and kinematics) and, in particular, in the large-$m_{1/2}$ region, decays to heavy Higgs bosons (H, A) become kinematically accessible only for heavy $\widetilde{G}$ and are unimportant otherwise.

Turning to the three-body channels, the decay through the virtual photon to a $q\overline{q}$ pair can become comparable to the channel $\widetilde{G} \to \tilde{\chi}_i^0 Z$, injecting nucleons even in the kinematical region $m_{3/2} < m_\chi + M_Z$, where direct on-shell Z-boson production is not possible. Finally, we note that the partial width of the three-body decay $\widetilde{G} \to \tilde{\chi}_i^0 W^+W^-$ is usually smaller by at least an order of magnitude relative to the dominant two-body decays, except when this three-body decay exhibits resonant behavior. For example, the subprocess $\widetilde{G} \to \tilde{\chi}^{+*}W^- \to \tilde{\chi}_i^0 W^+W^-$ can lift the contribution of the $\tilde{\chi}_i^0 W^+W^-$ channel to the level of the dominant two-body decays in the threshold region where the chargino can be produced on-shell.

With these observations in mind, one can understand the gravitino lifetime curves along the WMAP strips for $\tan\beta = 10$ and 50 in Fig. 5.1. We recall that the funnel region is only present in the CMSSM for large $\tan\beta$. Since the relation $m_\chi \approx m_A/2$ is realized at large $m_{1/2}$, the WMAP strip extends to significantly higher values of $m_{1/2}$ for $\tan\beta = 50$ than for $\tan\beta = 10$. In the latter case (upper left panel), the WMAP strip shown consists only of a coannihilation region, which terminates around $m_{1/2} = 900$ GeV. We notice that the gravitino lifetime is longer for $\tan\beta = 50$ than for $\tan\beta = 10$, for the same values of $m_{3/2}$ and $m_{1/2}$. Especially for the two upper panels, this is because for $\tan\beta = 50$ the WMAP strip, in the coannihilation region and (particularly) in the Higgs rapid-annihilation funnel region, occurs at larger m_0 and hence heavier squark and slepton masses, than in the $\tan\beta = 10$ case. This implies that the dominant two-body channels $\widetilde{G} \to \tilde{f}\, f$ are very suppressed or even closed for $\tan\beta = 50$. Thus, the total gravitino decay width is smaller (and hence the lifetime longer) for $\tan\beta = 50$ than for $\tan\beta = 10$.

The lower panels in Fig. 5.1 correspond to the focus-point region. It is worth noticing that, unlike the coannihilation or the rapid-annihilation region, the focus-point strip extends to remarkably high values of m_0 and $m_{1/2}$. For example, for $\tan\beta = 50$ (lower right panel) $m_0 \sim 3\,\text{TeV}$ ($5\,\text{TeV}$) at $m_{1/2} = 1000\,\text{GeV}$ ($2000\,\text{GeV}$). As a result, the sfermion masses in this region are much larger than in the funnel or the coannihilation strip. Hence, for gravitino masses up to 1 TeV all the fermion-sfermion decay channels

$\widetilde{G} \to \tilde{f}\, f$ are closed, and the lifetime is larger than the upper panels. On the other hand, when $m_{3/2} = 5\,\mathrm{TeV}$ the dominant decay channels $\tilde{g}\, g$, $\tilde{f}\, f$ and $\tilde{\chi}^+ W^-$ are open along the WMAP strips also in the focus-point region, resulting in relatively flat lifetime curves as functions of $m_{1/2}$.

We note that for $m_{3/2} = 5$ TeV, the largest value shown, the gravitino lifetime $\sim$ few $\times 10^2$ s in all the cases shown in Fig. 5.1, which is comparable with the duration of BBN. Lighter gravitinos would decay after BBN is completed.

As $m_{1/2}$ increases for fixed $m_{3/2}$, the gaugino masses increase. Therefore, one by one the various gravitino decay channels are closed. The last to be closed are the two-body decay to $\tilde{\chi}_1^0\, \gamma$ and the three-body decay to light quark pairs $\tilde{\chi}_1^0\, q\overline{q}$. Eventually all the channels are closed when $m_{3/2} < m_\chi$. For $m_{3/2} = 250\,\mathrm{GeV}$ this occurs for $m_{1/2} \sim 580\,\mathrm{GeV}$, as can be seen in Fig. 5.1. When the dominant channel for hadron production, $\tilde{\chi}_1^0\, Z$, closes we observe a significant decline in the nucleon spectra. This is the reason that in Fig. 5.3 in all the panels, for $m_{3/2} = 250\,\mathrm{GeV}$ the value of B_p becomes smaller than 10^{-2} at $m_{1/2} = 400\,\mathrm{GeV}$, and the same at $m_{1/2} = 940\,\mathrm{GeV}$ when $\tan\beta = 50$ and $m_{3/2} = 500\,\mathrm{GeV}$ (right panels). Above these values of $m_{1/2}$, the only channel that produces some hadrons is $\widetilde{G} \to \tilde{\chi}_1^0\, q\overline{q}$.

The importance of the channel $\widetilde{G} \to \tilde{\chi}_i^0\, Z$ for producing nucleons can be seen in Fig. 5.2. There we plot the quantity $\epsilon\, N_p(\epsilon)$ for the case of protons for $\tan\beta = 10$ and $m_{3/2} = 250\,\mathrm{GeV}\,(500\,\mathrm{GeV})$ in the left (right) panel. The curves in these figures correspond to the various $m_{1/2}$ we sample along the WMAP coannihilation strip. The reason for the peaks in the GeV region is that the protons that are produced by on-shell hadronic decays of the Z boson have typical energies of a few GeV. As discussed earlier, for $\tan\beta = 10$ and $m_{3/2} = 250\,\mathrm{GeV}$ the $\tilde{\chi}_i^0\, Z$ channel closes above $m_{1/2} = 400\,\mathrm{GeV}$. Therefore, we observe two kinds of curves in Fig. 5.2 (left). These that peak in the GeV region are fed by the $\tilde{\chi}_1^0\, Z$ channel, whereas these without the peak originate from the three-body channel $\tilde{\chi}_1^0\, q\overline{q}$. For $\tan\beta = 10$ and $m_{3/2} = 500\,\mathrm{GeV}$, the decay $\widetilde{G} \to \tilde{\chi}_1^0\, Z$ is not closed anywhere along the WMAP strip, so all the curves in Fig. 5.2 (right) exhibit the Z-boson peak.

There are a few other features in Fig. 5.3 to be discussed. For $m_{1/2} \gtrsim 240\,\mathrm{GeV}$ in the upper panels the lightest chargino can decay on-shell to $\tilde{\chi}_i^0\, W^+$. The same happens in the lower left (right) panel for $m_{1/2} = 520\,\mathrm{GeV}$ ($m_{1/2} = 360\,\mathrm{GeV}$). This

causes a sudden increase in the number of the produced protons, that is more noticeable for $\tan\beta = 10$ (upper left panel), since there the relative importance of the decay channel $\widetilde{G} \to \tilde{\chi}_1^{+*} W^- \to \tilde{\chi}_i^0 W^+ W^-$ is greater. This channel is closed for larger values of $m_{1/2}$ as the chargino becomes heavier, resulting in the shoulders we observe for $\tan\beta = 10$ (upper left panel) in the B_p curves at $m_{1/2} = 520\,\text{GeV}$ ($m_{3/2} = 500\,\text{GeV}$) and $m_{1/2} = 800\,\text{GeV}$ ($m_{3/2} = 750\,\text{GeV}$). The corresponding features appear also at the same points for $\tan\beta = 50$ in Fig. 5.3 (upper right panel). In the same figure, for $m_{3/2} \geq 500$ GeV, the additional wiggle seen at $m_{1/2} \sim 280$ GeV is due to the closing of the $\widetilde{G} \to \tilde{\chi}_2^+ W^-$ channel. In the focus-point figures (lower panels), at $m_{1/2} = 400\,\text{GeV}$ and $m_{3/2} = 250\,\text{GeV}$ the $\tilde{\chi}_1^0 Z$ channel closes. The same occurs at $m_{1/2} = 960\,\text{GeV}$ ($m_{1/2} = 1460\,\text{GeV}$) for $m_{3/2} = 500\,\text{GeV}$ ($m_{3/2} = 750\,\text{GeV}$). After this point, B_p diminishes. Along the focus-point strip, we also can see in the B_p curves the effect of the closing of the $\tilde{\chi}_{1,2}^+ W^-$ channels. In particular, the $\tilde{\chi}_1^+ W^-$ channel closes at $m_{1/2} = 780\,\text{GeV}$ for $m_{3/2} = 500\,\text{GeV}$, $\tan\beta = 10$, at $m_{1/2} = 1200\,\text{GeV}$ for $m_{3/2} = 750\,\text{GeV}$, $\tan\beta = 50$, and at $m_{1/2} = 1640\,\text{GeV}$ for $m_{3/2} = 1000\,\text{GeV}$, $\tan\beta = 50$. For $\tan\beta = 50$, the $\tilde{\chi}_2^+ W^-$ channel closes at $m_{1/2} = 440\,\text{GeV}$ for $m_{3/2} = 500\,\text{GeV}$, at $m_{1/2} = 760\,\text{GeV}$ for $m_{3/2} = 750\,\text{GeV}$, and at $m_{1/2} = 1040\,\text{GeV}$ for $m_{3/2} = 1000\,\text{GeV}$. These thresholds produce distinctive features in the corresponding curves. For very heavy gravitino masses, such as the case $m_{3/2} = 5\,\text{TeV}$ considered here, the dominant two-body decay channels $\tilde{g}\,g$, $\tilde{t}\,t$, $\tilde{\chi}_i^0 Z$ and $\tilde{\chi}^+ W^-$ are kinematically available, even in the focus-point region, so no specific features are observed, and the nucleon fractions are similar in all the scenarios studied.

Finally, we note that various other channels close as $m_{1/2}$ increases, without producing any significant features in the B_p curves. For instance, for $\tan\beta = 10$ (upper left panel in Fig. 5.3), for $m_{3/2} = 250\,\text{GeV}$, the $\tilde{\chi}_1^0 h$ channel closes at $m_{1/2} = 340\,\text{GeV}$. The same occurs for the channels $\tilde{g}g$ and $\tilde{\chi}_1^+ H^-$ when $m_{3/2} = 500\,\text{GeV}$ at $m_{1/2} = 220\,\text{GeV}$, and at $m_{1/2} = 300\,\text{GeV}$ for the channel $\tilde{\chi}_2^+ W^-$. Similarly, for $m_{3/2} = 750\,\text{GeV}$ at $m_{1/2} = 260\,\text{GeV}$, the channel $\tilde{\chi}_2^+ H^-$ closes, and at $m_{1/2} = 340\,\text{GeV}$ the channels $\tilde{g}g$ and $\tilde{\chi_1}^+ H^-$ close. Just to complete the list for this gravitino mass, at $m_{1/2} = 400\,\text{GeV}$ the Higgs boson channels $\tilde{\chi}_1^0 A, H$ close and at $m_{1/2} = 520\,\text{GeV}$ the chargino channel $\tilde{\chi}_2^+ W^-$ closes.

5.2 Constraints on metastable particles

5.2.1 Generic constraints on abundances of metastable particles

Before discussing constraints on specific supersymmetric models with a metastable gravitino, we first discuss constraints on the possible abundance ζ_X of a generic metastable particle X, as a function of its possible lifetime τ_X. We discuss exclusively the constraints due to the effects of the electromagnetic and hadronic showers produced in X decays. Thus, the constraints presented in this Section apply exclusively to *neutral* metastable particles including, but not limited to, the gravitino. Not wishing to commit to any specific model, we give results for two typical values of B_h, which are applicable also outside the context of specific supersymmetric models. Recall, however, that, as noted above, in specific supersymmetric models one may calculate B_h and it is *not*, in general, constant.

The hadronic decays of metastable particles X affect BBN in different ways, depending on the stage of BBN in which the non-thermal decay particles interact with the background thermal nuclei. This effectively divides the decay effects according to the decaying particle's lifetime τ_X.

• Decays much before weak freeze-out ($\tau_X \ll 1$ sec) produce showers that are thermalized before BBN commences. These decays thus have no impact on light-element abundances, and BBN offers no strong constraints on such short-lived decays.

• Decays during weak freeze-out (1 sec $< \tau_X <$ 100 sec) introduce new interactions that may interconvert the neutrons and protons, e.g., via $n\pi^+ \to p\pi^0$. These interactions prolong the $n \leftrightarrow p$ equilibrium, and hence delay the freeze-out of the n/p ratio. In this regime the effect on the light elements is somewhat similar to the addition of relativistic species, with the dominant effect being that on ^{4}He. However, because the upper limit on ^{4}He is weak [95], this effect does not induce a constraint on our particle properties.

• Finally, decays following weak freeze-out ($\tau_X \gg 100$ sec) generate electromagnetic and hadronic showers that induce new (photo)nuclear interactions, which in turn may modify the light-element abundances established previously by BBN.

These processes lead to the constraints seen in Figs. 5.4 - 5.7. These plot abundance contours as a function of pre-decay X abundance ζ_X as in eq. (4.2) and lifetime τ_X, all for decay spectra corresponding to $(m_{1/2}, m_{3/2}, \tan\beta) = (300\,\mathrm{GeV}, 500\mathrm{GeV}, 10)$. In these

and subsequent figures, the white regions in each panel are those allowed at face value by the light-element abundances reviewed in Chapter 3. Specifically, these are: D/H $< 3.2\times10^{-5}$, ^{3}He/D < 1.0 (also shown are dashed lines for ^{3}He/D < 0.3), $Y_{^4\mathrm{He}} > 0.240$, ^{6}Li/^{7}Li < 0.05, and ^{7}Li/H $< 2.75 \times 10^{-10}$. The latter constraint comes from ^{7}Li in globular clusters, and we also demarcate by a dashed line the region within the white area where ^{7}Li/H $< 1.91 \times 10^{-10}$ (the errors represent a 95% CL) as inferred from field stars. The yellow, red, and magenta regions correspond to progressively larger deviations from the central values of the abundances as noted on the figures. Fig. 5.4 shows the constraints when the effects of both hadronic and electromagnetic decays are included. To give a sense of how the various decay modes contribute, Fig. 5.5 shows constraints when hadronic effects are omitted, and only electromagnetic decays are included. Figs. 5.6 (Fig. 5.7) both omit effects of electromagnetic decays, and include only hadronic decays to neutrons (protons).

The basic features of these plots are similar to those found in previous work, but for completeness we summarize them here. In all plots, we see that at low ζ_X, all constraints are satisfied except for ^{7}Li. This is reasonable, as in the limit of $\zeta_X \to 0$ we recover the standard BBN abundances, which agree well with observations except for the ^{7}Li problem which persists. Also, we see a similar behavior in all plots for small $\tau_X \lesssim 10^2$ sec. Here, the decays occur after weak freezeout but before light element formation occurs, and so for the most part the abundances are unaffected; the main exception is perturbations in ^{4}He due to pion interactions delaying $n \leftrightarrow p$ freezeout.

For several elements the basic trends at $\tau_X \gtrsim 10^2$ sec are relatively simple. We begin with ^{4}He, which is the only species for which decays always lead to reduced abundances. This is physically reasonable, since ^{4}He is the most abundant complex species, and the non-thermal reactions represent sinks but not sources. That is, photoerosion and spallation destroy ^{4}He, but X decays cannot produce it; hence ^{4}He drops as ζ_X increases. On the other hand, we see that decays increase the D/H abundance, which is readily understood physically. Destruction of ^{4}He produces deuteron fragments, some of which are thermalized before interacting and thus survive. Because ^{4}He is so abundant, even if only a small fraction of ^{4}He is destroyed, the resulting deuteron production can be significant. For ^{6}Li/^{7}Li, the basic trend is also towards increasing production with increasing ζ_X. Here, not-yet-thermalized mass-3 fragments can interact with ambient

^{4}He to produce ^{6}Li via $^3\mathrm{He}(\alpha, p)^6\mathrm{Li}$ and $t(\alpha, n)^6\mathrm{Li}$. Again, even if only a small fraction of $A = 3$ nuclei interact this way, this can represent a substantial ^{6}Li abundance compared to observational limits. Moreover, while other secondary processes also contribute to ^{7}Li, the much larger effect is for ^{6}Li, so that the $^6\mathrm{Li}/^7\mathrm{Li}$ ratio increases with ζ_X.

By comparing the full constraints (Fig. 5.4) with those in the electromagnetic-only case of Fig. 5.5, we see illustrated the well-known result that the electromagnetic decays dominate at $\tau_X \gtrsim 10^6$ sec, but are ineffective at smaller times [111]. Again for D/H, ^{7}Li/H, and ^{3}He/D, we see that the hadronic effects from neutrons and protons (Figs. 5.6 and 5.7, respectively) are broadly similar, though the neutron constraints are generally more restrictive out to about $\tau_X \sim 10^6$ sec. This is the timescale for neutron decay to outpace other neutron interactions.

The cases of ^{7}Li and ^{3}He/D are more complicated. Turning to ^{7}Li in Fig. 5.4, we see that at intermediate lifetimes ($\sim 10^4$ sec), decays lead to higher ^{7}Li/H; this is due to secondary production from unthermalized mass-3 spallation products, $^3\mathrm{He}(\alpha, \gamma)^7\mathrm{Be}$ and $t(\alpha, \gamma)^7\mathrm{Li}$. However, at lifetimes around $\tau_X \sim 10^2 - 10^3$ sec, there a narrow 'valley' emerges in which ^{7}Li/H is *reduced*, indeed enough to come into agreement with observational limits. By comparing Figs. 5.6 and 5.7, we see that this effect is entirely due to injected neutrons, and is absent when only proton decays are included. This suggests that neutrons are destroying ^{7}Be, and that is indeed the case. As noted already by Jedamizk and in subsequent work [37, 38, 39], thermalized neutrons can destroy ^{7}Be via $^7\mathrm{Be}(n, p)^7\mathrm{Li}$ and followed by $^7\mathrm{Li}(p, \alpha)^4\mathrm{He}$. We include this effect, but also we allow for further ^{7}Be destruction in which the same reactions are initiated by injected neutrons not yet thermalized. This addition slightly enhances the low-^{7}Li/H 'valley'. Notice that the left side of the 'valley' coincides almost exactly with the constraint from D/H, so that we find $\mathrm{D/H} > 3.2 \times 10^{-5}$ in essentially the entire region where $^7\mathrm{Li/H} < 2.75 \times 10^{-10}$. However, along the left side of the 'valley' in Fig. 5.4, there may be a marginal solution to the ^{7}Li problem, to which we return later in the context of the CMSSM.

Finally, turning to ^{3}He/D at low lifetimes, we also see a reduction in the ratio for large ζ_X, with a particularly large effect in the neutron-only case. As with ^{7}Li destruction, here the free neutrons preferentially capture on t and ^{3}He. This leads to a small ^{3}He/D ratio as ζ_X increases. Specifically, we see that $^3\mathrm{He/D} < 0.3$ in the narrow

strip in Figs. 5.4 and 5.6 where the ^{7}Li may (almost) be solved.

5.2.2 Constraints on the abundance of a massive gravitino

We now apply the above analysis to the specific class of supersymmetric scenarios with a metastable massive gravitino and a neutralino LSP χ.

We recall that neutralino LSP scenarios are characterized by narrow strips along which the relic χ density lies within the range $0.0975 < \Omega_{\rm CDM}h^2 < 0.1223$ that is favored by WMAP and other observations [78]. Since this range is relatively narrow (namely only a few %), within any specific supersymmetric scenario it determines some combination of the model parameters also to within $\mathcal{O}$(few) %. A more detailed discussion is given in [125], where some explicit parameterizations of such WMAP strips are given. In the examples given there, the value of m_0 is tightly determined in CMSSM scenarios as a function of $m_{1/2}$ for fixed values of $\tan\beta$ and A_0. Many properties of these supersymmetric models change little as one varies m_0 across such a narrow WMAP strip. Specifically, the branching ratios for massive gravitino decay and hence B_h vary little across a strip, and one may usefully represent the cosmological constraints on such CMSSM scenarios as functions of $m_{1/2}$ alone, using a representative value of B_h that is calculated as a function of $m_{1/2}$.

One representative example is shown in Fig. 5.8: the first five panels, with shadings, display the effects of the decays of a gravitino with a mass $m_{3/2} = 250$ GeV on the different light-element abundances (D/H, ^{3}He/D, ^{4}He, ^{6}Li/^{7}Li and ^{7}Li/H) as functions of $m_{1/2}$ along the WMAP strip in the coannihilation region for a CMSSM scenario with $\tan\beta = 10, A_0 = 0$. As in Fig. 5.4 - 5.7, the white regions in each panel are those allowed at face value by the ranges of the light-element abundances reviewed in Chapter 3, and the yellow, red, and magenta regions correspond to progressively larger deviations from the central values of the abundances. The final panel (bottom right), shows the strongest constraints from each abundance, as labeled, and from these one infers the strongest overall constraint, shown by the thick black curve.

We first note that all constraints weaken abruptly as $m_{1/2} \to 600$ GeV. This corresponds to the limiting case when $m_\chi \sim 0.42 m_{1/2} \to m_{3/2} = 250$ GeV. In this limit, the energies in the EM and HD showers vanish, and the effects of gravitino decay disappear. Note that $m_{1/2} = 250$ GeV is the smallest value we consider; for larger values this effect

is less important.

Consider now the D/H constraints in the region $m_{1/2} \lesssim 600$ GeV in the top left panel of Fig. 5.8. We see that the lowest contour, at D/H $= 3.2 \times 10^{-5}$, lies at about $\zeta_{3/2} \simeq 10^{-11}$ GeV between $m_{1/2} = 180$ GeV and just under 600 GeV [1] . To understand this behavior, we recall from Fig. 5.1 that for $m_{1/2} = 180 - 580$ GeV, the gravitino lifetime grows from about 10^7 sec to 10^{10} sec, and in Fig. 5.3 we see that the nucleon branching ratios $B_p \approx B_n \sim 6 \times 10^{-2}$ for $m_{1/2} \lesssim 400$ GeV. Combining these with the generic lifetime dependence in Fig. 5.4, we see that for $B_p \approx B_n \sim 2 \times 10^{-1}$, the lowest D/H contour for $\tau \gtrsim 10^7$ sec is roughly constant at $\zeta_{3/2} \sim 3 \times 10^{-12}$ GeV. In our case, these constraints weaken due to the lower branching ratios by a factor ~ 3, yielding the value $\zeta_{3/2} \sim 10^{-11}$ GeV seen in Fig. 5.8. The higher D/H contours in Fig. 5.8 can be understood in a similar manner.

As another example, consider the ^{7}Li/H panel in the bottom middle panel of Fig. 5.8. There we see, for $m_{1/2} \lesssim 600$ GeV, an 'island' of the lowest constraint where $\zeta_{3/2} \sim 10^{-10} - 10^{-8}$ GeV. As $\zeta_{3/2}$ drops, ^{7}Li/H then grows, peaking to highest level where $\zeta_{3/2} \sim 3 \times 10^{-9}$ GeV. Then as $\zeta_{3/2}$ continues to decrease, ^{7}Li/H continues drops down to its standard BBN level. From the generic plot Fig. 5.4, we see that for $\tau \gtrsim 10^7$ sec and with $B_p \sim 0.2$, the ^{7}Li/H constraint forms an island around $\zeta_{3/2} \sim 10^{-9}$ GeV, with a width that grows with τ. Scaling down to the lower branching, we again can understand the behavior in Fig. 5.8.

The fact that this qualitative analysis works so well indicates that the generic results are a good approximation to the full ones, modulo changes in branching ratios. However, the generic results are for a particular decay spectrum whereas, as we have seen, there are significant variations in the decay spectrum. Thus we infer that our results are not strongly dependent on the detailed shapes of the decay spectra beyond the sensitivity to the branching ratios. This also makes sense in terms of our analytic approximations developed in Section 3.3, 3.4 and 5.2 of [47], which suggest that the decay spectra enter principally via their integral properties and particularly their branching ratios.

This understanding of the non-thermal particle effects leading to our constraints gives confidence in our results, and thus to their implications for supersymmetry. Namely,

[1] We recall that the gravitino becomes the LSP for $m_{1/2} \gtrsim 600$ GeV, in which case a different analysis is necessary.

again in the case of Fig. 5.8 where $\tan\beta = 10$ and $m_{3/2} = 250$ GeV, the fact that the observed abundances generally agree with the standard BBN calculations implies that the allowed (white) regions are generally at low gravitino abundance. The exception is the bottom middle panel, where the observational discrepancy with the standard BBN calculation of the ^{7}Li abundance is reflected in the fact that the yellow region extends from a vanishing gravitino abundance up to quite large values, and the 'preferred' white region appears only when $\zeta_{3/2} > 10^{-9}$ GeV and $m_{1/2}$ is not too large [2] . It is clear that this 'preferred' region for ^{7}Li/H is incompatible with the allowed regions for the other light-element abundances shown in the other panels. Thus, there is no value of $m_{1/2}$ in this particular CMSSM scenario that solves the ^{7}Li/H problem. We disregard the ^{7}Li/H problem in the compilation of constraints shown in the bottom right panel of Fig. 5.8, and in the following discussion.

The weakening of the constraints as $m_{1/2} \to 600$ GeV implies that a large abundance is allowed for $m_{3/2} = 250$ GeV if $m_{1/2} \sim 600$ GeV, apart from the issue of the ^{7}Li abundance. We recall that if $m_{1/2} > 600$ GeV with fixed $m_{3/2} = 250$ GeV, the gravitino becomes the LSP and the lightest neutralino becomes the NLSP. In this case, the constraint due to the cosmological relic density should be applied to the gravitino, the WMAP strip is no longer relevant, and a different analysis would be required.

In the final, summary panel of Fig. 5.8 (bottom right), we see explicitly that the ^{7}Li constraint (light blue) is incompatible with the other constraints due to ^{4}He (green), D/H (magenta), ^{3}He/D (red) and ^{6}Li/^{7}Li (dark blue). The weakest of these constraints is that due to ^{4}He, the two strongest constraints at smaller and larger $m_{1/2}$, respectively, are those due to ^{6}Li/^{7}Li and ^{3}He/D, and the combined constraint is shown in black. We see that it hovers in the range $\zeta_{3/2} = m_{3/2}n_{3/2}/n_\gamma \sim 3 \times 10^{-12}$ to 10^{-12} GeV, corresponding to $n_{3/2}/n_\gamma \sim 10^{-14}$, except in the limit as $m_{1/2} \to 600$ GeV.

Figs. 5.9, 5.10, 5.11, and 5.12 show the correspondingly coloured regions of varying discomfort for the different light-element abundances for the larger values of $m_{3/2} =$ 500 GeV, 750 GeV, 1000 GeV and 5000 GeV, respectively. The constraints are shown for the full length of the WMAP strip up to $m_{1/2} \sim 900$ GeV, along which $m_\chi < m_{3/2}$ for all the displayed values of $m_{3/2}$. For $m_{3/2} \leq 1000$ GeV, we see that the D/H

[2] We also note the existence of a more disfavored (red) region in the bottom middle panel showing the ^{7}Li/H ratio, appearing when $\zeta_{3/2} > 10^{-9}$ GeV and $m_{1/2} \sim 500$ GeV.

constraint (top left panel in each plot) and the ^{4}He constraint (top right in each plot) are relatively stable, reflecting the rough constancy of the D/H results for long lifetimes (see Fig. 5.4), and the rough constancies of the branching ratios (see Fig. 5.3). For $m_{3/2} = 5000$ GeV, the short lifetimes (see Fig. 5.1) severely weaken the constraints for all elements (cf. Fig. 5.4), with D/H surviving as the strongest for all $m_{1/2}$. We discuss later the case of large $m_{3/2}$.

In the case of ^{7}Li/H (bottom middle panels), the 'preferred' white region changes position as $m_{3/2}$ increases, moving to larger $m_{1/2}$ for $m_{3/2} = 500, 750$ GeV, but reverting to low $m_{1/2}$ at high $m_{3/2}$. The $m_{1/2}$ mass ranges are those which have lifetimes near $\sim 3 \times 10^6$ sec (see Fig. 5.4), whereas the ^{7}Li constraint is strongest for long lifetimes. However, there is no overlap between the white regions in this and the other panels, implying that the ^{7}Li problem cannot be solved for any value of $m_{3/2}$ for the particular values of $\tan\beta$ and A_0 chosen here. As stated previously, we do not include the ^{7}Li constraint in our compilation. As ^{7}Li is problematic in standard BBN, the inclusion of this constraint would give the false impression that nearly every supersymmetric model with a decaying gravitino is excluded. We are therefore implicitly assuming that there is another solution for the ^{7}Li problem, e.g., due to observational or astrophysical uncertainties as discussed in Section 3.2. In contrast, the constraints from the other light elements perturb the previous concordance of BBN with respect to those elements.

Finally, we note that for $m_{3/2} = 500$ to 1000 GeV, the ^{6}Li/^{7}Li constraint is significantly stronger than for $m_{3/2} = 250$ GeV, becoming progressively stricter. This reflects the stronger limits arising when the gravitino lifetime is shorter (see Fig. 5.4). In all cases the ^{6}Li/^{7}Li ratio provides the most restrictive limit on $\zeta_{3/2}$, and strengthens by a factor ~ 10 as $m_{1/2}$ increases from 250 to 1000 GeV. Specifically, we find $\zeta_{3/2} \lesssim 10^{-12} - 10^{-11}$ GeV for $m_{3/2} = 500$ GeV, $\zeta_{3/2} \lesssim 3 \times 10^{-13} - 3 \times 10^{-12}$ GeV for $m_{3/2} = 750$ GeV, and $\zeta_{3/2} \lesssim 10^{-13} - 10^{-12}$ GeV for $m_{3/2} = 1000$ GeV.

In the case of Fig. 5.12, we see that the most significant upper limit on the gravitino abundance is that from D/H. Comparing this with the *lower* limit on the gravitino abundance coming from ^{7}Li/H, we see that they are marginally compatible over essentially the full range of $m_{1/2}$ displayed. However, this conclusion is crucially dependent on the precise implementations of the D/H and ^{7}Li/H constraints: for example, if the upper limit on the ^{7}Li/H abundance is strengthened to 1.91×10^{-10}, as suggested by field stars

and indicated by the dashed line in the middle lower panel of Fig. 5.12, compatibility becomes more difficult.

Figs. 5.13 - 5.17 are the same as Figs. 5.8 - 5.12, but for $\tan\beta = 50$. Similar trends emerge as for the $\tan\beta = 10$ results, with some differences of detail due to the more rapid rise in lifetimes with $m_{1/2}$ (Fig. 5.1). The range in $m_{1/2}$ is extended to almost 1.9 TeV and includes the rapid annihilation funnel in addition to the coannihilation region. We again see that no regions allow for a solution to the ^{7}Li problem while simultaneously satisfying the other light-element constraints. The constraints on $\zeta_{3/2}$ are again dominated by the ^{6}Li/^{7}Li ratio, and are weak for $m_{3/2} = 5000$ GeV. As in the $\tan\beta = 10$ case, the ^{7}Li/H constraint is incompatible with the others for $m_{3/2} \leq 1000$ GeV, but may be marginally compatible for $m_{3/2} = 5000$ GeV.

Figs. 5.18 - 5.22 present a similar analysis to that in Figs. 5.8 - 5.12, but for the focus-point region of the CMSSM with $\tan\beta = 10$. The results are also largely similar to those for the previous cases. The same is true for the focus-point region of the CMSSM with $\tan\beta = 50$, shown in Fig. 5.23 - 5.27. As in the previous cases, the ^{7}Li/H constraint is incompatible with all the other constraints, except possibly for $m_{3/2} = 5000$ GeV.

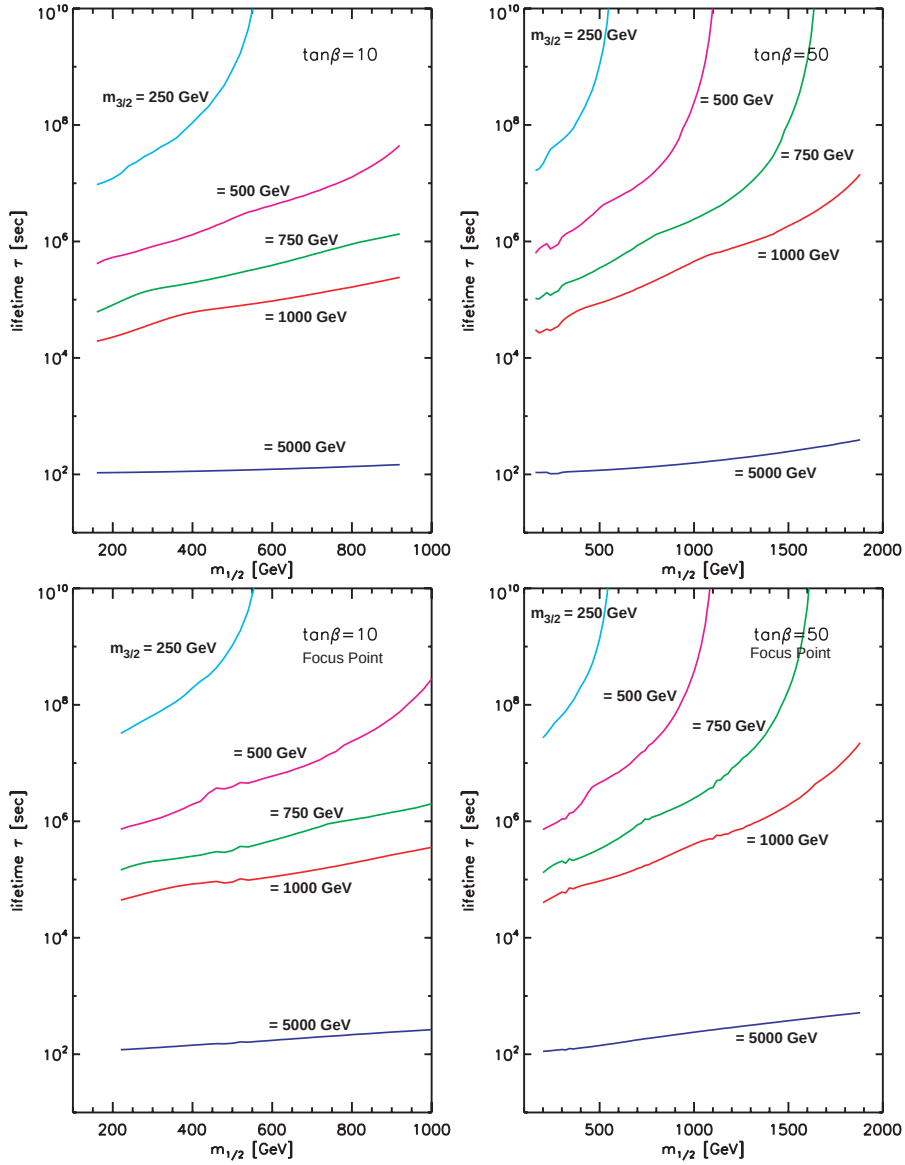

Figure 5.1: The gravitino lifetime for representative values of $m_{3/2}$ as a function of $m_{1/2}$ for $\tan\beta = 10$ (left) and $\tan\beta = 50$ (right) along WMAP strips, in the coannihilation and funnel region (top) and the focus-point region (below).

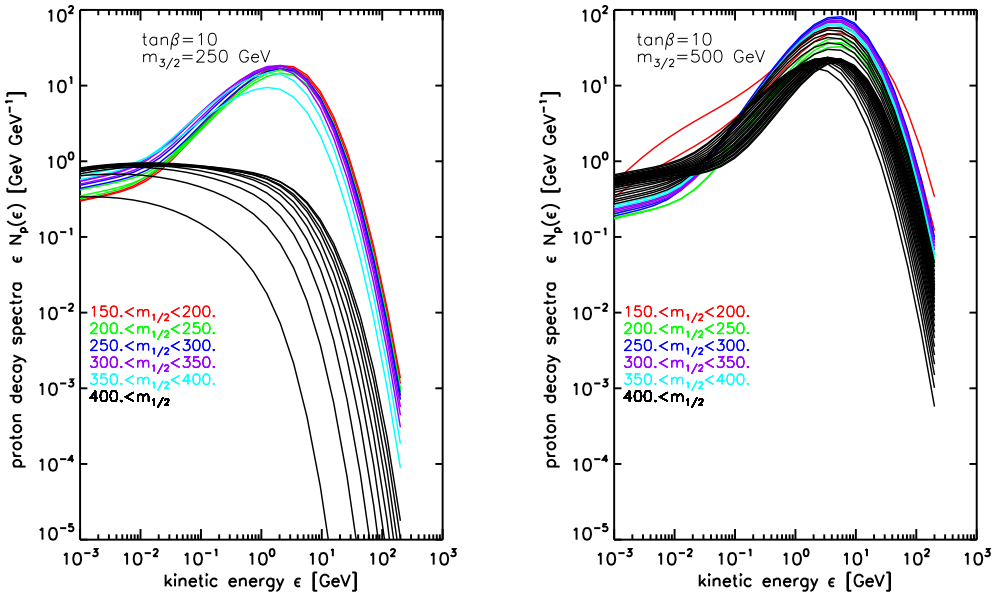

Figure 5.2: Sample spectra for gravitino decays into protons. We plot values of the combination $\epsilon\ N_p(\epsilon)$, which gives the particle number per logarithmic energy range, for different representative values of the gaugino mass parameter $m_{1/2}$ along the coannihilation strip for $\tan\beta = 10$, assuming the indicated values of the gravitino mass $m_{3/2}$.

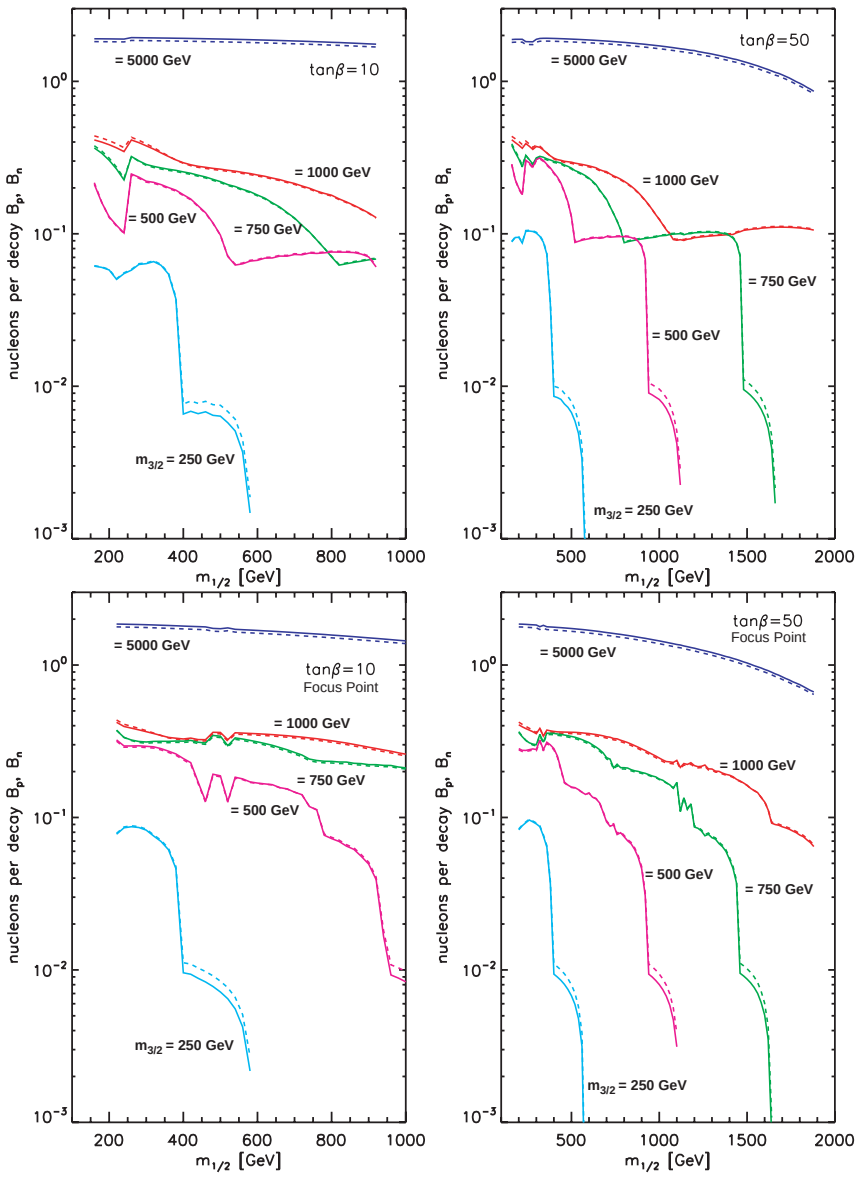

Figure 5.3: The number of nucleons per gravitino decay, as a function of $m_{1/2}$ for $\tan\beta = 10$ (left) and $\tan\beta = 50$ (right). The upper panels are for WMAP strips in the coannihilation and rapid-annihilation regions, and the lower panels are for WMAP strips in the focus-point regions. Solid curves: number B_p of protons per decay. Broken curves: number B_n of neutrons per decay. We see that generally $B_p \approx B_n$ to a good approximation.

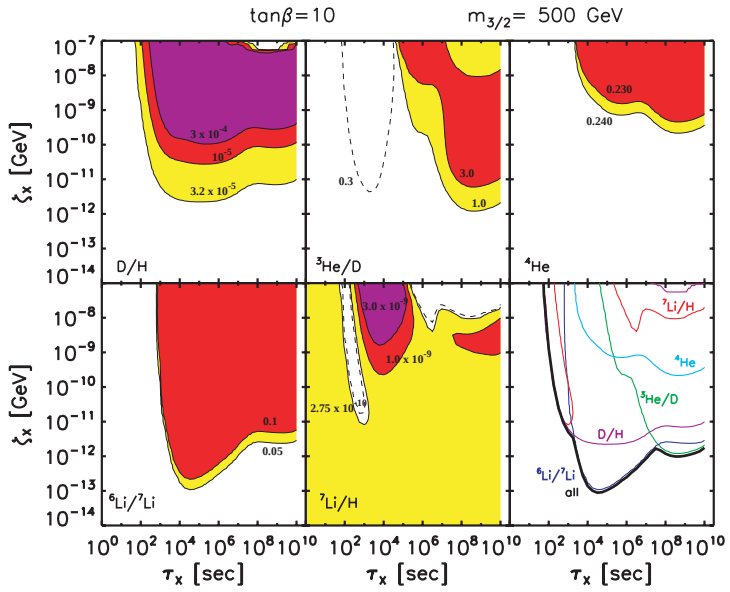

Figure 5.4: Plots of abundance versus lifetime for metastable particles X with lifetimes τ_X between 1 and 10^{10} sec, assuming the decay spectra calculated for $(m_{1/2}, m_{3/2}, \tan\beta) = (300\ \text{GeV}, 500\ \text{GeV}, 10)$, in which case $B_p \approx 0.2$ and the electromagnetic branching is $B_{\rm EM} m_{3/2} = 115$ GeV. The X abundance before decay is given by $\zeta_X = m_X n_X / n_\gamma$ (eq. 4.2). The white regions in each panel are those allowed at face value by the ranges of the light-element abundances reviewed in Chapter 3, whilst the yellow, red and magenta regions correspond to progressively larger deviations from the central values of the abundances.

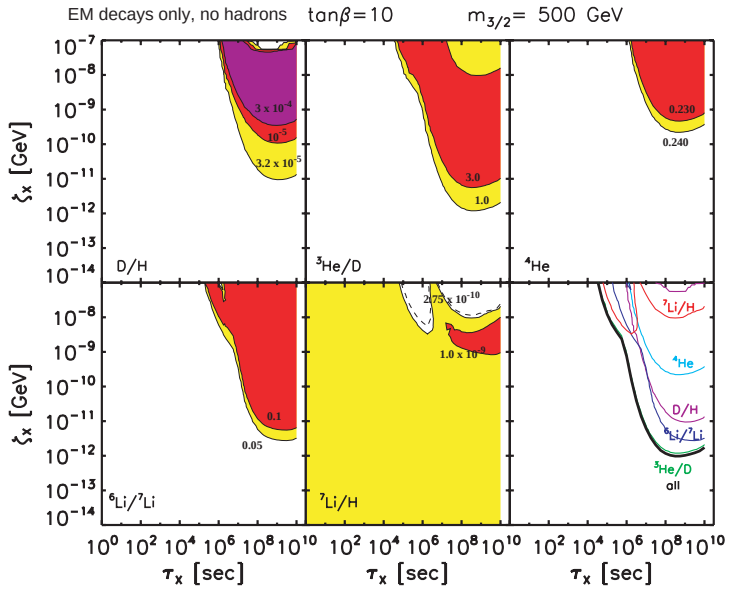

Figure 5.5: As in Fig. 5.4, but with electromagnetic decay products only. All hadronic showers and resulting interactions with light elements are ignored.

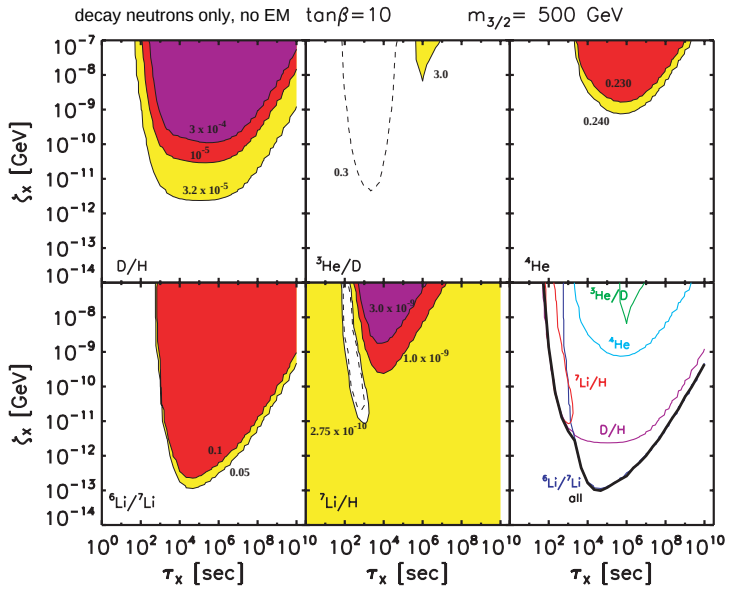

Figure 5.6: As in Fig. 5.4, but only with decay neutrons. Decay protons and electromagnetic particles are ignored.

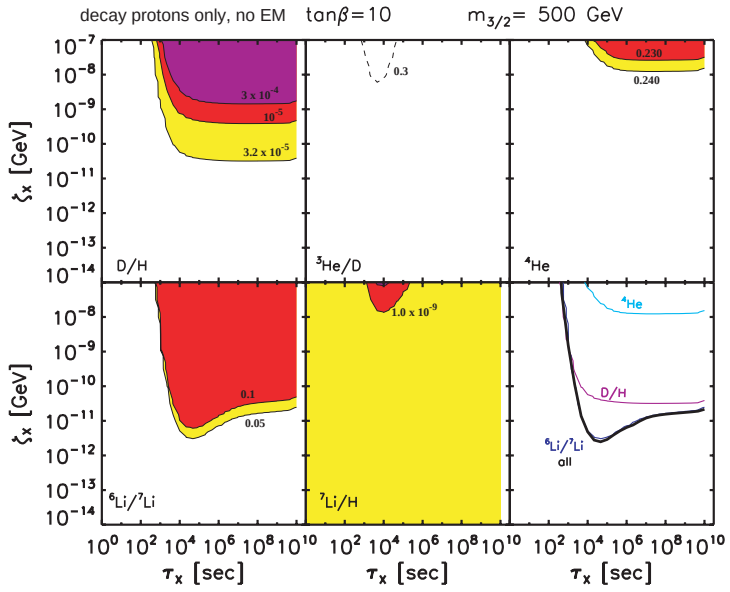

Figure 5.7: As in Fig. 5.4, but only with decay protons. Decay neutrons and electromagnetic particles are ignored.

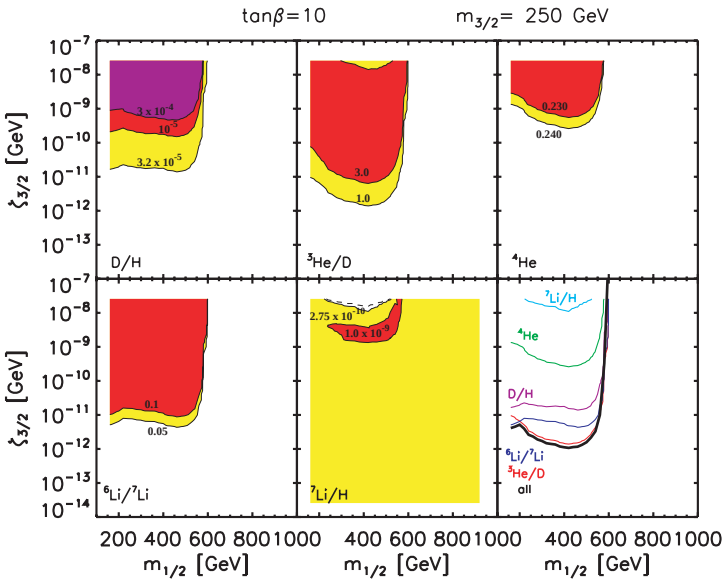

Figure 5.8: The effects of the decays of a gravitino with a mass $m_{3/2} = 250$ GeV on the different light-element abundances (D/H, ^{3}He/D, ^{4}He, ^{7}Li/H and ^{6}Li/^{7}Li) as a function of $m_{1/2}$ along the WMAP coannihilation strip for a CMSSM scenario with $\tan\beta = 10, A_0 = 0$. As in Figs. 5.4, the white regions in each panel are those allowed at face value by the light-element abundances reviewed in Chapter 3, and the yellow, red, and magenta regions correspond to progressively larger deviations from the central values of the abundances.

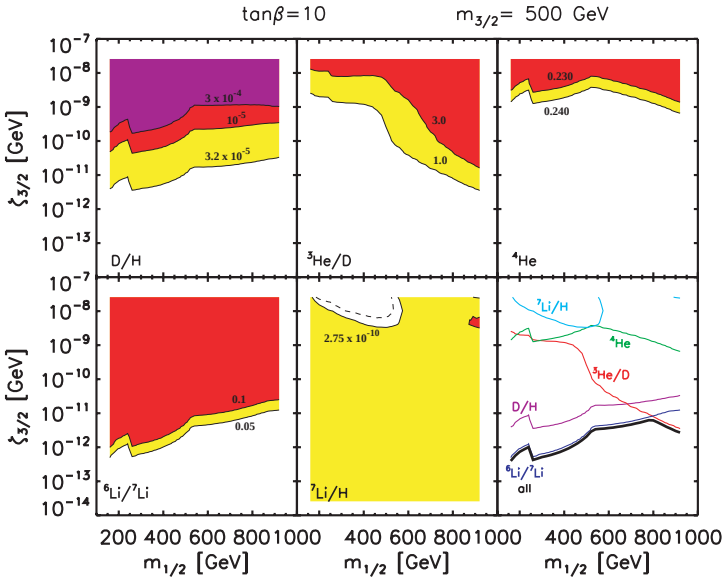

Figure 5.9: As for Fig. 5.8, with $m_{3/2} = 500$ GeV but unchanged values for the CMSSM parameters.

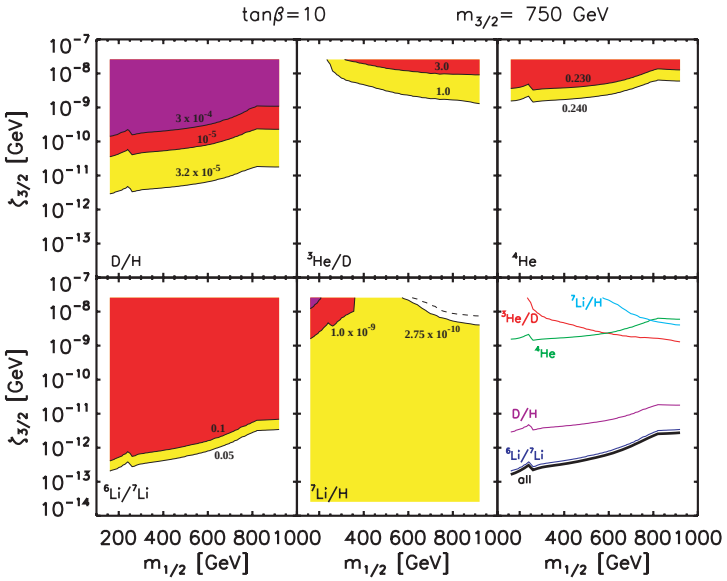

Figure 5.10: As for Fig. 5.8, with $m_{3/2} = 750$ GeV but unchanged values for the CMSSM parameters.

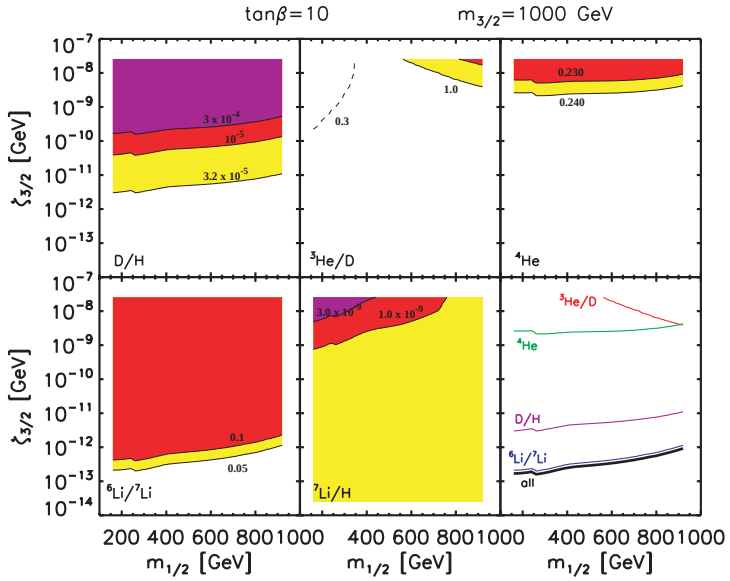

Figure 5.11: As for Fig. 5.8, with $m_{3/2} = 1000$ GeV but unchanged values for the CMSSM parameters.

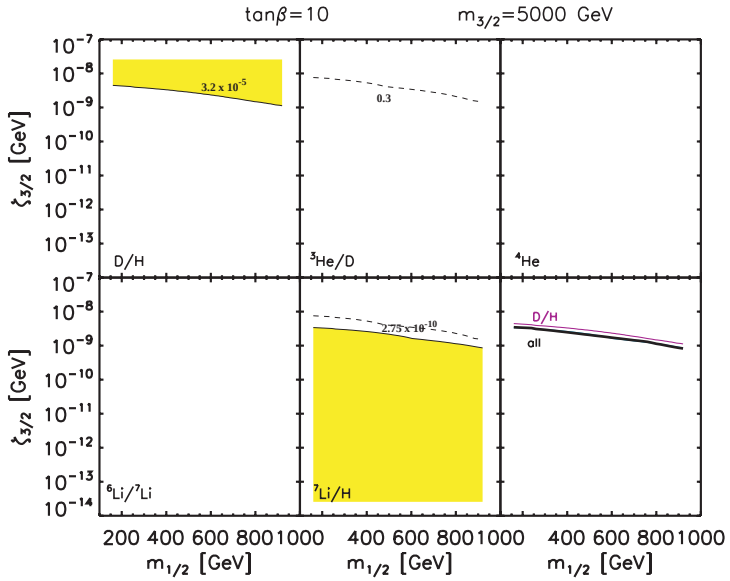

Figure 5.12: As for Fig. 5.8, with $m_{3/2} = 5000$ GeV but unchanged values for the CMSSM parameters.

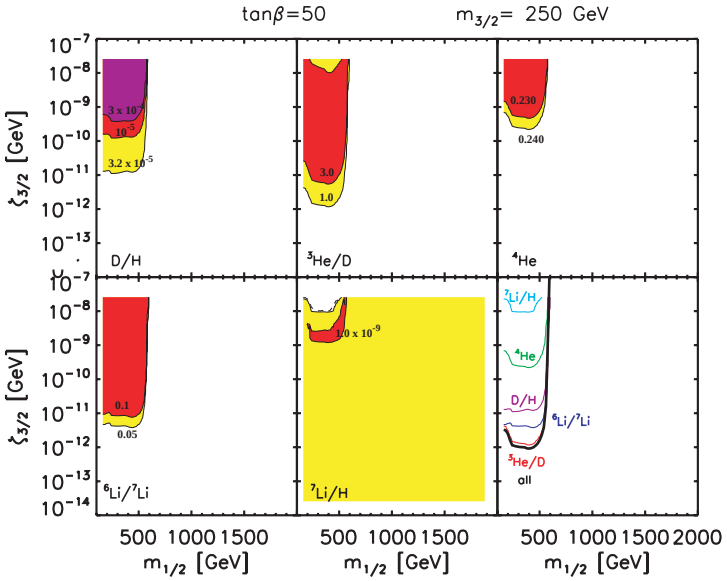

Figure 5.13: As for Fig. 5.8, with $m_{3/2} = 250$ GeV, but $\tan\beta = 50$ and unchanged values for the CMSSM parameters.

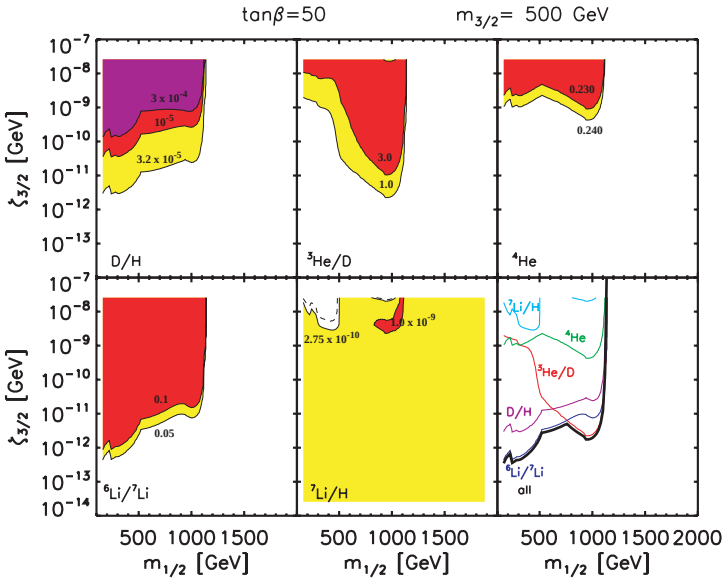

Figure 5.14: As for Fig. 5.8, with $m_{3/2} = 500$ GeV, but $\tan\beta = 50$ and unchanged values for the CMSSM parameters.

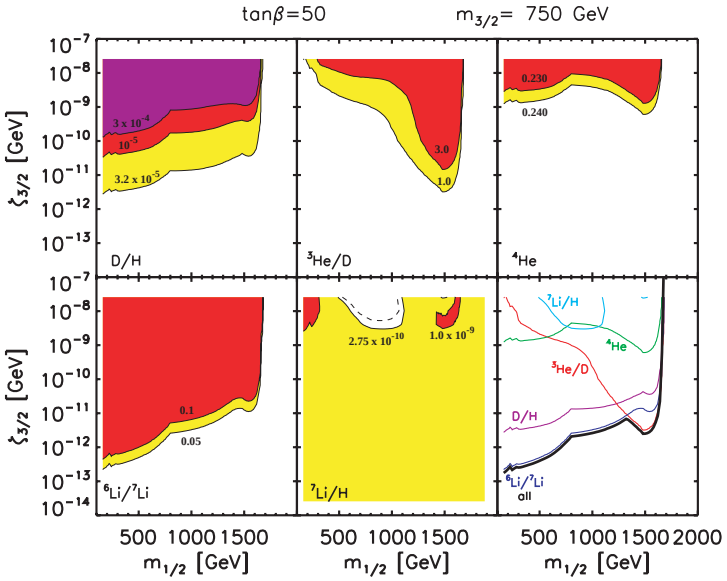

Figure 5.15: As for Fig. 5.8, with $m_{3/2} = 750$ GeV, but $\tan\beta = 50$ and unchanged values for the CMSSM parameters.

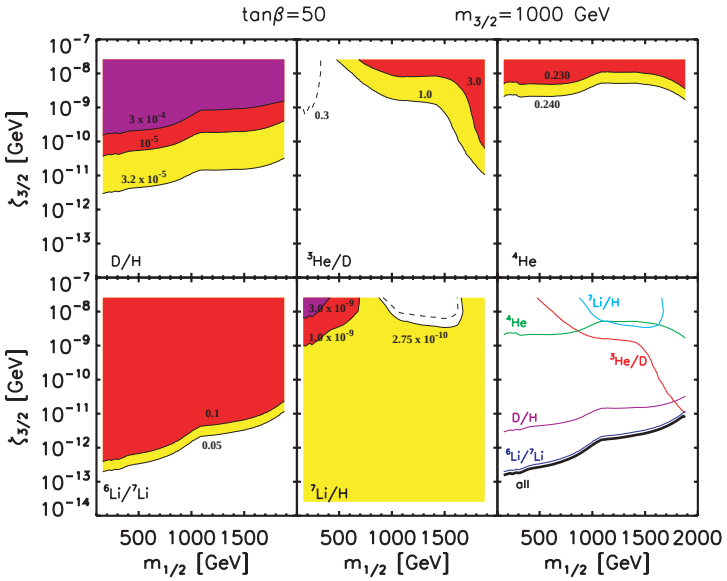

Figure 5.16: As for Fig. 5.8, with $m_{3/2} = 1000$ GeV, but $\tan\beta = 50$ and unchanged values for the CMSSM parameters.

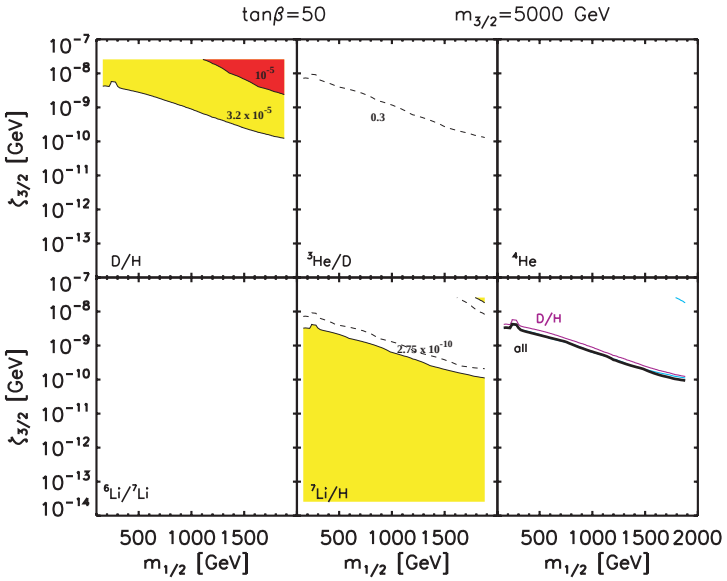

Figure 5.17: As for Fig. 5.8, with $m_{3/2} = 5000$ GeV, but $\tan\beta = 50$ and unchanged values for the CMSSM parameters.

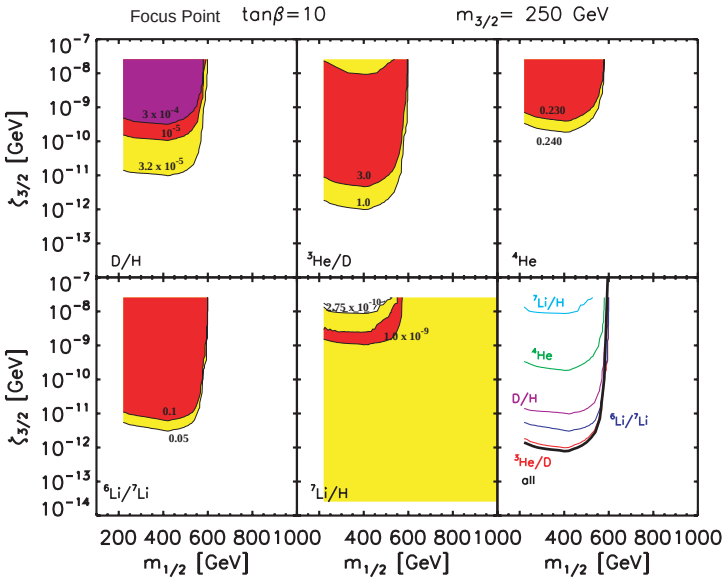

Figure 5.18: As for Fig. 5.8, with $m_{3/2} = 250$ GeV, but $\tan\beta = 10$ and CMSSM parameters appropriate for the WMAP strip in the focus-point region.

5.2.3 Varying $m_{3/2}$ and the ^{7}Li problem

The previous plots displayed the gravitino constraints along WMAP strips in the $(m_{1/2}, m_0)$ planes for a few discrete choices of $m_{3/2}$. We now display some results as continuous functions of $m_{3/2}$ for a few WMAP-compatible points with certain discrete values of $m_{1/2}$. Fig. 5.28 shows our first choice, $m_{1/2} = 400$ GeV and $\tan\beta = 10$, in which case the WMAP point is essentially benchmark point C defined in [125]. As expected from the previous figures, we see that the other light-element constraints are incompatible with the ^{7}Li/H constraint for low $m_{3/2}$. Disregarding the ^{7}Li problem, we find, e.g., an upper limit on $\zeta_{3/2} \sim 10^{-13}$ when $m_{3/2} \sim 1.4$ TeV. However, marginal compatibility with the cosmological ^{7}Li abundance is approached for $m_{3/2} \gtrsim 3$ TeV with $\zeta_{3/2} > 10^{-11}$ GeV, as was to be expected from Fig. 5.12. This is a realization within the CMSSM of the marginal compatibility between the ^{7}Li abundance and the D/H ratio that was noted earlier in the context of Fig. 5.4.

Figs. 5.29, 5.30 and 5.31 display similar features for other choices of WMAP-compatible benchmark points [125]. In the case of Fig. 5.29, we choose benchmark point L with

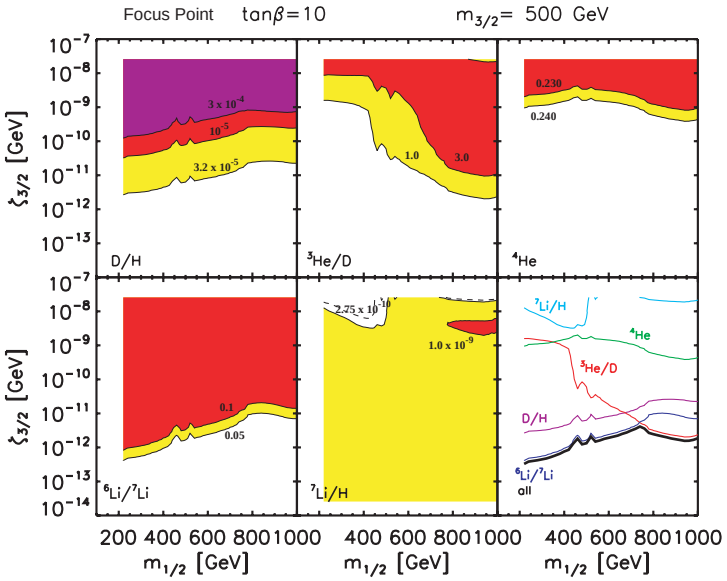

Figure 5.19: As for Fig. 5.8, with $m_{3/2} = 500$ GeV, but $\tan\beta = 10$ and CMSSM parameters appropriate for the WMAP strip in the focus-point region.

$m_{1/2} = 460$ GeV and $\tan\beta = 50$, which is also in a coannihilation strip. We see very similar features to Fig. 5.28, e.g., an upper limit on $\zeta_{3/2} \sim 2 \times 10^{-13}$ GeV when $m_{3/2} \sim 1.6$ TeV if the ^{7}Li constraint is disregarded, and a marginal solution of the ^{7}Li problem for $m_{3/2} \gtrsim 3$ TeV with $\zeta_{3/2} > 10^{-11}$ GeV. Fig. 5.30 is based on benchmark point M with $m_{1/2} = 1840$ GeV and $\tan\beta = 50$, which is in a rapid-annihilation funnel. The features seen in the previous figures shift to higher $m_{3/2}$, e.g., we see an upper limit on $\zeta_{3/2} \sim 10^{-12}$ GeV when $m_{3/2} \sim 2.4$ TeV if the ^{7}Li constraint is disregarded, and a marginal solution of the ^{7}Li problem for $m_{3/2} \gtrsim 4$ TeV with $\zeta_{3/2} > 5 \times 10^{-11}$ GeV. Finally, Fig. 5.31 is based on benchmark point E with $m_{1/2} = 300$ GeV and $\tan\beta = 10$, which is in a focus-point region. We see in general results that are very similar to those for benchmark point C shown in Fig. 5.28.

The stability of the marginal 'solution' of the ^{7}Li problem reflects the fact that the gravitino lifetime $\sim 10^2 - 10^3$ s and the number of nucleons per decay are relatively stable for heavy gravitino masses as $m_{1/2}$ and $\tan\beta$ are varied: see Figs 5.1 and 5.3. The underlying physics of this marginal 'solution', as discussed in [37, 38, 39], is that for this range of gravitino lifetimes, thermalized neutrons can destroy ^{7}Be via $^7\mathrm{Be}(n,p)^7\mathrm{Li}$,

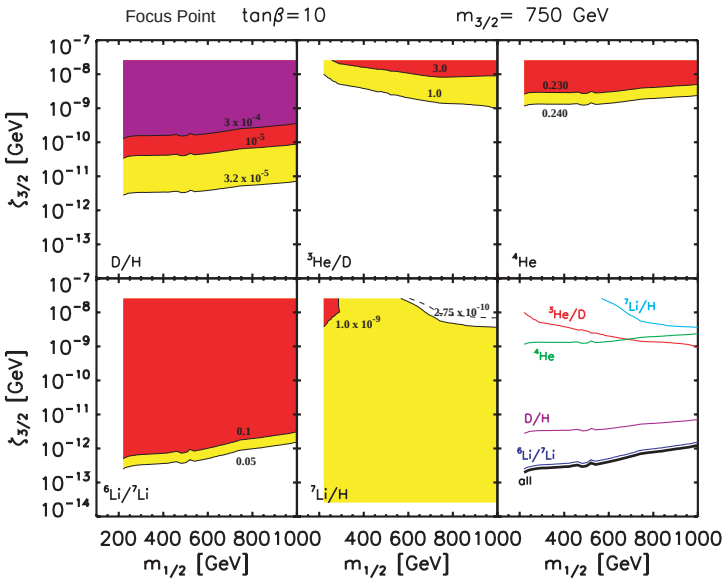

Figure 5.20: As for Fig. 5.8, with $m_{3/2} = 750$ GeV, but $\tan\beta = 10$ and CMSSM parameters appropriate for the WMAP strip in the focus-point region.

following which ^{7}Li is destroyed by the $^7\mathrm{Li}(p,\alpha)^4\mathrm{He}$ reaction. Here, as discussed in Appendix A of [47], we also allow for supplementary ^{7}Be destruction by non-thermalized neutrons.

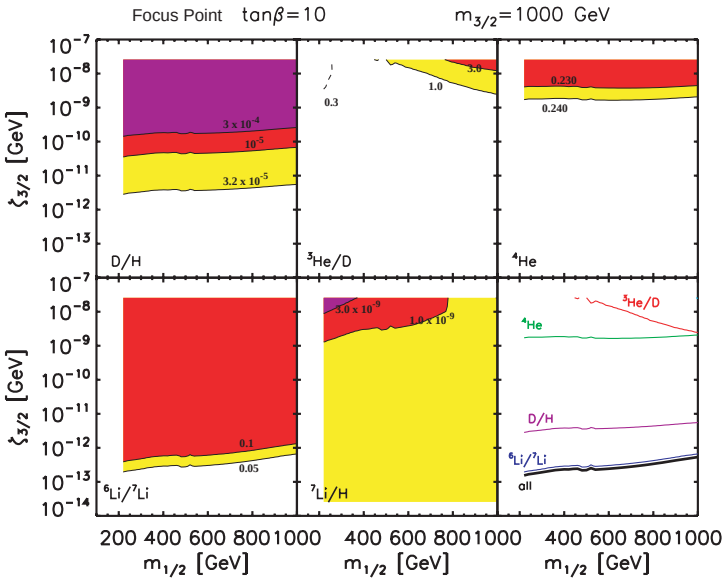

Figure 5.21: As for Fig. 5.8, with $m_{3/2} = 1000$ GeV, but $\tan\beta = 10$ and CMSSM parameters appropriate for the WMAP strip in the focus-point region.

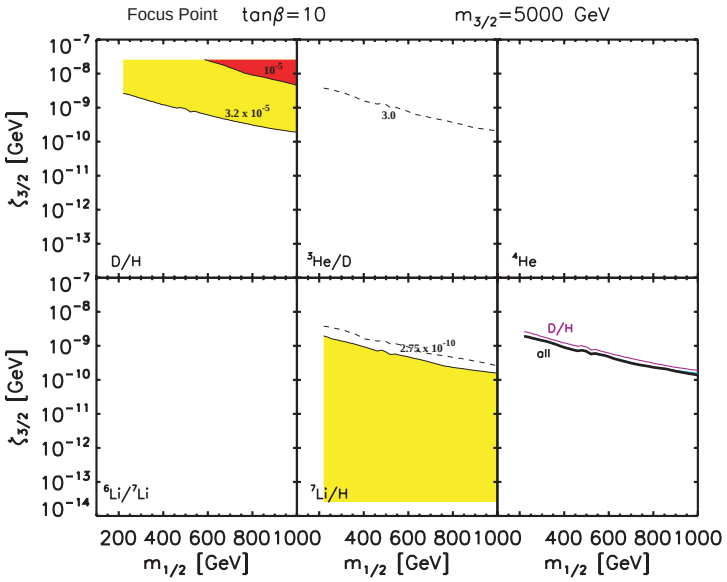

Figure 5.22: As for Fig. 5.8, with $m_{3/2} = 5000$ GeV, but $\tan\beta = 10$ and CMSSM parameters appropriate for the WMAP strip in the focus-point region.

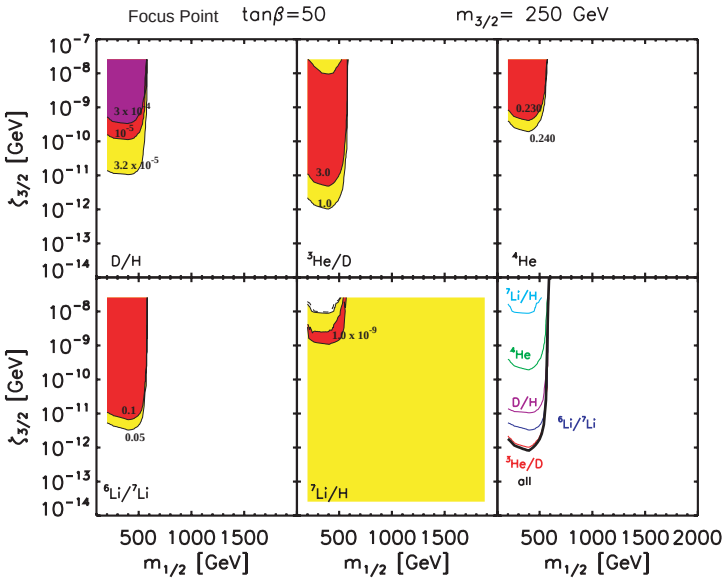

Figure 5.23: As for Fig. 5.8, with $m_{3/2} = 250$ GeV, but $\tan\beta = 50$ and CMSSM parameters appropriate for the WMAP strip in the focus-point region.

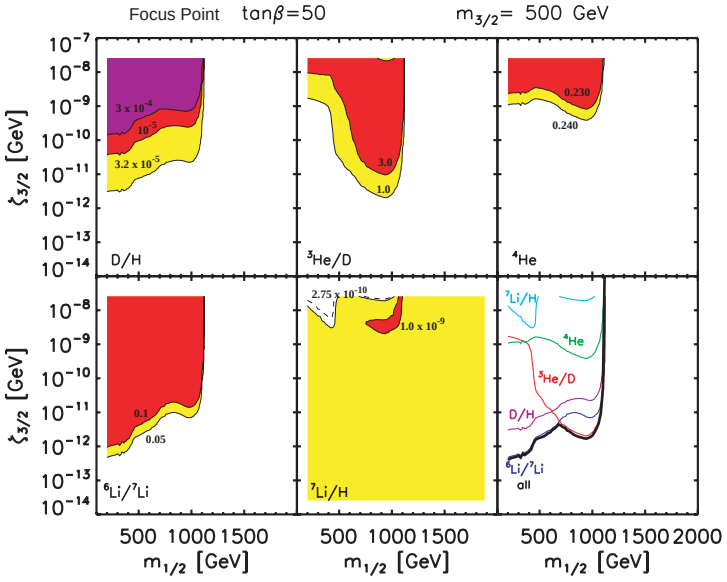

Figure 5.24: As for Fig. 5.8, with $m_{3/2} = 500$ GeV, but $\tan\beta = 50$ and CMSSM parameters appropriate for the WMAP strip in the focus-point region.

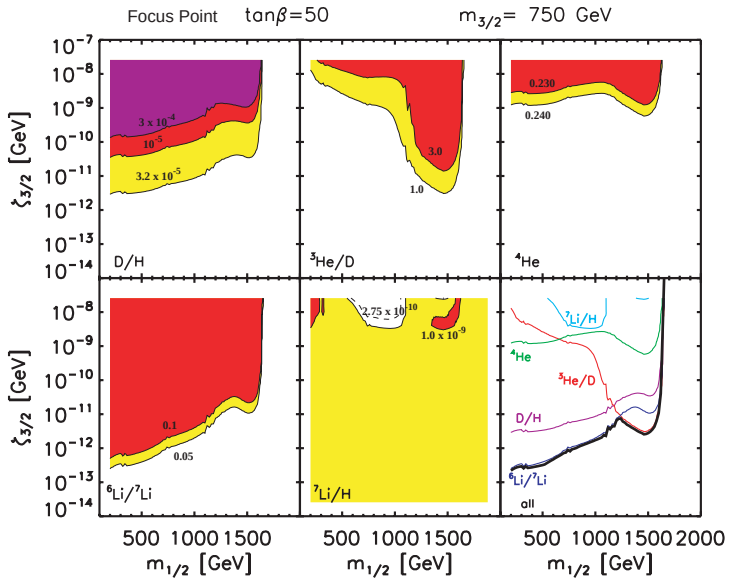

Figure 5.25: As for Fig. 5.8, with $m_{3/2} = 750$ GeV, but $\tan\beta = 50$ and CMSSM parameters appropriate for the WMAP strip in the focus-point region.

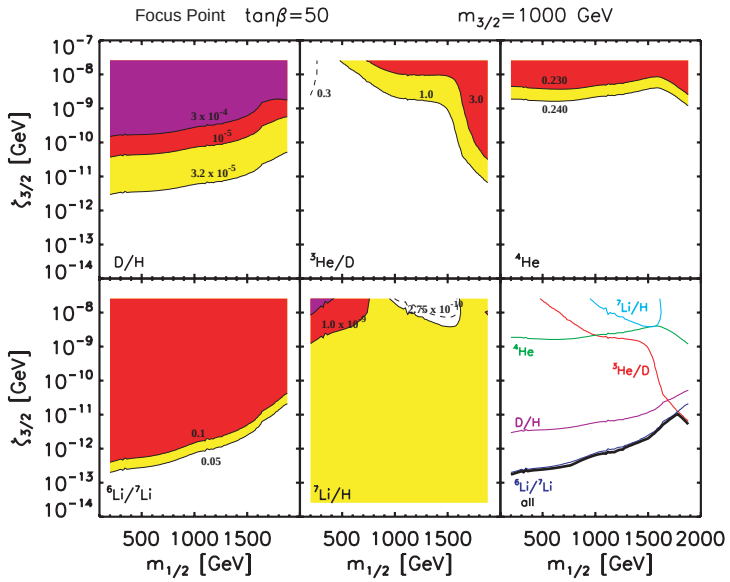

Figure 5.26: As for Fig. 5.8, with $m_{3/2} = 1000$ GeV, but $\tan\beta = 50$ and CMSSM parameters appropriate for the WMAP strip in the focus-point region.

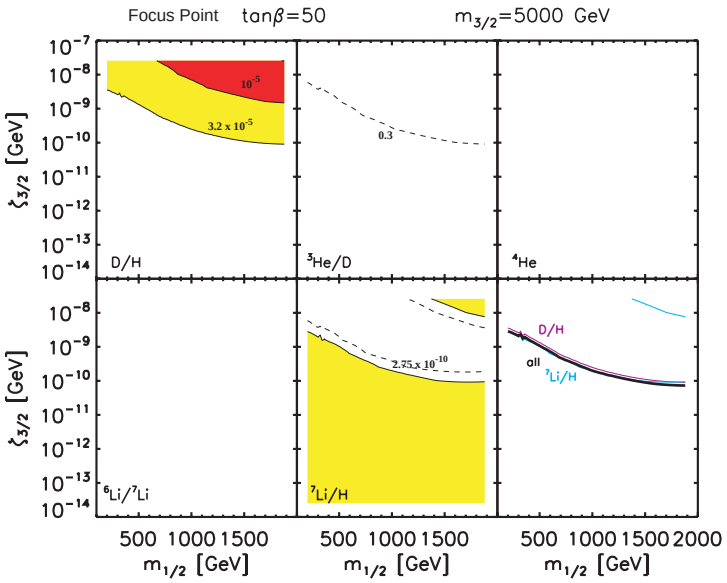

Figure 5.27: As for Fig. 5.8, with $m_{3/2} = 5000$ GeV, but $\tan\beta = 50$ and CMSSM parameters appropriate for the WMAP strip in the focus-point region.

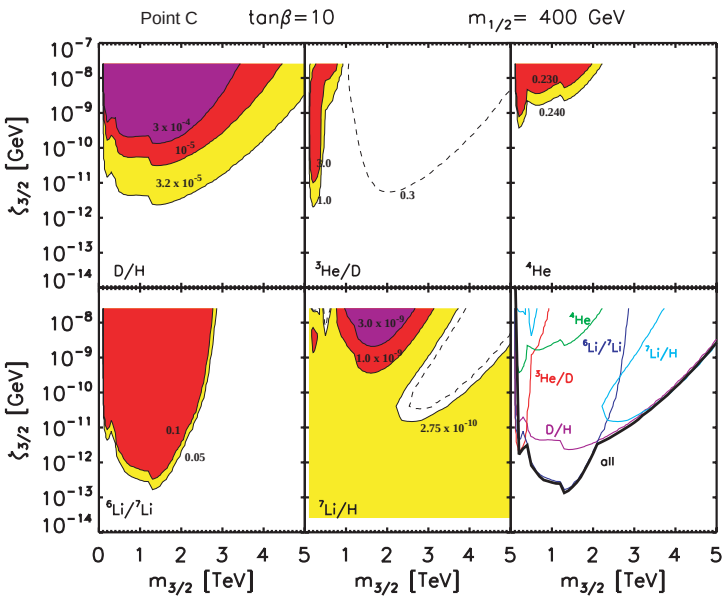

Figure 5.28: The effects of the decays of a gravitino with variable mass $m_{3/2}$ on the different light-element abundances for a specific point (benchmark C) with $m_{1/2} = 400$ GeV on the WMAP coannihilation strip for a CMSSM scenario with $\tan\beta = 10, A_0 = 0$. As in previous figures, the white regions in each panel are those allowed at face value by the light-element abundances reviewed in Chapter 3, and the yellow, red, and magenta regions correspond to progressively larger deviations from the central values of the abundances. We see marginal compatibility between the ^{7}Li constraint (light blue) and the other constraints for $m_{3/2} \gtrsim 3$ TeV.

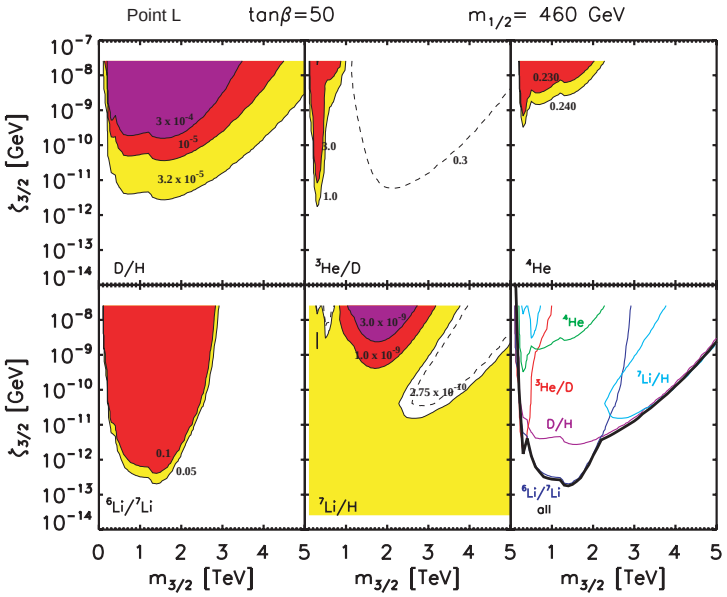

Figure 5.29: As for Fig. 5.28, for CMSSM benchmark point L with $m_{1/2} = 460$ GeV and $\tan\beta = 50$, on the WMAP strip in the coannihilation region.

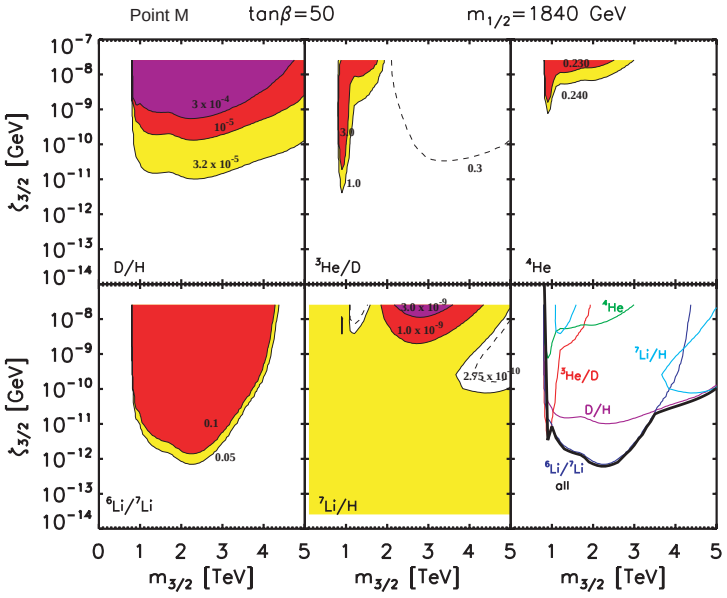

Figure 5.30: As for Fig. 5.28, for CMSSM benchmark point M with $m_{1/2} = 1840$ GeV and $\tan\beta = 50$, on the WMAP strip in the rapid-annihilation funnel region.

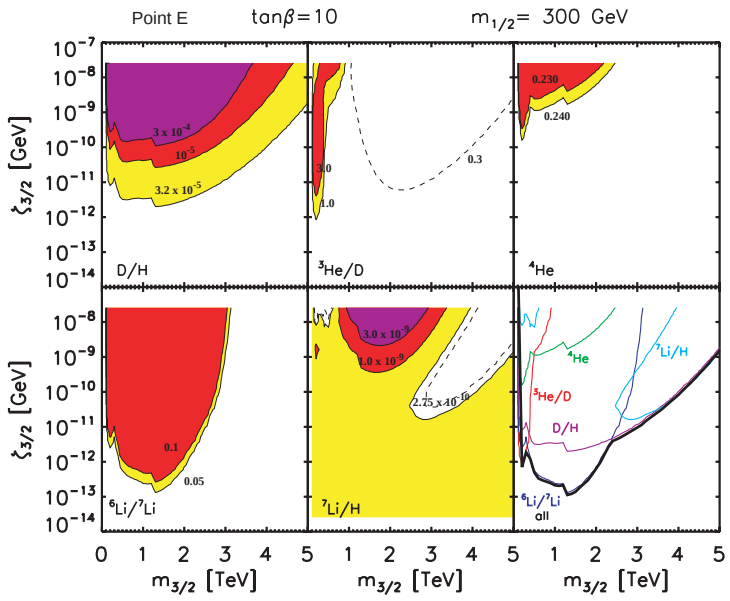

Figure 5.31: As for Fig. 5.28, for CMSSM benchmark point E with $m_{1/2} = 300$ GeV and $\tan\beta = 10$, on the WMAP strip in the focus-point region.

Chapter 6

Nuclear Reaction Uncertainties, Massive Gravitino Decays and the ^{7}Li Problem

Having shown the importance of the non-thermal nuclear reactions in constraining new physics in Chapter 5, we now turn to discuss the effects of the uncertainties in the non-thermal nuclear reaction rates, so that we could evaluate more precisely the constraints on the decays of unstable particles during or after BBN, and the potential to solve the ^{7}Li problem in this scenario.

6.1 Principal nuclear reaction rates

As explained in Chapter 4, the impacts of the non-thermal nuclear reactions on the light-element abundances are introduced through eqs. (4.5) and (4.6). The non-thermal processes we considered are listed in Table 4.1.

The rates $\Gamma_{hb\to\ell}$ in eq. (4.6) depend on both the non-thermal hadron spectra N_h, as well as the cross section $\sigma_{hb\to\ell}$, and so both terms will contribute to the uncertainty budget. However, it turns out that the spectra have significantly smaller errors. As emphasized in Section 3 and Appendix A of [47], the spectra N_h are determined by an equilibrium between the non-thermal hadron sources and their losses. The sources are

the heavy particle decays, whose spectra are well-determined by supersymmetry and Standard Model physics, and have negligibly small uncertainties ($\lesssim 5\%$). Also, the physics for the losses are well understood [47], and errors in the various losses are all $< 10\%$ [60].

We conclude that the errors in N_h should be relatively small, $\lesssim 10\%$, and hence that the uncertainties in the reaction rates should be dominated by the larger errors in the light-element cross sections that we have highlighted in Table 4.1.

The uncertainty in the reaction rate $\Gamma_{hb\to\ell}$, due to cross-section errors $\delta\sigma_{hb\to\ell}$, is

$$\delta\Gamma_{hb\to\ell} = \int N_h(\epsilon)\ v\ \delta\sigma_{hb\to\ell}(\epsilon)\ d\epsilon \tag{6.1}$$

$$\equiv \epsilon_{hb\to\ell}\ \Gamma_{hb\to\ell} \tag{6.2}$$

where $\epsilon_{hb\to\ell} = \delta\Gamma_{hb\to\ell}/\Gamma_{hb\to\ell}$ characterizes the fractional error in the rate. The propagated non-thermal spectra $N_h(\epsilon)$ generally increase to a peak at $\epsilon \sim few$ GeV, i.e., at energies far above thermal energies, the Gamow peak, and any reaction threshold. Non-thermal rates, unlike thermal rates, are sensitive to cross section behaviors over much larger ranges of energies. The cross sections typically grow rapidly above threshold, and then in some cases (fusion processes) drop strongly above $\epsilon \sim few \times 10$ MeV, or in other cases (spallation processes) remain nearly constant or drop slowly at high energies. We should expect the uncertainties in non-thermal rates often to be larger than the typical uncertainties in the thermal rates, which are sensitive to a much narrower range of energies around the Gamow peak, typically $\sim 0.1 - 0.3$ MeV.

We have estimated uncertainties for the non-thermal reactions by comparing nominal cross-section fits with experimental measurements. The fitting functions $\sigma(\epsilon)$ typically provide good or excellent fits to the data. However, the data themselves are often sparse over the large energy ranges of interest. Unfortunately, this paucity of data is particularly acute for the spallation reactions $h^4\mathrm{He} \to (h, {}^2A, {}^3A)+\cdots$, which are among the most important, as we shall see. In each case, we estimate conservatively the typical fractional size $\epsilon = \delta\sigma/\sigma$ of the experimental error bars over the energies where the cross section is substantial (i.e., near maxima for strongly-peaked cross sections, and out to $\sim few$ GeV for flat cross sections). In the following section, we determine which of these reactions have the most important impacts on the light-element abundances, and we report the uncertainties for those in Table 4.1.

For a sufficiently large abundance of gravitinos, the standard BBN predictions are modified, and the resulting light-element abundances need to be compared with observational determinations. In Chapter 5, we used the abundances (or abundance ratios) of D, ^{4}He, ^{7}Li, ^{3}He/D, and ^{6}Li/^{7}Li to determine the allowed regions of parameter space defined by the gravitino mass, $m_{3/2}$, the gaugino mass, $m_{1/2}$, the ratio of Higgs vacuum expectation values, $\tan\beta$, and the gravitino abundance, $\zeta_{3/2}$. We re-calculate the global likelihood function χ^2 in the same representative $(m_{3/2}, \zeta_{3/2})$ planes, now including the uncertainties in the measured abundances as well as the nuclear reaction rates. For our present χ^2 analysis, we restrict our attention to the elements that have definite observational abundances with which we can make a comparison, namely, D/H, ^{4}He and ^{7}Li/H, as we summarized in Chapter 3.

To obtain our χ^2 distribution, we combine the standard BBN uncertainties with the observational errors in quadrature. In the case of ^{7}Li, where the reported errors are uneven, we use the upper error bar on the observation, and the lower error bar on the theory, as we are interested in the region between these two central values. Correspondingly, the likelihood function that we calculate is

$$\chi^2 \equiv \left(\frac{Y_p - 0.256}{0.011}\right)^2 + \left(\frac{\frac{D}{H} - 2.82 \times 10^{-5}}{0.27 \times 10^{-5}}\right)^2 + \left(\frac{\frac{^7\mathrm{Li}}{H} - 1.23 \times 10^{-10}}{0.71 \times 10^{-10}}\right)^2 + \sum_i s_i^2, \quad (6.3)$$

where the s_i are the contributions to the total χ^2 due to the nuisance parameters associated with varying one or more of the rates listed in Table 4.1. Standard BBN has a large total $\chi^2 = 31.7$, primarily due to the discrepancy in ^{7}Li. There is a contribution of $\Delta\chi^2 \sim 30$ from the ^{7}Li abundance, $\Delta\chi^2 \sim 1.2$ from the D/H abundance, and a smaller contribution from ^{4}He, corresponding to a $\sim 5-\sigma$ discrepancy overall [1] .

Our treatments of the hadronic and electromagnetic components of the showers induced by heavy-particle decays follow those in [47]. Also, we follow the calculations of decay branching ratios and particle spectra described in Chapter 5. The only differences here are in the nuclear reaction rates and their uncertainties that were discussed above.

We display in Fig. 6.1 the effects on the abundances of the light elements deuterium, ^{3}He, ^{4}He, ^{6}Li and ^{7}Li of the decays of a generic metastable particle X with lifetime

[1] We find that $\chi^2 = 21.8$ even when the globular cluster value of ^{7}Li/H is used, corresponding to a $4-\sigma$ effect.

$\tau_X \in (1, 10^{10})$ sec. For illustration, we assume the decay spectra calculated in [47] for the choice $(m_{1/2}, m_{3/2}, \tan\beta) = (300\ \text{GeV}, 500\ \text{GeV}, 10)$, in which case the proton branching ratio $B_p \approx 0.2$ and the electromagnetic branching rate is $B_{\rm EM} m_{3/2} = 115$ GeV. In this figure we assume the nominal central values of the nuclear reaction rates discussed in the text, and this figure may be compared directly with Fig. 5.4. The main differences are in the upper left panel, where the region where the deuterium abundance lies within the favored range is now pushed to values of ζ_X that are lower by a factor of about 2 when $\tau_X < 10^6$ sec as compared to Fig. 5.4, and in the lower middle panel, where the region of acceptable ^{7}Li abundance extends to lower ζ_X when $\tau_X \sim 10^3$ sec. Both these effects are due to the inclusion of the reactions $n^4\text{He} \to nn^3\text{He}$ and $p^4\text{He} \to ppt$, and have the effect of pushing the location of a possible 'solution' of the ^{7}Li problem also to lower ζ_X.

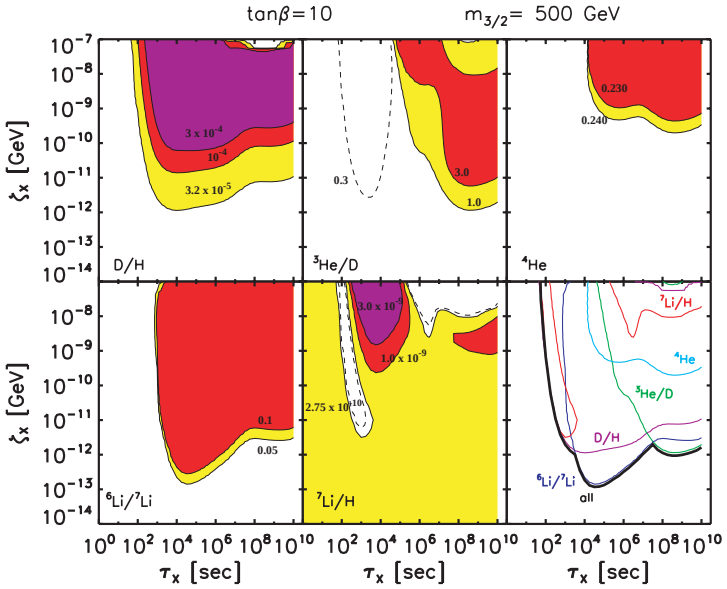

Figure 6.1: The same plot as Fig. 5.4, but with the inclusion of the reactions $n^4\text{He} \to nn^3\text{He}$ and $p^4\text{He} \to ppt$.

We show in Fig. 6.2, one generic $(m_{3/2}, \zeta_{3/2})$ plane, also without the inclusion of uncertainties in the non-thermal rates in Table 4.1. This plot is based on a specific CMSSM point (benchmark C of [125]) with $m_{1/2} = 400$ GeV, $A_0 = 0$, and $\tan\beta = 10$.

The universal scalar mass is set to $m_0 = 90$ GeV to get the correct WMAP density for dark matter. The lightest neutralino mass is about 165 GeV for this point, and for gravitino masses larger than this we have neutralino dark matter with an unstable massive gravitino. This figure may be compared directly with Fig. 5.28. As in Fig. 6.1, the region where the deuterium abundance lies within the favored range is now also pushed to lower $\zeta_{3/2}$ when $m_{3/2} \lesssim 2$ TeV as compared to Fig. 5.28, and the region of acceptable ^{7}Li abundance extends to lower $\zeta_{3/2}$ when $m_{3/2}$ is between 2 - 3 TeV. In the lower right panel, we see marginal compatibility between the ^{7}Li constraint (light blue) and the other constraints for $m_{3/2} \gtrsim 3$ TeV. This region will be the focus of our discussion in the following χ^2 analysis.

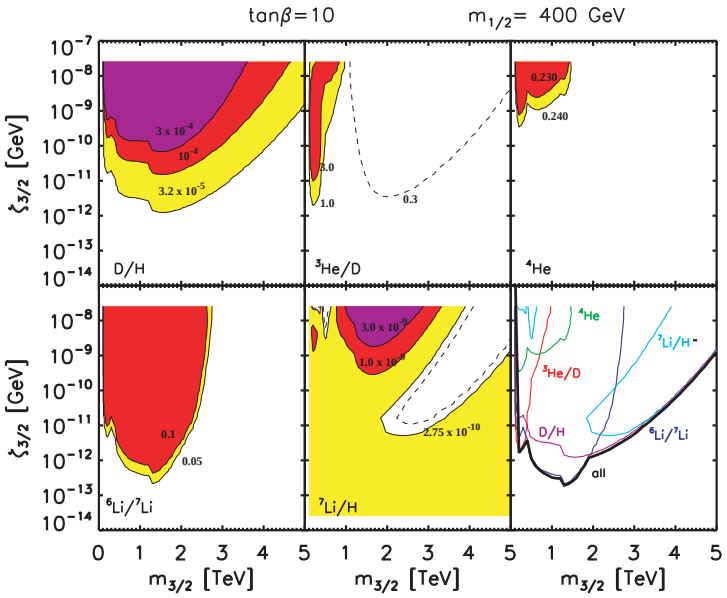

Figure 6.2: The same plot as Fig. 5.28, but with the inclusion of the reactions $n^4\mathrm{He} \to nn^3\mathrm{He}$ and $p^4\mathrm{He} \to ppt$.

6.2 Incorporation of uncertainties

Of the 36 interactions we study, there are just 10 whose uncertainties induce non-negligible uncertainties in the light-element abundances, namely the reactions 2, 3, 4,

6, 7, 21, 22, 23, 31, and 32 in Table 4.1. Their uncertainties are not important for the ^{4}He abundance Y_p, but are potentially important for the deuterium, ^{3}He, ^{6}Li and ^{7}Li abundances.

To explore the effect of reaction uncertainties, we quantify the reaction sensitivity as follows. Using the set of unperturbed non-thermal reaction rates $\{\Gamma_i^0\}$, we find the unperturbed abundances of light elements: examples of these results appear in Figures 6.1 and 6.2. For a given light element ℓ, we call the unperturbed abundance y_ℓ^0. Then, for any single reaction j, we consider changes in the rate by a factor $1+\epsilon$: $\Gamma_j' = (1+\epsilon)\Gamma_j^0$, leaving all other non-thermal (and thermal) rates unchanged. We evaluate the new resulting light-element abundances for a wide range of values for ϵ including both positive and negative values and write the new, perturbed ℓ abundance as $y_\ell'|_{\mathrm{rxn}j} \equiv y_\ell^0 + \delta y_\ell|_{\mathrm{rxn}j}$. In this way, we were able to identify the 10 reactions listed above as potentially playing an important role in altering the light-element abundances. Our final results are based on a Gaussian distribution of rates with widths give by the values of ϵ chosen according to the uncertainty estimates in Table 4.1.

We display in Figs. 6.3, 6.4, 6.5, and 6.7 the effects of the uncertainties in these reaction rates on the abundances of each of the key elements among deuterium, ^{3}He, ^{6}Li and ^{7}Li, each in a $(m_{3/2}, \zeta_{3/2})$ plane. We concentrate here on benchmark point C, as the effect of perturbing the interactions is qualitatively similar for the other benchmark points we consider below.

For example, in Fig. 6.3 we show the effect of the $p^4\mathrm{He} \to np^3\mathrm{He}$ (reaction 2) in Table 4.1 on the abundances of D/H (left) and ^{3}He/H (right). In this case the effect on ^{6}Li and ^{7}Li is negligible. We plot contours showing

$$\left.\frac{\delta y_\ell}{y_\ell}\right|_{\mathrm{rxn}j} \equiv \frac{y_\ell'|_{\mathrm{rxn}j} - y_\ell^0}{y_\ell^0} \ , \tag{6.4}$$

the relative change in the light-element abundance when rate j is perturbed by a factor $(1+\epsilon)$. For reaction 2, we estimate a 20% uncertainty in the rate and, as one can see, the effect on D/H is always less than 4% and occurs at very high gravitino abundances. The effect on ^{3}He is also relatively small, but extends over a larger portion of the parameter space. The effect of reaction 31($p^4\mathrm{He} \to ppt$) is qualitatively similar to the one shown in Fig. 6.3.

For reactions 3 and 4, corresponding to $p^4\mathrm{He} \to ddp$ and $p^4\mathrm{He} \to dnpp$ respectively,

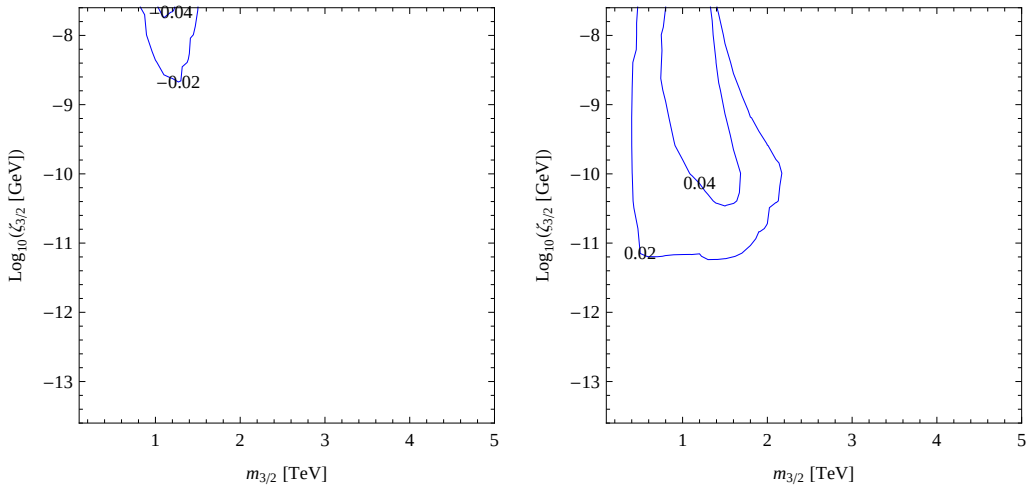

Figure 6.3: The effects in the $(m_{3/2}, \zeta_{3/2})$ plane of the 20% uncertainty in the rate for the reaction 2 ($p^4\mathrm{He} \to np^3\mathrm{He}$) on the abundances of deuterium (left) and ^{3}He (right). Contours show the relative changes in the light-element abundances.

we estimate an uncertainty of 40%. However, even with the larger uncertainty, the relative change in D/H for both rates is still less than 4%, extends down to lower $\zeta_{3/2} \sim 10^{-10}$ GeV, and the ^{3}He abundance variation is even smaller. Accordingly, we do not show these examples.

In Fig. 6.4, the effects of reaction 6 corresponding to $t^4\mathrm{He} \to {}^6\mathrm{Li}n$ are displayed (the effects of reaction 7 corresponding to $^3\mathrm{He}^4\mathrm{He} \to {}^6\mathrm{Li}p$ are similar but weaker by a factor of 2): we estimate 20% uncertainties for these reactions. We see that in this case, while there is some effect on the abundance of ^{7}Li, the dominant effect of varying this rate is on ^{6}Li, where changes can be as large as 12% for almost all the values of $\zeta_{3/2}$ shown when $m_{3/2} \sim 1$ TeV. We find similar results for points E and L, whilst for point M (see below) similarly large changes in ^{6}Li are centered around $m_{3/2} \sim 2$ TeV. The effects on deuterium and ^{3}He are negligible for reactions 6 and 7.

The effects of reaction 21 ($n^4\mathrm{He} \to npt$), for which we also estimate an uncertainty of 20%, on all four light elements are shown in Fig. 6.5. The possible effect on ^{7}Li is largest, amounting possibly to a reduction in the ^{7}Li abundance by up to 6% in a

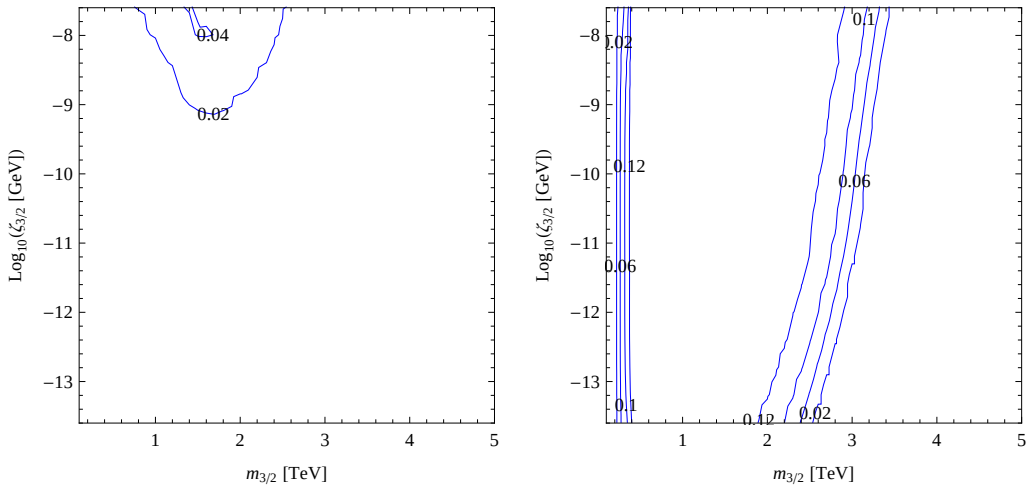

Figure 6.4: Similar to Fig. 6.3, for the reaction 6 ($t^4\mathrm{He} \to {}^6\mathrm{Li}n$), in this case showing the effect on ^{7}Li/H (left) and ^{6}Li/H (right).

diagonal region extending from $m_{3/2} \gtrsim 3$ TeV. (For benchmark point M, the reduction in the ^{7}Li abundance occurs at $m_{3/2} \gtrsim 4$ TeV.) Reaction 32 ($n^4\mathrm{He} \to nn^3\mathrm{He}$) shows effects somewhat similar (though in general a bit weaker) to those seen in Fig. 6.5, and is not shown separately.

We note that, although the relative shift in the abundance is small for a 20% variation in the rate, the ^{7}Li abundance in this region (the diagonal strip where the abundance is decreased by 4-6% in Fig. 6.5) is already significantly reduced when using the (unperturbed) non-thermal rates. In this region, several rates (principally reactions 21, 23, and 32) combine to lower the ^{7}Li abundance when the gravitino abundance is sufficiently large. However, subsequent variations in the rates do not make any further significant changes in the abundances. To help better understand this point quantitatively, we show in Fig. 6.6, the ^{7}Li abundance as a function of ϵ for rate 21 (other rates have $\epsilon_{i\neq 21} = 0$) in the upper panel and as a function of $\epsilon_{21} = \epsilon_{23} = \epsilon_{32}$ in the lower panel. As one can see, particularly in the latter case, when $\epsilon_{21,23,32} = -1$ and these rates are shut off entirely, the abundance of ^{7}Li is 4.2 $\times 10^{-10}$ (the 20% decrease in ^{7}Li is due to the remaining non-thermal reactions). Furthermore, coherent variations in these rates

of 20-40% make relatively small changes in the abundances as reflected in Fig. 6.5, and the effects of random variations in the rates would clearly be smaller still.

Whilst reaction 23 ($n^4\mathrm{He} \to dnnp$) shows smaller variations in ^{7}Li, the uncertainty (which we estimate at 40%) is larger. The effect on D/H is also pronounced, as seen in Fig. 6.7. The effect of reaction 22 ($n^4\mathrm{He} \to ddn$) is qualitatively similar but weaker.

We conclude this section by summarizing the main results of our propagation of non-thermal reaction rate errors into uncertainties in light-element abundances. We find that the ^{4}He abundance is essentially unaffected by reaction rate errors. For ^{7}Li, we find that no one reaction dominates the non-thermal perturbations, which in turn means that errors in any given rate only have a rather small (typically $\lesssim 10\%$) effect on the ^{7}Li/H abundance. Non-thermal deuterium production is also not entirely controlled by a single reaction, though the $n^4\mathrm{He} \to dnnp$ reaction clearly stands out as the most important, and the resulting errors in D/H can go as high as $\gtrsim 20\%$.

These results have important implications for our χ^2 analysis, which, as we will see, is dominated by ^{7}Li/H and D/H. Since the ^{7}Li/H nuclear uncertainties are small compared to the observational errors in the ^{7}Li/H abundance, the latter dominates the lithium contribution to χ^2. Conversely, the D/H non-thermal rate errors are significant in comparison to the observational errors, and thus will have an important effect on the χ^2 and ultimately on the lithium problem. From this we infer that the reactions which most critically need improved nuclear data are those which are important for deuterium production.

6.3 χ^2 analyses of benchmark CMSSM scenarios

To proceed with the χ^2 analysis, we use Eq. (6.3) to calculate χ^2 for each point sampled in the $(m_{3/2}, \zeta_{3/2})$ plane. The reaction rates are treated as nuisance parameters and therefore, for each evaluation of χ^2, each non-thermal rate is chosen from a Gaussian distribution about the mean rate with the uncertainty specified in the previous section. At each point and for each reaction considered, the difference between the rate chosen and its mean value, relative to the quoted uncertainty in the rate, determines the corresponding s_i in Eq. (6.3).

From the results of the analysis in the previous section, it is clear that it will be

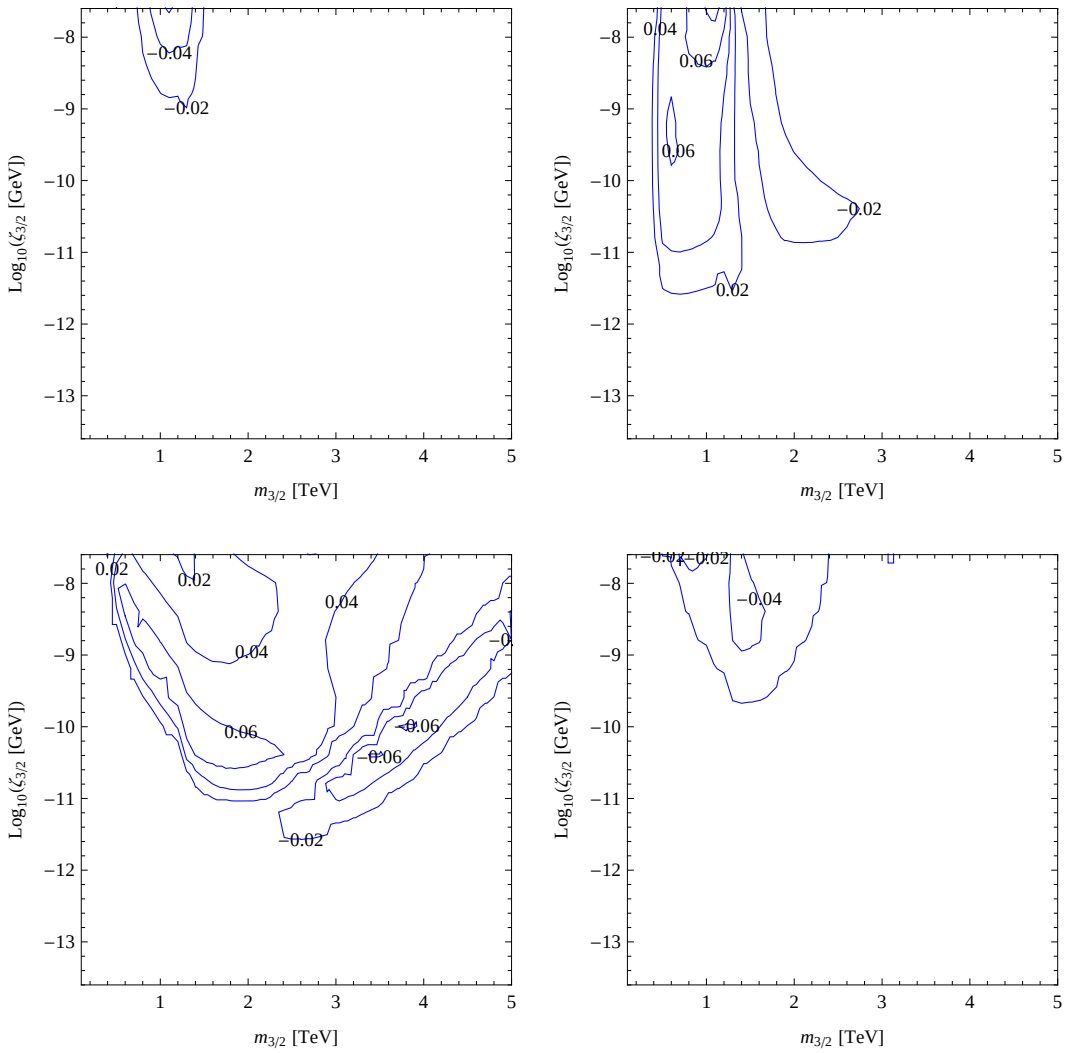

Figure 6.5: Similar to Fig. 6.3, for the reaction 21 ($n^4\mathrm{He} \to npt$), showing the effects on all four light elements deuterium (upper left), ^{3}He (upper right), ^{7}Li (lower left) and ^{6}Li (lower right).

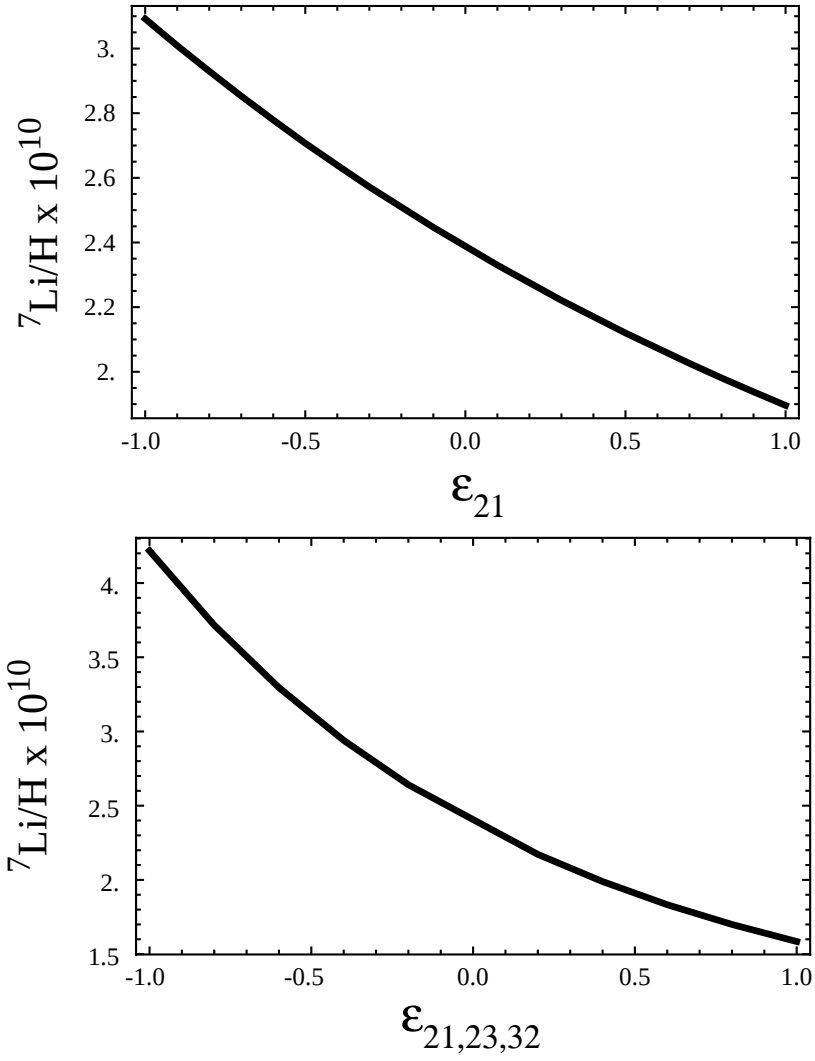

Figure 6.6: The ^{7}Li abundance as a function of ϵ: $\epsilon = -1$ is equivalent to turning off the rate, and $\epsilon = 0$ leaves the rate unperturbed. In the upper panel we show the effect of reaction 21 alone, and in the lower panel we show the combined effect of reactions 21, 23, and 32.

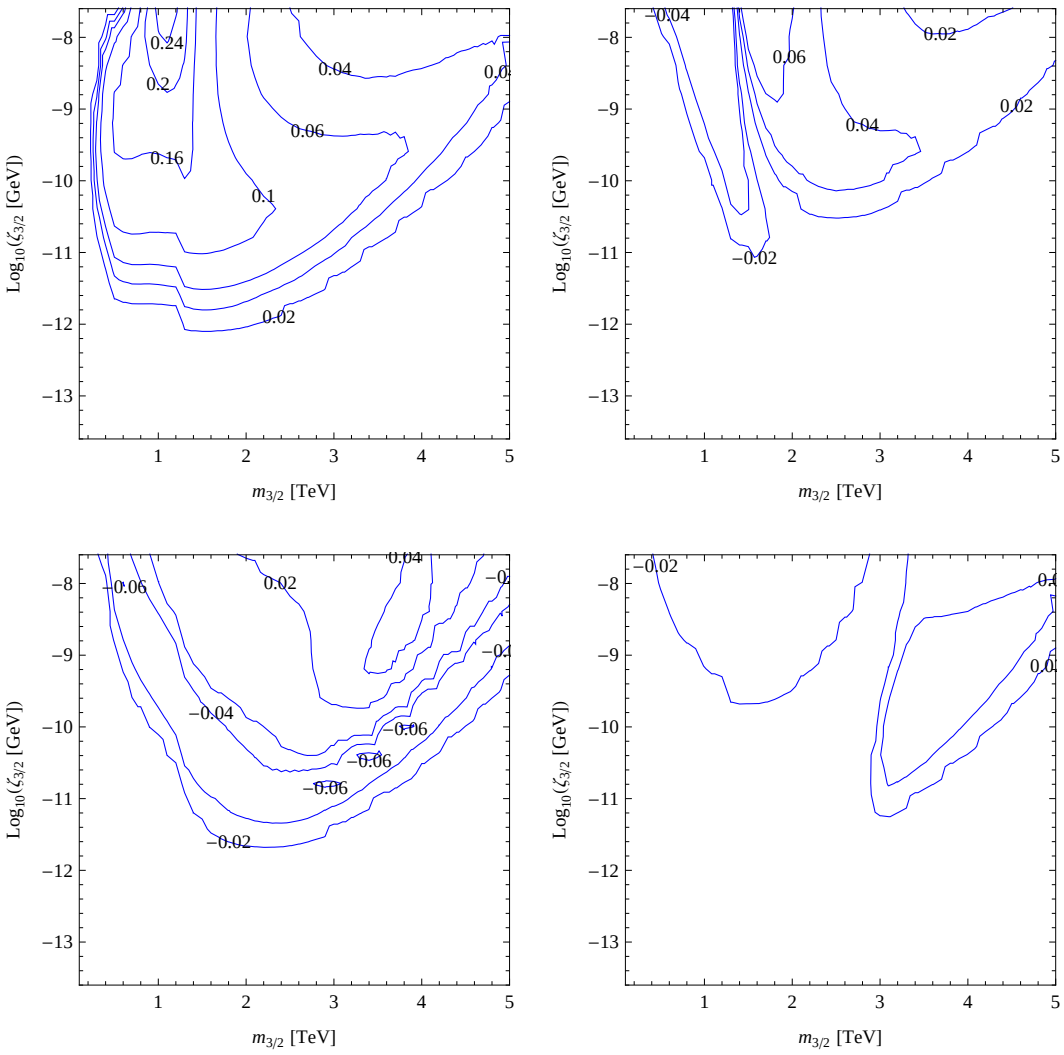

Figure 6.7: Similar to Fig. 6.5, for the reaction 23 ($n^4\mathrm{He} \to dnnp$).

sufficient to focus on the effects of reactions 21, 23, and 32. In principle, one could include all reactions in the χ^2 analysis as nuisance parameters. However, the inclusion of many more reactions would have only a marginal effect on lowering the χ^2 contribution from the abundances, while at the same time increasing χ^2 through s_i^2. Since each rate typically increases χ^2 by roughly one unit, one would need to gain at least one unit from the effect of the uncertainty in the rate on the element abundances. Including the uncertainties of reactions beyond 21, 23, and 32 with finite sample sizes will typically lead to a larger value of χ^2.

In Section 5.2.3, we discussed the application of the BBN constraints to four benchmark CMSSM scenarios with specific values of the soft supersymmetry-breaking parameters $m_{1/2}, m_0$ and A_0, $\tan\beta$, and the Higgs mixing parameter μ, labelled C, E, L and M [125]. In each case, $A_0 = 0$ and $\mu > 0$ was chosen. The parameters corresponding to point C were given earlier. For points E, L, and M they are $(m_{1/2}, m_0, \tan\beta) =$ (300 GeV, 1615 GeV, 10), (460 GeV, 310 GeV, 50), and (1840 GeV, 1400 GeV, 50) respectively. Variants of these CMSSM scenarios with a massive gravitino are characterized by the gravitino mass $m_{3/2}$ and its abundance $\zeta_{3/2}$. The $(m_{3/2}, \zeta_{3/2})$ planes for benchmark scenarios C, E, L and M are shown in Fig. 6.8, displaying χ^2 contours for the light-element abundances calculated incorporating the nuclear reaction rate uncertainties discussed above.

In the limit of large $m_{3/2}$ and/or small $\zeta_{3/2}$, the value of the χ^2 function approaches ~ 31.7, the same value as in standard BBN. This large value of χ^2 is due primarily to the ^{7}Li problem. We see that in each of the CMSSM scenarios in Fig. 6.8 there is a 'trough' of much lower χ^2 with a minimum at ~ 5.5, shown in each panel by a cross. We display contours of $\chi^2 = 6$ and 9.2, corresponding to the 95 and 99% CLs for fitting to two parameters. Also shown are the higher χ^2 contours of 32 (corresponding to the BBN value) and 50. We see that the $(m_{3/2}, \zeta_{3/2})$ planes are very similar for benchmarks C, E and L. The plane for benchmark M is somewhat different, and the minimum value of χ^2 is slightly higher. In Table 6.1, we show the various abundances and χ^2 contributions for each of the three light elements for the standard BBN result and our best-fit point for each of the four benchmark points.

It is interesting to note the tension between D and ^{7}Li. At each of the best fit points, there is a considerable reduction in ^{7}Li, approaching the observational value.

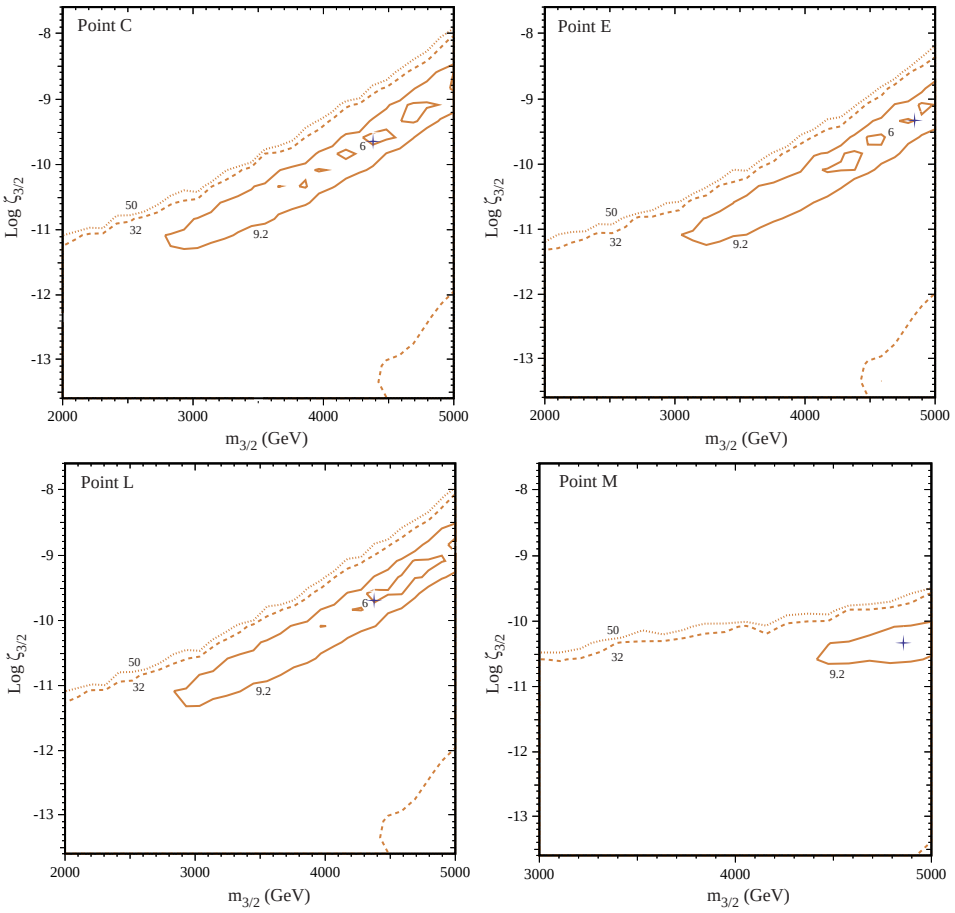

Figure 6.8: Contours of the χ^2 function in the $(m_{3/2}, \zeta_{3/2})$ planes for the benchmark CMSSM scenarios C (upper left), E (upper right), L (lower left) and M (lower right), incorporating the uncertainties in the nuclear rates discussed in the text.

Table 6.1: Results for the best-fit points for CMSSM benchmarks C, E, L and M. The second set of results for C and M correspond to the globular cluster value for primordial ^{7}Li/H. The third and fourth entries for point C correspond to the higher adopted uncertainty for D/H in field stars and to the globular cluster ^{7}Li abundances, respectively.

	$m_{3/2}$[GeV]	$\mathrm{Log}_{10}(\zeta_{3/2}/[\mathrm{GeV}])$	Y_p	D/H ($\times 10^{-5}$)	^{7}Li/H ($\times 10^{-10}$)	$\sum s_i^2$	χ^2
BBN	——	——	0.2487	2.52	5.12	——	31.7
C	4380	−9.69	0.2487	3.15	2.53	0.26	5.5
E	4850	−9.27	0.2487	3.20	2.42	0.29	5.5
L	4380	−9.69	0.2487	3.21	2.37	0.26	5.4
M	4860	−10.29	0.2487	3.23	2.51	1.06	7.0
C	4680	−9.39	0.2487	3.06	2.85	0.08	2.0
M	4850	−10.47	0.2487	3.11	2.97	0.09	2.7
C	3900	−10.05	0.2487	3.56	1.81	0.02	2.8
C	4660	−9.27	0.2487	3.20	2.45	0.16	1.1

The minimum value $\chi^2 \sim 5.5$ certainly amounts to a 'mitigation' of the ^{7}Li problem, but not a 'solution', in the sense that since we are fitting two parameters ($m_{3/2}$ and $\zeta_{3/2}$) and using 3 measurements, we have effectively only one degree of freedom and χ^2/d.o.f. ~ 5.5. However, this improvement in ^{7}Li comes at the expense of D/H, which at this point begins to make a more significant contribution to the total χ^2. On the other hand, the ^{4}He abundance Y_p does not contribute significantly to the likelihood at any point in the parameter space. At the minimum, the deuterium abundance contributes $\Delta\chi^2 \sim 1.5$, whereas the ^{7}Li abundance contributes $\Delta\chi^2 \sim 3.4$. Thus the previous 4- or 5-σ ^{7}Li problem is reduced to a $\lesssim$ 2-σ problem. If this mitigation is to lead to a complete solution, one or more of the nuclear reaction rates and/or measured light-element abundances should lie outside its quoted uncertainty.

As an example, in Fig. 6.9 we show the analogous results for the χ^2 likelihood, assuming the globular cluster value for ^{7}Li/H (see Section 3.2). Results for this case for benchmark points C and M are also summarized in Table 6.1. We now see the appearance of contours for $\chi^2 = 4.6$ and 2.3 corresponding to 90 and 68 % CLs respectively. The best-fit χ^2 values drop considerably in this case, with values of 2.0 and 2.7 for points C and M respectively. Thus a massive ($\gtrsim$ 4 TeV) gravitino can provide a potential solution of the lithium problem if globular cluster data is assumed to represent

the primordial ^{7}Li abundance.

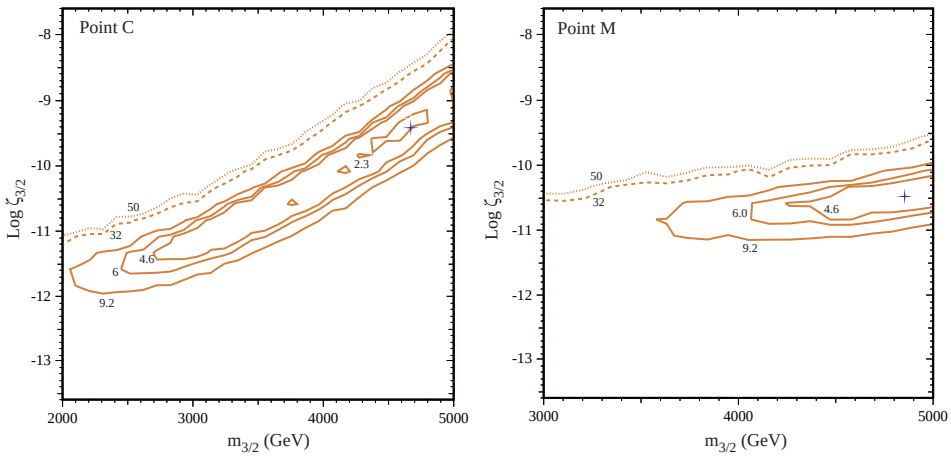

Figure 6.9: As in Fig. 6.8, contours of the χ^2 function in the $(m_{3/2}, \zeta_{3/2})$ planes for the benchmark CMSSM scenario C (left) and M (right), assuming the globular cluster value of ^{7}Li/H.

As discussed in Section 3.1, one may also consider the effect of increasing the size of the uncertainty in the mean D/H abundance. Using an observed abundance of $(2.82 \pm 0.53) \times 10^{-5}$, we obtain the χ^2 contours seen in the left panel of Fig. 6.10, corresponding to point C. In this case, we can obtain solutions with $\chi^2 = 2.8$ and a best-fit point with a ^{7}Li/H abundance of 1.81 $\times 10^{-10}$ coming at the expense of a higher D/H abundance of 3.56×10^{-5}. When the globular cluster value of ^{7}Li/H is used together with the higher D/H uncertainty, we can even find a best-fit solution with $\chi^2 = 1.1$: D/H $= 3.20 \times 10^{-5}$ and ^{7}Li/H $= 2.45 \times 10^{-10}$, as seen in the right panel of Fig. 6.10.

The fact that this prospective solution to the ^{7}Li problem exists for several choices of supersymmetric scenarios, with parameters that are relatively stable, suggests that it is a general feature of supersymmetric models. For this potential solution to be confirmed, one or more of the following should happen.

1. There might be some refinement in measurements of the cosmological ^{7}Li abundance leading to a shift in the central value and/or a change in the assigned uncertainty. As we have shown in Fig. 6.9, for example, if the globular-cluster

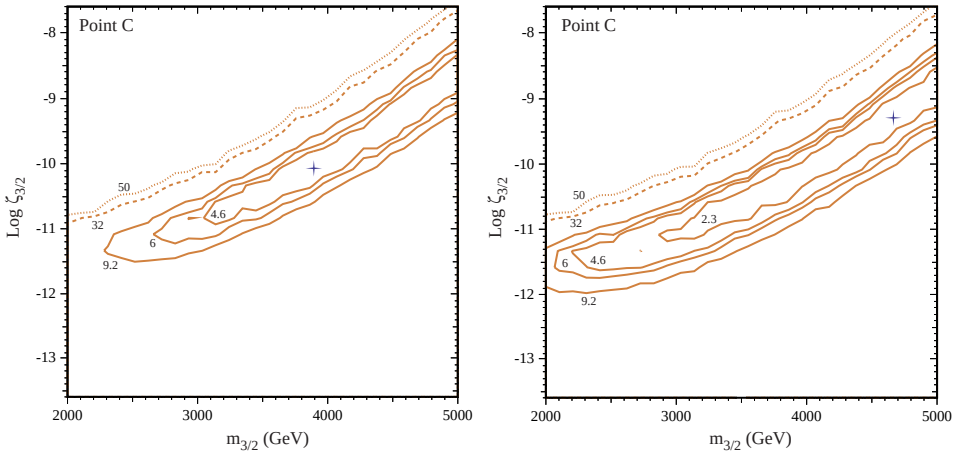

Figure 6.10: As in Fig. 6.8, contours of the χ^2 function in the $(m_{3/2}, \zeta_{3/2})$ planes for the benchmark CMSSM scenario C assuming (left) a greater uncertainty in the observed D/H abundance and (right) also assuming the globular cluster value of ^{7}Li/H.

estimate of the ^{7}Li abundance is adopted (which would correspond to $\chi^2 \sim 21.8$ in standard BBN), the decays of massive gravitinos could reduce χ^2 to ~ 2.0.

2. Alternatively, it is possible that the rates for one or more nuclear reactions might lie outside the ranges favored by the current measurements and their assigned uncertainties. As we have pointed out, the measurements of some of these non-thermal rates are sparse over the energy ranges of interest, and improved coverage is certainly possible and desirable. The highest-priority reactions for new cross-section measurements are $n^4\mathrm{He} \to npt$, $n^4\mathrm{He} \to dnnp$ and $n^4\mathrm{He} \to nn^3\mathrm{He}$, which we have shown to be the most relevant for this analysis.

3. Finally, we should mention the possibility of some unidentified error in our analysis: we have given reasons why we think the errors in the light-element cross sections dominate in the uncertainties of the non-thermal nuclear reaction rates, but we could be wrong.

Chapter 7

Enhanced Cosmological ^{6}Li Abundance as a Potential Signature of Residual Dark Matter Annihilations

The previous two chapters demonstrated that late-decaying massive gravitinos might resolve the ^{7}Li problem within the CMSSM framework. In this chapter we show that the ^{6}Li problem might, independently and in parallel, have at least a partial supersymmetric solution, via the late annihilations of neutralino LSPs.

We find negligible effects on the abundances of deuterium, ^{3}He, ^{4}He and ^{7}Li predicted by homogeneous BBN, but potentially a large enhancement in the predicted abundance of ^{6}Li, as suggested in [38]. The physics of this effect is the following. It is well understood that the famous $A = 5$ gap in the spectrum of stable nuclei impedes the production of heavier nuclei in BBN. The dominant mechanism for making ^{6}Li in annihilating-particle scenarios is initiated by p and n spallation of ^{4}He. This yields many $A = 3$ nuclei with only a tiny reduction in ^{4}He abundance. The tritium and ^{3}He nuclei are produced with large, non-thermal energies, and subsequently slow down due to ionization losses, but have some probability of inducing $t(\alpha, n)^6$Li or ^{3}He$(\alpha, p)^6$Li reactions first. In this way, an amount of ^{6}Li may be produced that is large relative

to the standard homogeneous BBN abundance, without making large amounts of extra deuterium and $A = 3$ or reducing the ^{4}He abundance, and leaving the ^{7}Li abundance unaffected.

7.1 Residual late-time neutralino annihilations

Assuming that the lightest neutralino χ is the LSP, and that R-parity is conserved, the relic neutralino density is essentially fixed at a freeze-out temperature $T_f \sim m_\chi/20$. At lower temperatures, the local density of neutralinos, n_χ, decreases as the universe expands (presumably) adiabatically, and subsequent annihilations have very little effect on the dark matter density, but may have important effects on the light-element abundances [27, 37, 38, 61].

The rate per volume of annihilation *events* is

$$q_{\rm ann} = \frac{1}{2} n_\chi^2 \langle \sigma v \rangle_{\rm ann}, \tag{7.1}$$

and so the annihilation event rate *per* χ is

$$\Gamma_{\rm ann} = \frac{q_{\rm ann}}{n_\chi} = \frac{1}{2} \langle \sigma v \rangle_{\rm ann} n_\chi = \frac{1}{2} \langle \sigma v \rangle_{\rm ann} Y_\chi n_{\rm b}, \tag{7.2}$$

and thus the annihilation event rate *per baryon* is

$$\frac{q_{\rm ann}}{n_{\rm b}} = \Gamma_{\rm ann} Y_\chi = \frac{1}{2} \langle \sigma v \rangle_{\rm ann} Y_\chi^2 n_{\rm b}, \tag{7.3}$$

where the χ abundance is

$$Y_\chi = \frac{n_\chi}{n_{\rm b}} = \frac{m_{\rm b}}{m_\chi} \frac{\Omega_\chi}{\Omega_{\rm b}}. \tag{7.4}$$

At the temperatures of interest here, $T_{\rm BBN} \lesssim 1$ MeV $\ll m_\chi$, the annihilation rate coefficient $\langle \sigma v \rangle_{\rm ann}$ is very well approximated as a constant, the value of which depends on the specific underlying supersymmetry model. In eq. (7.1), we are interested in only the s-wave part of the cross-section whereas a combination of s- and (mainly) p-wave cross-sections is constrained by the requirement of reproducing the present dark matter density within errors.

The annihilations inject non-thermal Standard Model particles, including both electromagnetic as well as hadronic species. For electromagnetic products we need only

track the total energy injected per annihilation. For non-thermal hadrons (nucleons) $h = n, p$, we calculate the spectrum $Q_h^{\rm ann}(\epsilon)$ of annihilation products, normalized such that $\int Q_h^{\rm ann}(\epsilon)\ d\epsilon = B_h$, the expected number of h created per annihilation. Then the injection/source rate of h due to annihilations, per unit volume, per unit time, and per unit kinetic energy ϵ, is

$$\frac{d\mathcal{N}_{h,\rm inj}^{\rm ann}}{dV\,dt\,d\epsilon} = q_{\rm ann} Q_h^{\rm ann}(\epsilon)\ . \tag{7.5}$$

These particles then lose energy as they propagate in the cosmic plasma. The propagated spectrum of non-thermal particles must be calculated, and this produces the non-thermal reactions on ambient thermal light nuclides that perturb BBN.

The effect of non-thermal particle injection in BBN has been well-studied in the case of decays of some unstable particle X. Much of the physics carries over here, once one makes the appropriate substitution of abundances $n_X \to n_\chi$ and of annihilation rate for decay rate: $\Gamma_X = \tau_X^{-1} \longrightarrow \Gamma_{\rm ann}$, as we explained in Chapter 4.

7.2 Order-of-magnitude calculation

Before turning to our numerical results, we first present an order-of-magnitude calculation that illustrates the basic physics in play, and also serves as a check on our numerical results. The total number of annihilation events per baryon occurring after a given time t_i is the time integral of eq. (7.3)

$$\mathcal{N}_{\rm ann} = \int_{t_i} \Gamma_{\rm ann}\ Y_\chi\ dt \sim Y_\chi^2 \langle\sigma v\rangle_{\rm ann} n_{\rm b}(t_i)\ t_i \tag{7.6}$$

$$= 5\times 10^{-9}\ \text{events/baryon}\ \left(\frac{\langle\sigma v\rangle_{\rm ann}}{10^{-26}\ \text{cm}^3\,\text{s}^{-1}}\right)\ \left(\frac{300\text{GeV}}{m_\chi}\right)^2\ . \tag{7.7}$$

Our fiducial values correspond to $t_i \sim 100$ sec and $T_i \sim 100$ keV, since this marks the epoch when the ^{4}He abundance becomes large.

Given this number of annihilations per baryon, we now need the branching for ^{6}Li production per annihilation. As discussed earlier, non-thermal particles from annihilations or decays produce ^{6}Li as a secondary by-product of ^{4}He spallation:

$$\begin{aligned} p_{\rm nonthermal} {}^4{\rm He} &\to {}^3{\rm H}_{\rm nonthermal} + \cdots \\ & \quad {}^3{\rm H}_{\rm nonthermal} + {}^4{\rm He} \to {}^6{\rm Li} + n\,, \end{aligned} \tag{7.8}$$

and similarly with nonthermal ^{3}He; nonthermal D also contributes but is subdominant. As discussed for the late-decay case in [47], each late annihilation produces a mass-3 abundance increment $\Delta Y(^3A)$ which is given in the thin target limit by

$$\Delta Y(^3A) \sim \mathcal{N}_{\rm ann} B_N \frac{\sigma(N\alpha \to {}^3A + \cdots)}{\sigma(N\alpha \to \text{inelastic})}, \tag{7.9}$$

where $B_N \sim 0.4$ is the number of nucleons per annihilation. Typically this increases the mass-3 abundance by an amount $\Delta Y(^3A) \sim 10^{-9} \ll Y_{\rm BBN}(^3A) \sim 10^{-5}$, i.e., much smaller than the standard primordial abundance, and thus we do not expect substantial perturbations to mass-3 nuclides, or to D, which has similar cross sections, or to ^{4}He.

The energetic $A = 3$ particles are slowed in the cosmic plasma by ionization and related losses, with a range $R_3 = \int (dE/dX)^{-1} dE$, where dE/dX is the loss rate per thickness $dX = \rho_{\rm b} dx$ in [g/cm^2]. Hence the stopping length is $R_3/\rho_{\rm b}$. The fraction of mass-3 nuclides which produce ^{6}Li before stopping is this stopping length divided by the mean free path for ^{6}Li production, namely:

$$f(^3A \to {}^6\text{Li}) \sim n_\alpha \sigma(^3A\alpha \to {}^6\text{Li}) \frac{R_3}{\rho_{\rm b}} \sim Y_\alpha \frac{\sigma(^3A\alpha \to {}^6\text{Li}) R_3}{m_{\rm b}} \sim 7 \times 10^{-4} \quad . \tag{7.10}$$

Collecting these results, the residual late-time annihilation contribution to the ^{6}Li abundance per baryon is

$$\begin{aligned} \Delta Y(^6\text{Li}) &= \Delta Y(^3A)\ f(^3A \to {}^6\text{Li}) \\ &\sim B_N Y_\chi^2 \langle\sigma v\rangle_{\rm ann} Y_\alpha \frac{\sigma(N\alpha \to {}^3A + \cdots)}{\sigma(N\alpha \to \text{inelastic})}\ \frac{\sigma(^3A\alpha \to {}^6\text{Li}) R_3}{m_{\rm b}}\ n_{\rm b}(t_i)\ t_i \\ &= 7 \times 10^{-13} \left(\frac{\langle\sigma v\rangle_{\rm ann}}{10^{-26}\ \text{cm}^3\,\text{s}^{-1}} \right) \left(\frac{300\ \text{GeV}}{m_\chi} \right)^2 \quad . \end{aligned} \tag{7.11}$$

The numerical results given above are evaluated for $t_i = 100$ sec, and we also take $R_3 = 1\,\text{g/cm}^2$ and $\sigma(^3A\alpha \to {}^6\text{Li}) = 30$ mb. This formula gives the scaling $\Delta Y(^6\text{Li}) \propto B_N \langle\sigma v\rangle_{\rm ann} (\Omega_\chi/m_\chi)^2$ which we verify with our full numerical results, and the normalization agrees to within a factor ~ 2. This agreement lends confidence in our code and our understanding of the physics.

7.3 Numerical results

We turn now to our full numerical results. In order to establish the context for our subsequent analysis of the possible annihilation effects along the strips in CMSSM parameter

space that are compatible with WMAP and other constraints on the present-day dark matter density, we first discuss the full CMSSM $(m_{1/2}, m_0)$ planes shown in Fig. 7.1. The light blue lines are contours of the ^{6}Li abundance, and the relic density is WMAP-compatible [3] along the dark blue strips, assuming that the lightest neutralino χ is the LSP and is stable, as in R-conserving models. There would be no consistent electroweak vacuum in the pink shaded region at small $m_{1/2}$ and large m_0, the lighter $\tilde{\tau}$ would be the LSP in the brown shaded region, and the green shaded region is excluded by $b \to s\gamma$ decay [1] [129]. Regions to the left of the red dash-dotted (black dashed) (purple) line are excluded by searches for the Higgs boson at LEP (charginos) (LHC searches for sparticles) [130]. In the paler pink region the supersymmetric contribution remedies the discrepancy between the experimental measurement of $g_\mu - 2$ and theoretical calculation within the Standard Model [131, 132] using low-energy e^+e^- data, with 1- (2-)σ [132] consistency being indicated by the dashed (solid) black lines.

We see in the left panel of Fig. 7.1 showing the $(m_{1/2}, m_0)$ plane for $\tan\beta = 10$ that most of the lower (coannihilation) WMAP strip has $^6\mathrm{Li/H} < 10^{-13}$, whereas the upper (focus-point) strip may have ^{6}Li/H as large as 10^{-12}. There is a region where ^{6}Li/H seems able to exceed 10^{-11}, but this is well inside the region between the WMAP strips, where the relic χ is overdense according to conventional Big-Bang cosmology. In the right panel of Fig. 7.1 for $\tan\beta = 55$, we see that $^6\mathrm{Li/H} \sim 10^{-13}$ along the coannihilation strip and in the funnel region at large $m_{1/2}$ and m_0 where the relic density is brought into the WMAP range by rapid annihilations through direct-channel H/A resonances, though somewhat larger values of ^{6}Li/H are possible at small $m_{1/2}$. Along the focus-point strip, we see that values of $^6\mathrm{Li/H} \sim 10^{-12}$ are also possible at small $m_{1/2}$, falling to $\sim 10^{-13}$ at large $m_{1/2}$. The range $^6\mathrm{Li/H} \sim 10^{-11}$ is never attained for $\tan\beta = 55$, even in the overdense region of the $(m_{1/2}, m_0)$ plane.

We now focus on the WMAP strips in Fig. 7.1. The left panel of Fig. 7.2 displays the figure-of-merit combination $\langle\sigma v\rangle_{\mathrm{ann}}(\Omega_\chi h^2/m_\chi)^2$ as a function of $m_{1/2}$ along the WMAP strips in the CMSSM for $\tan\beta = 10$ and 55. We see that $\langle\sigma v\rangle_{\mathrm{ann}}(\Omega_\chi h^2/m_\chi)^2$ along the coannihilation strip for $\tan\beta = 10$ is much smaller than along the other strips. This can be understood from the fact that along this strip several coannihilation processes

[1] According to conventional Big-Bang cosmology and in the absence of R violation, the LSP χ would be overdense in the regions between the WMAP strips. It would be underdense in the regions between these strips and the pink and brown shaded regions.

involving sleptons contribute to reducing the relic χ density into the WMAP range, and that their relative contributions become more important as $m_{1/2}$ increases. In addition, along this strip the s-wave cross-section relevant during BBN is significantly smaller than the p-wave cross-section that dominates during freeze-out. These coannihilation processes are less important along the corresponding strip for $\tan\beta = 55$, and unimportant in the funnel region and along the focus-point strips, where the s-wave cross-section becomes comparable to the total cross section. Hence, along these strips $\langle\sigma v\rangle_{\rm ann}$ must be larger, in order to bring the relic density down into the WMAP range unaided. Note that the precipitous drop in the cross section at low $m_{1/2}$ for the $\tan\beta = 10$ focus point strip occurs as we pass below the W^+W^- threshold.

The $\chi\chi$ annihilations feed many different particle species into the cosmological background, initially with non-thermal spectra that we model using `PYTHIA` [59]. The only species that survive long enough to interact significantly with background nuclei are protons and neutrons (and their antiparticles) and photons. The former are far more important for the nuclear reactions of interest here, so we focus on their numbers and spectra. The right panel of Fig. 7.2 displays the numbers of protons (solid or dotted lines) and neutrons (dashed or dash-dotted lines) produced per annihilation event, again along the WMAP strips for $\tan\beta = 10, 55$ discussed previously. We see that in general the numbers of protons and neutrons increase significantly as $m_{1/2}$ increases, with some bumps as new annihilation thresholds are crossed.

Fig. 3 of [133] displays the most important branching fractions for final states in $\chi\chi$ annihilations as functions of $m_{1/2}$ along the WMAP strips for $\tan\beta = 10$ and 55, which include the final states $\tau^+\tau^-$, $b\bar{b}$, W^+W^-, $t\bar{t}$, hZ and ZZ. Of these, the $\tau^+\tau^-$ final state clearly yields no baryons, while the numbers of baryons yielded by the final states W^+W^-, hZ and ZZ are all independent of the annihilation centre-of-mass energy $2m_\chi$. Only the $b\bar{b}$ and $t\bar{t}$ final states yield numbers of baryons that increase with the annihilation centre-of-mass energy.

Fig. 7.3 displays the spectra of protons (upper panel) and neutrons (lower panel) for the W^+W^-, hZ and ZZ final states for $m_\chi = 250$ GeV, and for the $b\bar{b}$ final state for $m_\chi = 100, 250$ GeV, all calculated using `PYTHIA`. We display the number of protons or neutrons per unit of the parameter $x \equiv \sqrt{E_i^2 - m_i^2}/m_\chi$, where $i = p, n$. The proton and neutron spectra are almost identical. They differ in the small x region primarily

because of the difference of m_p and m_n. We also see that the W^+W^-, hZ and ZZ final states yield rather similar spectra, with the spectrum from the hZ final state rising slightly higher. The spectra of baryons from $b\bar{b}$ final states rise from being lower at $m_\chi = 100$ GeV to being higher at $m_\chi = 250$ GeV.

Together with Fig. 3 of [133], Fig. 7.3 enables us to understand the salient features of the baryon production rates shown in the right panel of Fig. 7.2. The large branching fraction for $\tau^+\tau^-$ suppresses baryon injection along the coannihilation strip for $\tan\beta = 10$, particularly for small $m_{1/2}$ but less so for large $m_{1/2}$ where the W^+W^- branching fraction grows.

Following their injection into the primordial plasma, some of the nucleons cause spallation of ^{4}He, yielding $A = 3$ nuclei as discussed above. These are produced with large, non-thermal energies and subsequently thermalize, but may previously induce $t(\alpha, n)^6$Li or ^{3}He$(\alpha, p)^6$Li reactions. Fig. 7.4 displays the enhancement of the cosmological ^{6}Li abundance that we find along the WMAP strips discussed above. The homogeneous BBN value $\sim 10^{-14}$ is attained at large $m_{1/2}$ along the WMAP coannihilation strip for $\tan\beta = 10$, but much larger values are possible along the other WMAP strips [2] , where we find ^{6}Li/H $\sim 10^{-13}$ at large $m_{1/2}$ to 10^{-12} at small $m_{1/2}$. We have found that the enhancement of ^{6}Li scales very closely with the combination $B_N\langle\sigma v\rangle_{\rm ann}/m_\chi^2$, as was to be expected.

We recall that the enhancement of ^{6}Li/H that would be required for consistency with eq. (3.5) is by a factor ~ 1000, rather than the factor of up to ~ 100 that we find here. However, as we have noted there remains a question as to whether or not the plateau ratio of 0.05 should be attributed to ^{6}Li. The abundance of ^{6}Li we find here is potentially observable and would in fact be seen as a plateau extending to low metallicities. Optimistically, we could envision ^{6}Li observations playing a role in discerning between supersymmetric models. In any case, we regard the enhancement we find as already an interesting contribution to the analysis of the ^{6}Li problem.

[2] The region of enhanced ^{6}Li along the WMAP coannihilation strip for $\tan\beta = 10$ with $m_{1/2} <$ 400 GeV is now excluded by the unsuccessful LHC searches for supersymmetry [130, 134].

7.4 Exploration of non-universal Higgs models

It is quite possible that some modifications of the CMSSM might yield even greater enhancements of the ^{6}Li abundance. To be successful in this respect, it is apparent from eq. (7.11) that such a model would require a relatively large annihilation cross section $\langle\sigma v\rangle_{\rm ann}$ combined with a small value of m_χ, as in the focus-point region of the CMSSM. There, the relatively large value of $\langle\sigma v\rangle_{\rm ann}$ is made possible by the admixture of a Higgsino component in the χ, and along this strip the low value of m_χ is consistent with the LHC and other constraints [134].

In an initial probe of other possibilities for a large enhancement of the ^{6}Li abundance, we have explored the NUHM1 model, in which the soft supersymmetry-breaking contributions to the Higgs masses have a common value that differs from m_0. It is known that in this model the Higgsino component in the LSP χ may be enhanced at values of $m_{1/2}$ and m_0 away from the focus-point region, thanks to a level-crossing transition at particular values of $\mu/m_{1/2}$ [70]. In the CMSSM, the value of μ is generally fixed by applying the conditions for a consistent electroweak vacuum. However, in the NUHM1 the value of $\mu/m_{1/2}$ can be adjusted by varying the degree of non-universality in the soft supersymmetry-breaking Higgs masses, enabling a WMAP-compatible relic density to be found in models with values of $(m_{1/2}, m_0)$ different from those allowed in the CMSSM.

We have explored the conditions under which such transition regions in the NUHM1 may yield an enhancement of ^{6}Li/H similar to, or (possibly) greater than the value $\sim 10^{-12}$ attainable in the CMSSM in the focus-point region. To this end, we have studied over a dozen NUHM1 parameter planes. In no case did we find enhancements of ^{6}Li/H significantly larger than in the CMSSM (and this is also the case in some planes we explored in the NUHM2, in which both Higgs soft supersymmetry-breaking masses are treated as free, non-universal parameters).

Fig. 7.5 shows results in a couple of selected NUHM1 parameter planes. The left panel shows an $(m_{1/2}, m_0)$ plane for $\tan\beta = 10, A_0 = 0$ and fixed $\mu = 250$ GeV. In this case, there is a near-vertical WMAP-compatible strip in a transition region at $m_{1/2} \sim 400$ GeV. This transition strip is compatible with the LEP Higgs constraint, and the upper part of the strip above $m_0 \sim 700$ GeV is compatible with the constraints

imposed by LHC searches for sparticles. We see that the ^{6}Li/H ratio is remarkably constant at $\sim 5 \times 10^{-13}$ along this strip. It would be possible to increase ^{6}Li/H to $\sim 10^{-12}$ by choosing μ somewhat smaller, in which case the WMAP-compatible strip would be at smaller $m_{1/2}$. In that case, the LHC would enforce a stronger lower limit on m_0, closer to the CMSSM focus-point strip. On the other hand, larger values of μ yield small values of the ^{6}Li abundance, and we find no increase in the ^{6}Li abundance for larger $\tan\beta$.

The right panel of Fig. 7.5 displays a (μ, m_0) plane in the NUHM1 for $\tan\beta = 20, A_0 = 0$ and fixed $m_{1/2} = 500$ GeV, at the lower end of the range allowed by the LHC and other data for $m_0 < 1000$ GeV. In this case, there are near-vertical WMAP-compatible strips in transition region at $|\mu| \sim 300$ GeV, where ^{6}Li/H approaches 10^{-12}. There is also a WMAP-compatible strip near $\mu \sim 1000$ GeV that parallels the region without a consistent electroweak vacuum (here caused by $m_A^2 < 0$), where ^{6}Li/H is again somewhat below 10^{-12}. Connecting these two regions is a coannihilation segment at $m_0 \sim 100 - 200$ GeV where the ^{6}Li abundance is relatively small. We have explored several other NUHM1 (μ, m_0) planes, finding that increasing $m_{1/2}$ decreases the attainable value of ^{6}Li/H. We have also explored several other projections of the NUHM1 and NUHM2, including $(m_A, m_{1/2})$, (m_A, m_0), (μ, m_A) and (m_1, m_2) planes, without finding values of ^{6}Li/H above 10^{-12}.

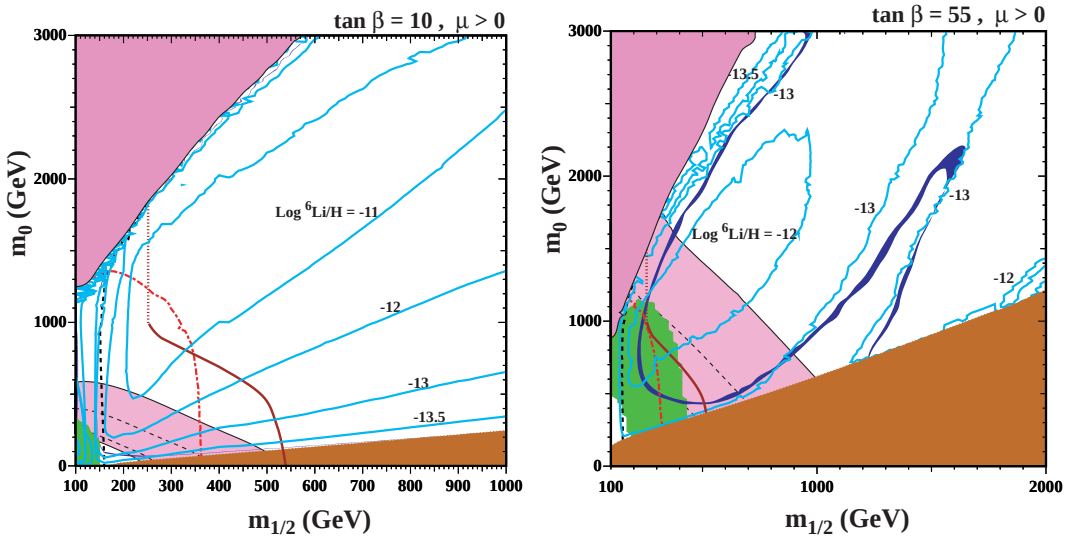

Figure 7.1: Left: The CMSSM $(m_{1/2}, m_0)$ plane for $A_0 = 0$ and $\tan\beta = 10$, and Right: the corresponding plane for $\tan\beta = 55$, both with $\mu > 0$, displaying contours of the ^{6}Li abundance including the effects of late-time $\chi\chi$ annihilations. Contours of the ^{6}Li abundance are coloured light blue, and the WMAP-compatible [3] strips of parameter space are shaded dark blue. The brown shaded region at large $m_{1/2}$ and small m_0 is excluded because the LSP would be charged, and in the pink shaded region at small $m_{1/2}$ and large m_0 there would be no consistent electroweak vacuum. Also shown are the exclusion by LEP searches for the Higgs boson (red dash-dotted line) and charginos (black dashed line), and by LHC searches for sparticles (purple solid and dotted line) [130]. The green shaded region is excluded by $b \to s\gamma$ [129], and the paler pink region is favoured by $g_\mu - 2$ at the 1- (2-)σ level [132], as indicated by the dashed (solid) black lines.

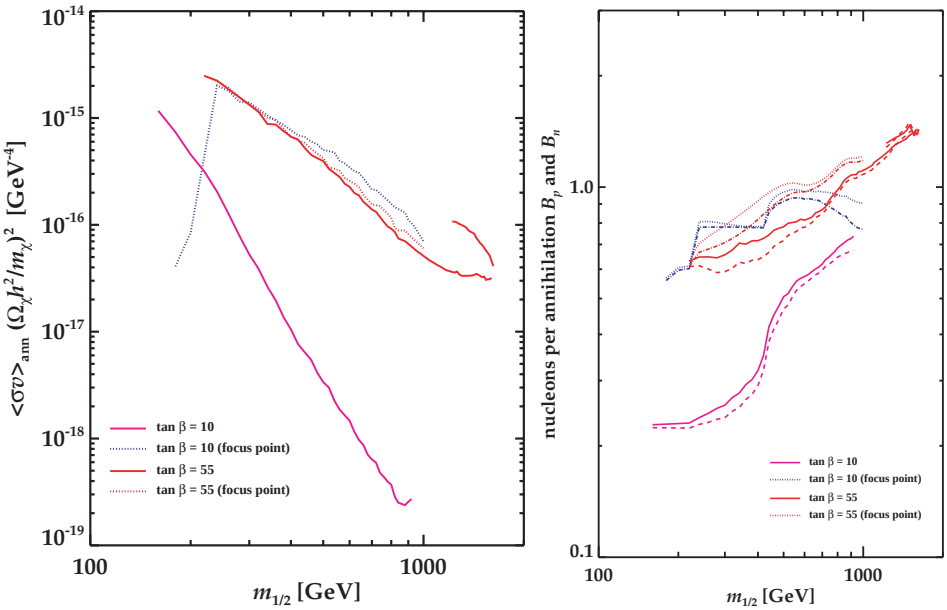

Figure 7.2: Left: The figure of merit for the late-time annihilation rate, namely the velocity-averaged $\chi\chi$ annihilation cross section divided by the square of the neutralino mass, $\langle\sigma v\rangle_{\rm ann}(\Omega_\chi h^2/m_\chi)^2$, along the WMAP strips in the coannihilation, focus-point and funnel regions for $\tan\beta = 10, 55$, $A_0 = 0$ and $\mu > 0$, as functions of $m_{1/2}$. We see that the figure of merit along the $\tan\beta = 10$ coannihilation strip is much smaller than along the other strips, and that all decrease rapidly as $m_{1/2}$ increases. Right: The numbers $B_{p,n}$ of protons (solid or dotted lines) and neutrons (dashed or dash-dotted lines) produced per $\chi\chi$ annihilation event, as calculated using `PYTHIA`, along the WMAP strips in the coannihilation, focus-point and funnel regions for $\tan\beta = 10, 55$, $A_0 = 0$ and $\mu > 0$, as functions of $m_{1/2}$. We see that in general the numbers increase significantly as $m_{1/2}$ increases.

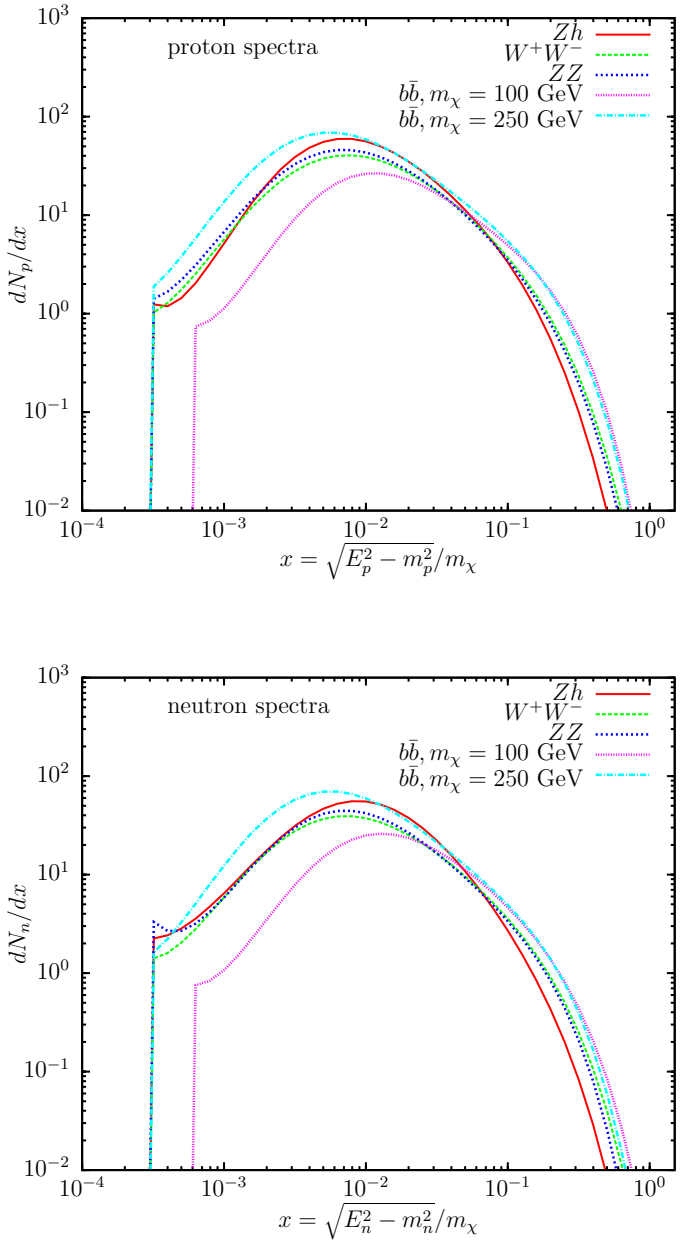

Figure 7.3: The spectra of protons (upper panel) and neutrons (lower panel) injected by $\chi\chi$ annihilations into the Zh, W^+W^-, ZZ and $b\bar{b}$ (for m_χ=100 and 250 GeV) final states, as calculated using `PYTHIA`.

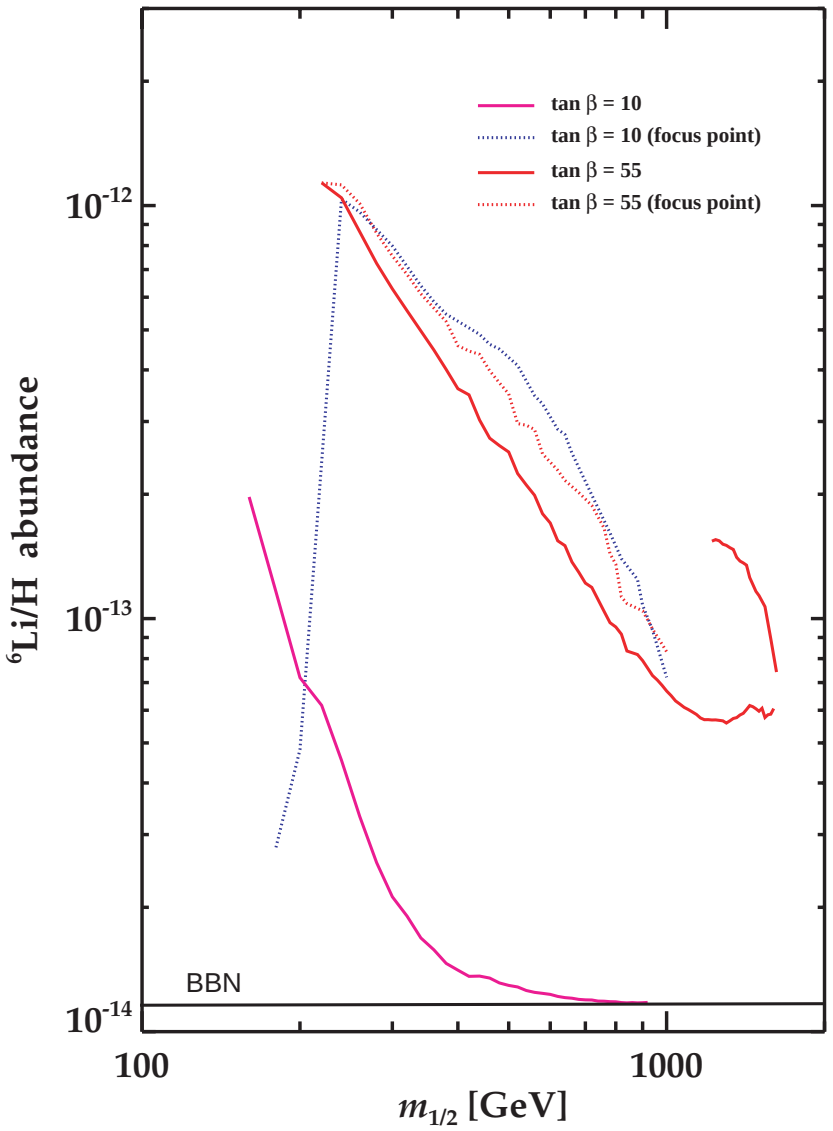

Figure 7.4: The enhancement of the cosmological ^{6}Li abundance as a function of $m_{1/2}$ along the WMAP strips discussed in the text. The standard homogeneous BBN value $\sim 10^{-14}$ is attained at large $m_{1/2}$ along the WMAP coannihilation strip for $\tan\beta = 10$.

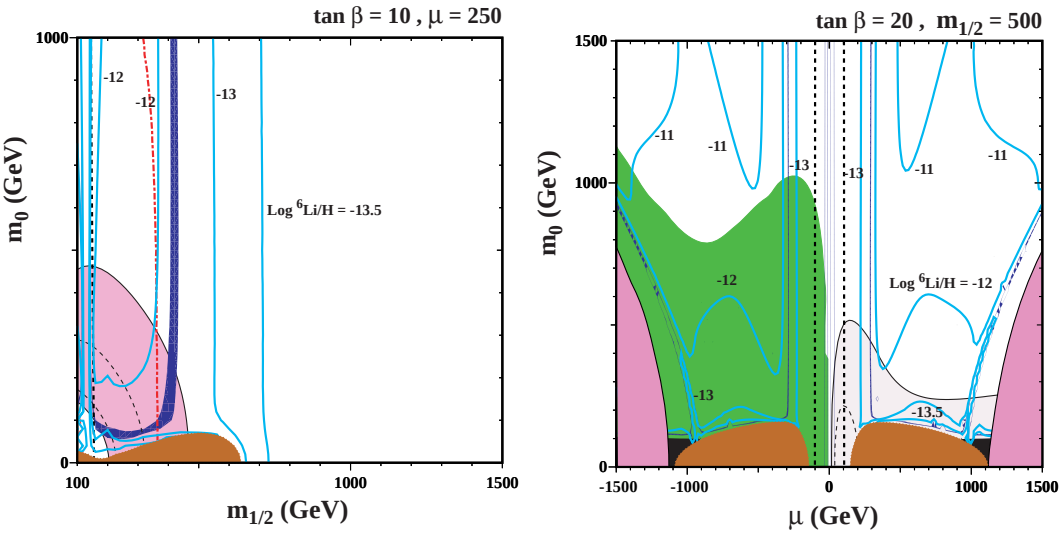

Figure 7.5: Left: The NUHM1 $(m_{1/2}, m_0)$ plane for $\mu = 250$ GeV, $A_0 = 0$ and $\tan\beta = 10$, and Right: the NUHM1 (μ, m_0) plane for $m_{1/2} = 500$ GeV, $A_0 = 0$ and $\tan\beta = 20$, displaying contours of the ^{6}Li abundance including the effects of late-time $\chi\chi$ annihilations. Contours of the ^{6}Li abundance are coloured light blue, and the WMAP-compatible strips of parameter space are shaded dark blue. The other shaded regions and lines have the same meanings as in Fig. 7.1.

Chapter 8

Summary and Conclusions

We have studied the cosmological constraints on unstable gravitinos in R-conserving CMSSM scenarios with a neutralino LSP arising from their effects on the light-element abundances. The first step in this study was the calculation of two-body gravitino decay modes and some important three-body decay modes. The next step was the simulation of the electromagnetic and hadronic products of these decays using `PYTHIA`. We have then used our new suite of codes to simulate the interactions of these decay products with the cosmological plasma, including both energy losses and interactions with the nuclei of light elements that affect their abundances. Generally, we find that details of the decay spectra are less important than the overall fractions of baryons produced in the gravitino decays. These fractions are model-dependent, and vary considerably with the gravitino mass and the CMSSM parameters. In addition to the baryon fractions, the constraints on the gravitino abundance inferred from the observed light-element abundances depend sensitively on the gravitino lifetime, and are generally weaker in scenarios with a shorter-lived gravitino.

For $m_{3/2} < 3$ TeV, none of the CMSSM scenarios we study solves the cosmological ^{7}Li problem. Accordingly, one must either reject these CMSSM scenarios, or re-evaluate the observational data on ^{7}Li, or postulate some other mechanism for bringing the ^{7}Li abundance into line with standard BBN predictions, or find some way to modify these predictions. Setting the ^{7}Li problem aside, we find that the strongest constraints are usually those imposed by the ^{6}Li/^{7}Li ratio, with weaker limits coming from the D/H, ^{3}He/D and ^{4}He constraints. We have evaluated these constraints along WMAP strips in

the $(m_{1/2}, m_0)$ plane where the relic neutralino density falls within the expected range for cold dark matter, for $m_{3/2} = 250, 500, 750, 1000$ and 5000 GeV, $A_0 = 0$ and two representative choices $\tan\beta = 10, 50$. There are two strips for each choice of $\tan\beta$: one in the coannihilation and funnel region, and one in the focus-point region.

We find that the upper limits on $\zeta_{3/2} = m_{3/2} n_{3/2}/n_\gamma$ are quite similar along these WMAP strips, that they weaken as $m_{1/2}$ increases for fixed $m_{3/2}$ (particularly for $\tan\beta = 50$), that they strengthen by about an order of magnitude as $m_{3/2}$ increases from 250 GeV towards 1000 GeV, and that the constraints are significantly weaker for $m_{3/2} = 5000$ GeV. The constraints also weaken considerably as the neutralino mass approaches $m_{3/2}$ from below, as the phase space for gravitino decay disappears. For larger values of $m_{1/2}$, the neutralino is no longer the LSP, and the WMAP strips are inapplicable.

Extending these studies to larger $m_{3/2}$, we find that the D/H and ^{7}Li/H constraints may become marginally compatible for $m_{3/2} \gtrsim 3$ TeV and a very narrow range of gravitino abundance that increases with $m_{3/2}$. In this region, both thermal and non-thermal neutrons destroy ^{7}Be via the $^7\mathrm{Be}(n,p)^7\mathrm{Li}$ reaction, which is followed by ^{7}Li destroyed via the $^7\mathrm{Li}(p,\alpha)^4\mathrm{He}$ reaction for a finely-tuned range of lifetimes around $\tau_X \sim 10^3$ sec. We find that the competing upward perturbations to D/H and ^{3}He/D drive these species away from their observed levels in the regimes where the ^{7}Li problem is solved. This highlights the continued importance of the nuclear reaction data, particularly at energies beyond the $\lesssim 1$ MeV range important for standard, thermal BBN reactions.

We have analyzed the possible effects of the uncertainties of the 36 different non-thermal nuclear reactions included in our code, and identified three as the most important, namely $n^4\mathrm{He} \to npt$, $n^4\mathrm{He} \to dnnp$ and $n^4\mathrm{He} \to nn^3\mathrm{He}$.

As an example of the possible applications of our uncertainty analysis, we have considered the late decays of massive gravitinos in various benchmark supersymmetric scenarios, and we have made a likelihood analysis of the possibility that the ^{7}Li problem might be mitigated or even marginally solved in some ranges of $m_{3/2}$ and $\zeta_{3/2}$, incorporating uncertainties in the nuclear reaction rates.

We confirm that there are indeed regions of the $(m_{3/2}, \zeta_{3/2})$ parameter planes in these scenarios where the global χ^2 function is reduced from its value ~ 31.7 in conventional BBN (~ 21.8 if the globular-cluster value for the ^{7}Li abundance is adopted) to $\chi^2 \sim 5.5$.

This provides a very significant alleviation of the ^{7}Li problem, reducing it from a 4- or 5-σ problem to a $\lesssim$ 2-σ issue. The fact that our best-fit points lie within the $\chi^2 = 6$ contours in Fig. 6.8 implies that they have a goodness-of-fit slightly exceeding 5%, which is marginal for considering massive gravitino decay as a 'solution' to the cosmological ^{7}Li problem.

Turning to the possible ^{6}Li problem, we have demonstrated that in both the CMSSM and the NUHM1 it is possible that late neutralino LSP annihilations may enhance significantly the cosmological ^{6}Li abundance, without affecting significantly the BBN abundances of the other light element deuterium, ^{3}He, ^{4}He and ^{7}Li. This enhancement may be up to two orders of magnitude, yielding ^{6}Li/H $\sim 10^{-12}$ compared to the BBN value $\sim 10^{-14}$.

As we have shown, this enhancement occurs typically when the neutralino LSP is relatively light and has a large annihilation cross section, as occurs when the LSP contains a strong Higgsino admixture. This phenomenon appears, in particular, in the focus-point region of the CMSSM and in transition regions of the NUHM1.

While interesting for the debates on the astrophysical lithium abundances, this enhancement falls short of resolving by itself the cosmological ^{6}Li problem. Further work could include a more exhaustive study of other supersymmetric models, to see whether they could reconcile a larger enhancement with the available theoretical, phenomenological, experimental and cosmological constraints. It is clearly desirable to pin down more definitively the magnitude of the ^{6}Li problem by establishing more solidly the existence and height of the inferred ^{6}Li plateau in halo stars. However, it already seems that a substantial enhancement of the standard homogeneous BBN prediction for ^{6}Li/H might be an interesting signature of supersymmetric models.

The supersymmetric possibility of 'solving' the ^{7}Li problem and/or the possible ^{6}Li problem is currently at a very intriguing stage. Clearly, this approach to 'solving' the lithium problems would be given an enormous boost if experimental evidence were to emerge for supersymmetry, either at the LHC or in (in)direct searches for astrophysical dark matter. If supersymmetry were to be discovered, the search for evidence of a possible metastable supersymmetric particle and the LSP would assume high priority, and it would be an exciting challenge to correlate their possible roles in cosmology and in the laboratory.

References

[1] L. Maiani, Proceedings of the 1979 Gif-sur-Yvette Summer School on Particle Physics, 1; G. 't Hooft, in Recent Developments in Gauge Theories, Proceedings of the Nato Advanced Study Institute, Cargese, 1979, eds. G. 't Hooft *et al.*, (Plenum Press, NY, 1980); E. Witten, Phys. Lett. B **105**, 267 (1981).

[2] H. Georgi, H. R. Quinn and S. Weinberg, Phys. Rev. Lett. **33**, 451 (1974); P. Langacker, in Proc. PASCOS90 Symposium eds Nath P and Reucroft S World scientific, Singapore, 1990); J. R. Ellis, S. Kelley and D. V. Nanopoulos, Phys. Lett. B **260**, 131 (1991); U. Amaldi, W. de Boer and H. Furstenau, Phys. Lett. B **260**, 447 (1991); P. Langacker and M. -x. Luo, Phys. Rev. D **44**, 817 (1991); C. Giunti, C. W. Kim and U. W. Lee, Mod. Phys. Lett. A **6**, 1745 (1991).

[3] E. Komatsu *et al.* [WMAP Collaboration], Astrophys. J. Suppl. **192**, 18 (2011) [arXiv:1001.4538 [astro-ph.CO]].

[4] S. M. Faber and J. J. Gallagher, Ann. Rev. Astron. Astrophys. **17** (1979) 135; A. Bosma, Ap. J. **86** (1981) 1825; V. C. Rubin, W. K. Ford and N. Thonnard, Ap. J. **238** (1980) 471; V. C. Rubin, D. Burstein, W. K. Ford and N. Thonnard, Ap. J. **289** (1985) 81; T. S. Van Albada and R. Sancisi, Phil. Trans. R. Soc. Land. **A320** (1986) 447; M. Persic and P. Salucci, Ap. J. Supp. **99** (1995) 501; M. Persic, P. Salucci and F. Stel, Mon. Not. Roy. Astron. Soc. **281**, 27 (1996) [astro-ph/9506004].

[5] D. Wittman, *et al.*, Astrophys. J. **643**, 128 (2006) [arXiv:astro-ph/0507606].

[6] D. Clowe, *et al.*, Astrophys. J. **648** (2006) L109 [arXiv:astro-ph/0608407].

[7] K. A. Olive, arXiv:astro-ph/0301505.

[8] J. Wess and J. Bagger, *Supersymmetry and supergravity*, Princeton University Press, Princeton, USA (1992).

[9] H. P. Nilles, Phys. Rept. **110**, 1 (1984).

[10] H. E. Haber and G. L. Kane, Phys. Rept. **117** (1985) 75.

[11] H. J. W. Muller-Kirsten and A. Wiedemann, *Supersymmetry: An Introduction With Conceptual And Calculational Details*, Hackensack, USA: World Scientific (2010).

[12] S. P. Martin, [arXiv:hep-ph/9709356].

[13] K. A. Olive, [arXiv:hep-ph/9911307].

[14] I. R. Aitchison, [arXiv:hep-ph/0505105].

[15] M. Shifman, *Advanced topics in quantum field theory: A lecture course*, Cambridge, UK: Univ. Pr. (2012).

[16] For recent reviews on dark matter and supersymmetry searches, see J. Beringer *et al.* [Particle Data Group Collaboration], Phys. Rev. D **86**, 010001 (2012).

[17] K. A. Olive, G. Steigman and T. P. Walker, Phys. Rept. **333**, 389 (2000) [astro-ph/9905320].

[18] E. W. Kolb and M. S. Turner, *The Early Universe (Frontiers in Physics)*, (Addison-Wesley, Redwood City, CA, 1990).

[19] K. A. Olive, CERN Yellow Report CERN-2010-002, 149-196 [arXiv:1005.3955 [hep-ph]].

[20] K. A. Olive, D. N. Schramm and G. Steigman, Nucl. Phys. B **180**, 497 (1981).

[21] R. H. Cyburt, B. D. Fields, K. A. Olive and E. Skillman, Astropart. Phys. **23**, 313 (2005) [astro-ph/0408033].

[22] G. Mangano and P. D. Serpico, Phys. Lett. B **701**, 296 (2011) [arXiv:1103.1261 [astro-ph.CO]].

[23] D. Lindley, Astrophys. J. **294** (1985) 1.

[24] J. R. Ellis, D. V. Nanopoulos and S. Sarkar, Nucl. Phys. B **259** (1985) 175.

[25] D. Lindley, Phys. Lett. B **171** (1986) 235.

[26] R. J. Scherrer and M. S. Turner, Astrophys. J. **331** (1988) 19; Astrophys. J. **331** (1988) 33.

[27] M. H. Reno and D. Seckel, Phys. Rev. D **37** (1988) 3441.

[28] S. Dimopoulos, R. Esmailzadeh, L. J. Hall and G. D. Starkman, Astrophys. J. **330**, 545 (1988); S. Dimopoulos, R. Esmailzadeh, L. J. Hall and G. D. Starkman, Nucl. Phys. B **311** (1989) 699.

[29] J. Ellis *et al.*, Nucl. Phys. B **337**, 399 (1992).

[30] M. Kawasaki and T. Moroi, Prog. Theor. Phys. **93** (1995) 879 [arXiv:hep-ph/9403364].

[31] M. Kawasaki and T. Moroi, Astrophys. J. **452**, 506 (1995).

[32] E. Holtmann, M. Kawasaki, K. Kohri and T. Moroi, Phys. Rev. D **60**, 023506 (1999) [arXiv:hep-ph/9805405].

[33] K. Jedamzik, Phys. Rev. Lett. **84**, 3248 (2000) [arXiv:astro-ph/9909445].

[34] M. Kawasaki, K. Kohri and T. Moroi, Phys. Rev. D **63** (2001) 103502 [arXiv:hep-ph/0012279].

[35] K. Kohri, Phys. Rev. D **64** (2001) 043515 [arXiv:astro-ph/0103411].

[36] R. H. Cyburt, J. R. Ellis, B. D. Fields and K. A. Olive, Phys. Rev. D **67** (2003) 103521 [arXiv:astro-ph/0211258].

[37] K. Jedamzik, Phys. Rev. D **70** (2004) 063524 [arXiv:astro-ph/0402344].

[38] K. Jedamzik, Phys. Rev. D **70** (2004) 083510 [arXiv:astro-ph/0405583].

[39] M. Kawasaki, K. Kohri and T. Moroi, Phys. Lett. B **625** (2005) 7 [arXiv:astro-ph/0402490]; Phys. Rev. D **71** (2005) 083502 [arXiv:astro-ph/0408426].

[40] J. R. Ellis, K. A. Olive and E. Vangioni, Phys. Lett. B **619**, 30 (2005) [arXiv:astro-ph/0503023].

[41] K. Kohri, T. Moroi and A. Yotsuyanagi, Phys. Rev. D **73**, 123511 (2006) [arXiv:hep-ph/0507245].

[42] D. G. Cerdeno, K. Y. Choi, K. Jedamzik, L. Roszkowski and R. Ruiz de Austri, JCAP **0606**, 005 (2006) [arXiv:hep-ph/0509275].

[43] K. Jedamzik, K. Y. Choi, L. Roszkowski and R. Ruiz de Austri, JCAP **0607**, 007 (2006) [arXiv:hep-ph/0512044].

[44] K. Jedamzik, Phys. Rev. D **74**, 103509 (2006) [arXiv:hep-ph/0604251].

[45] F. D. Steffen, JCAP **0609**, 001 (2006) [arXiv:hep-ph/0605306].

[46] R. H. Cyburt, B. D. Fields and K. A. Olive, JCAP **0811** (2008) 012. [arXiv:0808.2818 [astro-ph]].

[47] R. H. Cyburt, J. Ellis, B. D. Fields, F. Luo, K. A. Olive and V. C. Spanos, JCAP **0910**, 021 (2009) [arXiv:0907.5003 [astro-ph.CO]].

[48] M. Drees and M. M. Nojiri, Phys. Rev. D **47** (1993) 376 [arXiv:hep-ph/9207234]; G. L. Kane, C. F. Kolda, L. Roszkowski and J. D. Wells, Phys. Rev. D **49** (1994) 6173 [arXiv:hep-ph/9312272]; H. Baer and M. Brhlik, Phys. Rev. D **53** (1996) 597 [arXiv:hep-ph/9508321]; Phys. Rev. D **57** (1998) 567 [arXiv:hep-ph/9706509]; J. R. Ellis, T. Falk, K. A. Olive and M. Schmitt, Phys. Lett. B **388** (1996) 97 [arXiv:hep-ph/9607292]; Phys. Lett. B **413** (1997) 355 [arXiv:hep-ph/9705444]; J. R. Ellis, T. Falk, G. Ganis, K. A. Olive and M. Schmitt, Phys. Rev. D **58** (1998) 095002 [arXiv:hep-ph/9801445]; V. D. Barger and C. Kao, Phys. Rev. D **57** (1998) 3131 [arXiv:hep-ph/9704403]; J. R. Ellis, T. Falk, G. Ganis and K. A. Olive, Phys. Rev. D **62** (2000) 075010 [arXiv:hep-ph/0004169]; J. R. Ellis,

T. Falk, G. Ganis, K. A. Olive and M. Srednicki, Phys. Lett. B **510** (2001) 236 [arXiv:hep-ph/0102098]; V. D. Barger and C. Kao, Phys. Lett. B **518** (2001) 117 [arXiv:hep-ph/0106189]; L. Roszkowski, R. Ruiz de Austri and T. Nihei, JHEP **0108** (2001) 024 [arXiv:hep-ph/0106334]; A. Djouadi, M. Drees and J. L. Kneur, JHEP **0108** (2001) 055 [arXiv:hep-ph/0107316]; U. Chattopadhyay, A. Corsetti and P. Nath, Phys. Rev. D **66** (2002) 035003 [arXiv:hep-ph/0201001]; J. R. Ellis, K. A. Olive and Y. Santoso, New Jour. Phys. **4** (2002) 32 [arXiv:hep-ph/0202110]; H. Baer, C. Balazs, A. Belyaev, J. K. Mizukoshi, X. Tata and Y. Wang, JHEP **0207** (2002) 050 [arXiv:hep-ph/0205325]; R. Arnowitt and B. Dutta, arXiv:hep-ph/0211417.

[49] J. R. Ellis, K. A. Olive, Y. Santoso and V. C. Spanos, Phys. Lett. B **573** (2003) 162 [arXiv:hep-ph/0305212]; J. R. Ellis, K. A. Olive, Y. Santoso and V. C. Spanos, Phys. Rev. D **70** (2004) 055005 [arXiv:hep-ph/0405110].

[50] D. V. Nanopoulos, K. A. Olive and M. Srednicki, Phys. Lett. B **127** (1983) 30.

[51] J. R. Ellis, J. E. Kim and D. V. Nanopoulos, Phys. Lett. B **145** (1984) 181.

[52] R. Juszkiewicz, J. Silk and A. Stebbins, Phys. Lett. B **158** (1985) 463.

[53] M. Kawasaki and K. Sato, Phys. Lett. B **189** (1987) 23.

[54] T. Moroi, H. Murayama and M. Yamaguchi, Phys. Lett. B **303** (1993) 289.

[55] T. Moroi, arXiv:hep-ph/9503210.

[56] J. R. Ellis, D. V. Nanopoulos, K. A. Olive and S. J. Rey, Astropart. Phys. **4** (1996) 371 [arXiv:hep-ph/9505438].

[57] M. Bolz, A. Brandenburg and W. Buchmuller, Nucl. Phys. B **606** (2001) 518 [arXiv:hep-ph/0012052].

[58] J. Pradler and F. D. Steffen, Phys. Lett. B **648**, 224 (2007) [arXiv:hep-ph/0612291].

[59] T. Sjostrand, P. Eden, C. Friberg, L. Lonnblad, G. Miu, S. Mrenna and E. Norrbin, Comput. Phys. Commun. **135** (2001) 238 [arXiv:hep-ph/0010017].

[60] R. H. Cyburt, J. Ellis, B. D. Fields, F. Luo, K. A. Olive and V. C. Spanos, JCAP **1010**, 032 (2010) [arXiv:1007.4173 [astro-ph.CO]].

[61] J. S. Hagelin, R. J. D. Parker and A. Hankey, Phys. Lett. B **215** (1988) 397; J. A. Frieman, E. W. Kolb and M. S. Turner, Phys. Rev. D **41** (1990) 3080; J. S. Hagelin and R. J. D. Parker, Nucl. Phys. B **329** (1990) 464.

[62] J. Hisano, M. Kawasaki, K. Kohri and K. Nakayama, Phys. Rev. D **79**, 063514 (2009) [Erratum-ibid. D **80**, 029907 (2009)] [arXiv:0810.1892 [hep-ph]].

[63] D. Thomas, D. N. Schramm, K. A. Olive and B. D. Fields, Astrophys. J. **406**, 569 (1993) [arXiv:astro-ph/9206002].

[64] E. Vangioni-Flam, M. Cassé, R. Cayrel, J. Audouze, M. Spite, and F. Spite, New Astronomy, **4**, 245 (1999) [arXiv:astro-ph/9811327].

[65] V.V. Smith, D.L. Lambert, and P.E. Nissen, Astrophys. J. **408**, 262 (1993); Astrophys. J. **506**, 405 (1998); L.M. Hobbs and J.A. Thorburn, Astrophys. J. Lett., **428**, L25 (1994); Astrophys. J. **491**, 772 (1997); R. Cayrel, M. Spite, F. Spite, E. Vangioni-Flam, M. Cassé, and J. Audouze, Astron. Astrophys. **343**, 923 (1999); P. E. Nissen, M. Asplund, V. Hill and S. D'Odorico, Astron. Astrophys. **357**, L49 (2000).

[66] M. Asplund, D. L. Lambert, P. E. Nissen, F. Primas and V. V. Smith, Astrophys. J. **644**, 229 (2006) [arXiv:astro-ph/0510636].

[67] R. Cayrel *et al.*, Astron. Astrophys. **473**, L37 (2007) [arXiv:0708.3819 [astro-ph]].

[68] M. Steffen, R. Cayrel, P. Bonifacio, H. G. Ludwig and E. Caffau, IAU Symposium, **265**, 23 (2010) [arXiv:0910.5917 [astro-ph.SR]].

[69] H. Baer, A. Mustafayev, S. Profumo, A. Belyaev and X. Tata, Phys. Rev. D **71**, 095008 (2005) [arXiv:hep-ph/0412059]; H. Baer, A. Mustafayev, S. Profumo, A. Belyaev and X. Tata, JHEP **0507**, 065 (2005) [arXiv:hep-ph/0504001].

[70] J. R. Ellis, K. A. Olive and P. Sandick, Phys. Rev. D **78**, 075012 (2008) [arXiv:0805.2343 [hep-ph]].

[71] J. Ellis, K. Olive and Y. Santoso, Phys. Lett. B **539**, 107 (2002) [arXiv:hep-ph/0204192]; J. R. Ellis, T. Falk, K. A. Olive and Y. Santoso, Nucl. Phys. B **652**, 259 (2003) [arXiv:hep-ph/0210205].

[72] J. Ellis, B. D. Fields, F. Luo, K. A. Olive and V. C. Spanos, Phys. Rev. D **84**, 123502 (2011) [arXiv:1109.0549 [astro-ph.CO]].

[73] F. Luo, K. A. Olive and M. Peloso, JHEP **1010**, 024 (2010) [arXiv:1006.5570 [hep-ph]].

[74] E. Cremmer, S. Ferrara, C. Kounnas and D. V. Nanopoulos, Phys. Lett. B **133**, 61 (1983); J. R. Ellis, A. B. Lahanas, D. V. Nanopoulos and K. Tamvakis, Phys. Lett. B **134**, 429 (1984); A. B. Lahanas and D. V. Nanopoulos, Phys. Rept. **145**, 1 (1987).

[75] J. Pradler, [arXiv:hep-ph/0708.2786].

[76] V. S. Rychkov and A. Strumia, Phys. Rev. D **75**, 075011 (2007) [arXiv:hep-ph/0701104].

[77] J. F. Gunion and H. E. Haber, Nucl. Phys. B **272** (1986) 1.

[78] J. Dunkley *et al.* [WMAP Collaboration], Astrophys. J. Suppl. **180**, 306 (2009) [arXiv:0803.0586 [astro-ph]].

[79] R. I. Epstein, J. M. Lattimer and D. N. Schramm, Nature **263**, 198 (1976); T. Prodanovic and B. D. Fields, Astrophys. J. **597**, 48 (2003) [arXiv:astro-ph/0307183].

[80] J. L. Linsky *et al.*, Astrophys. J. **647**, 1106 (2006) [arXiv:astro-ph/0608308].

[81] E. Vangioni-Flam, K. A. Olive and N. Prantzos, Astrophys. J. **427**, 618 (1994) [arXiv:astro-ph/9310021]; S. Scully, M. Casse, K. A. Olive and E. Vangioni-Flam, Astrophys. J. **476**, 521 (1997) [arXiv:astro-ph/9607106]; G. Steigman, D. Romano and M. Tosi, Mon. Not. Roy. Astron. Soc. **378**, 576 (2007) [arXiv:astro-ph/0703682]; T. Prodanovic and B. D. Fields, JCAP **0809**, 003 (2008) [arXiv:0804.3095 [astro-ph]].

[82] S. Burles and D. Tytler, Astrophys. J. **499**, 699 (1998) [arXiv:astro-ph/9712108].

[83] S. Burles and D. Tytler, Astrophys. J. **507**, 732 (1998) [arXiv:astro-ph/9712109].

[84] J. M. O'Meara, D. Tytler, D. Kirkman, N. Suzuki, J. X. Prochaska, D. Lubin and A. M. Wolfe, Astrophys. J. **552**, 718 (2001) [arXiv:astro-ph/0011179].

[85] M. Pettini and D. V. Bowen, Astrophys. J. **560**, 41 (2001) [arXiv:astro-ph/0104474].

[86] D. Kirkman, D. Tytler, N. Suzuki, J. M. O'Meara and D. Lubin, Astrophys. J. Suppl. **149**, 1 (2003) [arXiv:astro-ph/0302006].

[87] J. M. O'Meara, S. Burles, J. X. Prochaska, G. E. Prochter, R. A. Bernstein and K. M. Burgess, Astrophys. J. **649**, L61 (2006) [arXiv:astro-ph/0608302].

[88] M. Pettini, B. J. Zych, M. T. Murphy, A. Lewis and C. C. Steidel, MNRAS **391**, 1499 (2008) [arXiv:0805.0594 [astro-ph]].

[89] R. H. Cyburt, B. D. Fields and K. A. Olive, New Astron. **6** (2001) 215 [arXiv:astro-ph/0102179].

[90] Bania, T. M., Rood, R. T., & Balser, D. S. 2002, Nature, **415**, 54.

[91] E. Vangioni-Flam, K. A. Olive, B. D. Fields and M. Casse, Astrophys. J. **585**, 611 (2003) [arXiv:astro-ph/0207583].

[92] B. D. Fields, K. A. Olive, J. Silk, M. Casse and E. Vangioni-Flam, Astrophys. J. **563**, 653 (2001) [arXiv:astro-ph/0107389].

[93] G. Sigl, K. Jedamzik, D. N. Schramm and V. S. Berezinsky, Phys. Rev. D **52** (1995) 6682 [arXiv:astro-ph/9503094].

[94] K. A. Olive and E. D. Skillman, New Astronomy, **6**, 119 (2001).

[95] K. A. Olive and E. D. Skillman, Astrophys. J. **617**, 29 (2004) [arXiv:astro-ph/0405588].

[96] E. Aver, K. A. Olive and E. D. Skillman, JCAP **1005**, 003 (2010) [arXiv:1001.5218 [astro-ph.CO]].

[97] Y. I. Izotov and T. X. Thuan, Astrophys. J. **710**, L67 (2010) [arXiv:1001.4440 [astro-ph.CO]].

[98] F. Spite, M. Spite, Astronomy & Astrophysics, **115** (1992) 357.

[99] S. G. Ryan, T. C. Beers, K. A. Olive, B. D. Fields and J. E. Norris, Astrophys. J. Lett. **530** (2000) L57 [arXiv:astro-ph/9905211].

[100] P. Bonifacio *et al.*, Astron. Astrophys., **390**, 91 (2002). [arXiv:astro-ph/0204332].

[101] L. Pasquini and P. Molaro, Astron. Astrophys. **307**, 761 (1996).

[102] F. Thevenin, C. Charbonnel, J. A. d. Pacheco, T. P. Idiart, G. Jasniewicz, P. de Laverny and B. Plez, Astron. Astrophys. **373**, 905 (2001) [arXiv:astro-ph/0105166].

[103] P. Bonifacio, Astron. Astrophys. **395**, 515 (2002) [arXiv:astro-ph/0209434].

[104] K. Lind, F. Primas, C. Charbonnel, F. Grundahl and M. Asplund, Astron. Astrophys. **503**, 545 (2009) [arXiv:0906.2876 [astro-ph.SR]].

[105] J. I. G. Hernandez *et al.*, Astron. Astrophys. **505**, L13 (2009) [arXiv:0909.0983 [astro-ph.GA]].

[106] R. H. Cyburt and M. Pospelov, Int. J. Mod. Phys. E **21**, 1250004 (2012) [arXiv:0906.4373 [astro-ph.CO]]; N. Chakraborty, B. D. Fields and K. A. Olive, Phys. Rev. D **83** (2011) 063006 [arXiv:1011.0722 [astro-ph.CO]].

[107] A. Hosford, S. G. Ryan, A. E. G. Perez, J. E. Norris and K. A. Olive, Astron. Astrophys. **493**, 601 (2009) [arXiv:0811.2506 [astro-ph]].

[108] S. Vauclair and C. Charbonnel, Astrophys. J. **502**, 372 (1998); M. H. Pinsonneault, T. P. Walker, G. Steigman and V. K. Narayanan, Astrophys. J. **527**, 180 (2002) [arXiv:astro-ph/9803073]; M. H. Pinsonneault, G. Steigman, T. P. Walker and V. K. Narayanan, Astrophys. J. **574**, 398 (2002) [arXiv:astro-ph/0105439]; O. Richard, G. Michaud and J. Richer, Astrophys. J. **619**, 538 (2005) [arXiv:astro-ph/0409672]; A. J. Korn *et al.*, Nature **442** (2006) 657 [arXiv:astro-ph/0608201].

[109] G. Steigman, B. D. Fields, K. A. Olive, D. N. Schramm and T. P. Walker, Astrophys. J. **415**, L35 (1993).

[110] B. D. Fields and K. A. Olive, New Astronomy, **4**, 255 (1999) [arXiv:astro-ph/9811183].

[111] R. H. Cyburt, J. R. Ellis, B. D. Fields, K. A. Olive and V. C. Spanos, JCAP **0611**, 014 (2006) [arXiv:astro-ph/0608562].

[112] M. Kusakabe, T. Kajino and G. J. Mathews, Phys. Rev. D **74**, 023526 (2006) [arXiv:astro-ph/0605255]; M. Kusakabe, T. Kajino, R. N. Boyd, T. Yoshida and G. J. Mathews, Phys. Rev. D **76**, 121302 (2007) [arXiv:0711.3854 [astro-ph]]; M. Kusakabe, T. Kajino, R. N. Boyd, T. Yoshida and G. J. Mathews, arXiv:0711.3858 [astro-ph].

[113] K. Jedamzik, JCAP **0803**, 008 (2008) [arXiv:0710.5153 [hep-ph]].

[114] D. Cumberbatch, K. Ichikawa, M. Kawasaki, K. Kohri, J. Silk and G. D. Starkman, Phys. Rev. D **76**, 123005 (2007) [arXiv:0708.0095 [astro-ph]].

[115] S. Bailly, K. Jedamzik and G. Moultaka, Phys. Rev. D **80**, 063509 (2009) [arXiv:0812.0788 [hep-ph]]; S. Bailly, K. Y. Choi, K. Jedamzik and L. Roszkowski, JHEP **0905**, 103 (2009) [arXiv:0903.3974 [hep-ph]].

[116] E. Rollinde, E. Vangioni-Flam and K. A. Olive, Astrophys. J. **627**, 666 (2005) [arXiv:astro-ph/0412426]; E. Rollinde, E. Vangioni and K. A. Olive, Astrophys. J. **651**, 658 (2006) [arXiv:astro-ph/0605633]; E. Rollinde, D. Maurin, E. Vangioni, K. A. Olive and S. Inoue, Astrophys. J. **673**, 676 (2008) [arXiv:0707.2086 [astro-ph]]; T. Prodanovic and B. D. Fields, Phys. Rev. D **76**, 083003 (2007) [arXiv:0709.3300 [astro-ph]]; M. Kusakabe, arXiv:0803.3401 [astro-ph].

[117] L. Brown and D. N. Schramm, Astrophys. J. **329**, L103 (1988).

[118] J. Ellis, J.S. Hagelin, D.V. Nanopoulos, K.A. Olive and M. Srednicki, *Nucl. Phys.* **B238**, 453 (1984).

[119] J. P. Meyer, Astron. & Astrophys. Suppl. **7**, 417 (1972).

[120] P. Mohr *et al.*, Phys. Rev. C **50**, 1543 (1994).

[121] R. H. Cyburt, Phys. Rev. D **70**, 023505 (2004) [arXiv:astro-ph/0401091].

[122] R. H. Cyburt and B. Davids, Phys. Rev. C **78**, 064614 (2008) [arXiv:0809.3240 [nucl-ex]].

[123] S. Ando, R. H. Cyburt, S. W. Hong and C. H. Hyun, Phys. Rev. C **74**, 025809 (2006) [arXiv:nucl-th/0511074].

[124] J. R. Ellis, K. A. Olive, Y. Santoso and V. C. Spanos, Phys. Lett. B **565**, 176 (2003) [arXiv:hep-ph/0303043].

[125] M. Battaglia *et al.*, Eur. Phys. J. C **22**, 535 (2001) [arXiv:hep-ph/0106204]; M. Battaglia, A. De Roeck, J. R. Ellis, F. Gianotti, K. A. Olive and L. Pape, Eur. Phys. J. C **33**, 273 (2004) [arXiv:hep-ph/0306219].

[126] J. L. Feng, A. Rajaraman and F. Takayama, Phys. Rev. D **68** (2003) 063504 [arXiv:hep-ph/0306024]; J. L. Feng, S. F. Su and F. Takayama, Phys. Rev. D **70** (2004) 063514 [arXiv:hep-ph/0404198].

[127] J. L. Feng, S. Su and F. Takayama, Phys. Rev. D **70** (2004) 075019 [arXiv:hep-ph/0404231].

[128] J. F. Gunion and H. E. Haber, Phys. Rev. D **37** (1988) 2515.

[129] S. Chen *et al.* [CLEO Collaboration], Phys. Rev. Lett. **87** (2001) 251807 [arXiv:hep-ex/0108032]; P. Koppenburg *et al.* [Belle Collaboration], Phys. Rev. Lett. **93** (2004) 061803 [arXiv:hep-ex/0403004]; B. Aubert *et al.* [BaBar Collaboration], arXiv:hep-ex/0207076; E. Barberio *et al.* [Heavy Flavor Averaging Group (HFAG)], arXiv:hep-ex/0603003.

[130] The solid part of the purple line in Fig. 7.1 represents results reported by the CMS Collaboration: S. Chatrchyan *et al.* [CMS Collaboration], Phys. Rev. Lett. **107**, 221804 (2011) [arXiv:1109.2352 [hep-ex]];
and the dotted part of the purple line represents results reported by the ATLAS Collaboration: G. Aad *et al.* [ATLAS Collaboration], Phys. Lett. B **710**, 67 (2012) [arXiv:1109.6572 [hep-ex]].

[131] [The Muon g-2 Collaboration], Phys. Rev. Lett. **92** (2004) 161802, [arXiv:hep-ex/0401008]; G. Bennett et al. [The Muon g-2 Collaboration], Phys. Rev. **D 73** (2006) 072003 [arXiv:hep-ex/0602035]; D. Stockinger, J. Phys. G **34** (2007) R45 [arXiv:hep-ph/0609168]; J. Miller, E. de Rafael and B. Roberts, Rept. Prog. Phys. **70** (2007) 795 [arXiv:hep-ph/0703049]; J. Prades, E. de Rafael and A. Vainshtein, arXiv:0901.0306 [hep-ph]; F. Jegerlehner and A. Nyffeler, Phys. Rept. **477**, 1 (2009) [arXiv:0902.3360 [hep-ph]]; M. Davier, A. Hoecker, B. Malaescu, C. Z. Yuan and Z. Zhang, Eur. Phys. J. C **66**, 1 (2010) [arXiv:0908.4300 [hep-ph]]; J. Prades, Acta Phys. Polon. Supp. **3**, 75 (2010) [arXiv:0909.2546 [hep-ph]]; T. Teubner, K. Hagiwara, R. Liao, A. D. Martin and D. Nomura, Chin. Phys. C **34**, 728 (2010) [arXiv:1001.5401 [hep-ph]].

[132] M. Davier, A. Hoecker, B. Malaescu and Z. Zhang, Eur. Phys. J. C **71**, 1515 (2011) [Erratum-ibid. C **72**, 1874 (2012)] [arXiv:1010.4180 [hep-ph]].

[133] J. Ellis, K. A. Olive and V. C. Spanos, JCAP **1110**, 024 (2011) [arXiv:1106.0768 [hep-ph]].

[134] A. Strumia, JHEP **1104** (2011) 073 [arXiv:1101.2195 [hep-ph]]; D. Feldman, K. Freese, P. Nath, B. D. Nelson and G. Peim, Phys. Rev. D **84**, 015007 (2011) [arXiv:1102.2548 [hep-ph]]; B. C. Allanach, Phys. Rev. D **83**, 095019 (2011) [arXiv:1102.3149 [hep-ph]]; S. Scopel, S. Choi, N. Fornengo and A. Bottino, Phys. Rev. D **83**, 095016 (2011) [arXiv:1102.4033 [hep-ph]]; O. Buchmueller, R. Cavanaugh, D. Colling, A. de Roeck, M. J. Dolan, J. R. Ellis, H. Flacher and S. Heinemeyer *et al.*, Eur. Phys. J. C **71**, 1634 (2011) [arXiv:1102.4585 [hep-ph]]; P. Bechtle, B. Sarrazin, K. Desch, H. K. Dreiner, P. Wienemann, M. Kramer, C. Robens and B. O'Leary, Phys. Rev. D **84**, 011701 (2011) [arXiv:1102.4693 [hep-ph]]; B. C. Allanach, T. J. Khoo, C. G. Lester and S. L. Williams, JHEP **1106**, 035 (2011) [arXiv:1103.0969 [hep-ph]]; S. Akula, N. Chen, D. Feldman, M. Liu, Z. Liu, P. Nath and G. Peim, Phys. Lett. B **699**, 377 (2011) [arXiv:1103.1197 [hep-ph]]; S. Akula, D. Feldman, Z. Liu, P. Nath and G. Peim, Mod. Phys. Lett. A **26**, 1521 (2011) [arXiv:1103.5061 [hep-ph]]; M. J. Dolan, D. Grellscheid, J. Jaeckel,

V. V. Khoze and P. Richardson, JHEP **1106**, 095 (2011) [arXiv:1104.0585 [hep-ph]]; M. Farina, M. Kadastik, D. Pappadopulo, J. Pata, M. Raidal and A. Strumia, Nucl. Phys. B **853**, 607 (2011) [arXiv:1104.3572 [hep-ph]]; O. Buchmueller, R. Cavanaugh, D. Colling, A. De Roeck, M. J. Dolan, J. R. Ellis, H. Flacher and S. Heinemeyer *et al.*, Eur. Phys. J. C **71**, 1722 (2011) [arXiv:1106.2529 [hep-ph]]; A. Strumia, arXiv:1107.1259 [hep-ph]; G. Bertone, D. G. Cerdeno, M. Fornasa, R. Ruiz de Austri, C. Strege and R. Trotta, JCAP **1201**, 015 (2012) [arXiv:1107.1715 [hep-ph]].

Appendix A

Single Gravitino-MSSM Vertices with Broken Electroweak Symmetry

We write here all the interactions of a single on-shell gravitino with MSSM fields (we also include the term (2.19) worked out in the main text). Besides the relations already written in Section 2.2, we also use the Higgs decomposition [77]

$$\begin{aligned} H_2^1 &= H^+ \cos\beta,\ H_1^2 = H^- \sin\beta, \\ H_1^1 &= v_1 + \frac{1}{\sqrt{2}}\left(H_1^0 \cos\alpha - H_2^0 \sin\alpha + iH_3^0 \sin\beta\right), \\ H_2^2 &= v_2 + \frac{1}{\sqrt{2}}\left(H_1^0 \sin\alpha + H_2^0 \cos\alpha + iH_3^0 \cos\beta\right), \end{aligned} \tag{A.1}$$

the sfermion rotation between the mass eigenstates $\tilde{f}_1,\ \tilde{f}_2$ and the interaction eigenstates $\tilde{f}_L,\ \tilde{f}_R$ [1]

$$\begin{pmatrix} \tilde{f}_1 \\ \tilde{f}_2 \end{pmatrix} = \begin{pmatrix} c_f & -s_f^* \\ s_f & c_f^* \end{pmatrix} \begin{pmatrix} \tilde{f}_L \\ \tilde{f}_R \end{pmatrix} \quad , \quad |c_f|^2 + |s_f|^2 = 1 \tag{A.2}$$

[1] We denote the chiral multiplets associated to SM l.h. fermions by $(P_L\nu,\ \tilde{\nu}_L)$, $(P_L e,\ \tilde{e}_L)$, $(P_L u,\ \tilde{u}_L)$, $\left(P_L d,\ \tilde{d}_L\right)$, and the multiplets associated to SM r.h. fermions by $(P_L e^c,\ \tilde{e}_R^*)$, $(P_L u^c,\ \tilde{u}_R^*)$, $\left(P_L d^c,\ \tilde{d}_R^*\right)$; family indices are understood.

and the relations between the gaugino, and neutralino/chargino mass eigenstates [77]

$$\begin{aligned}
\tilde{B} &= (N_{i1}^{*}\,P_L + N_{i1}\,P_R)\,\tilde{\chi}_i^0\,, \\
\tilde{W}^3 &= (N_{i2}^{*}\,P_L + N_{i2}\,P_R)\,\tilde{\chi}_i^0\,, \\
\frac{\tilde{A}^1 - i\tilde{A}^2}{\sqrt{2}} &\equiv \tilde{W} = \left(V_{j1}^{*}\,P_L + U_{j1}\,P_R\right)\tilde{\chi}_j\,, \\
\Rightarrow\ \frac{\tilde{A}^1 + i\tilde{A}^2}{\sqrt{2}} &\equiv \tilde{W}^c = \left(U_{j1}^{*}\,P_L + V_{j1}\,P_R\right)\tilde{\chi}_j^c\,.
\end{aligned} \tag{A.3}$$

We find

$$\begin{aligned}
\mathcal{L}_{\rm int} &= \mathcal{L}_{W\tilde{\chi}} + \mathcal{L}_{\gamma\tilde{\chi}^0} + \mathcal{L}_{Z\tilde{\chi}^0} + \mathcal{L}_{H\tilde{\chi}} + \mathcal{L}_{H^0\tilde{\chi}^0} + \mathcal{L}_{f\tilde{f}} + \mathcal{L}_{G\tilde{G}} \\
&\quad + \mathcal{L}_{WH^0\tilde{\chi}} + \mathcal{L}_{WH\tilde{\chi}^0} + \mathcal{L}_{WW\tilde{\chi}^0} + \mathcal{L}_{Wf\tilde{f}} + \mathcal{L}_{\gamma H\tilde{\chi}} + \mathcal{L}_{\gamma f\tilde{f}} + \mathcal{L}_{ZH\tilde{\chi}} \\
&\quad + \mathcal{L}_{ZH^0\tilde{\chi}^0} + \mathcal{L}_{Zf\tilde{f}} + \mathcal{L}_{W\gamma\tilde{\chi}} + \mathcal{L}_{WZ\tilde{\chi}} + \mathcal{L}_{GG\tilde{G}} + \mathcal{L}_{Gf\tilde{f}}
\end{aligned} \tag{A.4}$$

where

$$\begin{aligned}
\mathcal{L}_{W\tilde{\chi}} &= -\frac{\bar{\psi}_\mu}{M_P}\Big[\left(\sqrt{2}\,M_W\,\cos\beta\,U_{j2}^{*}\,\eta^{\mu\sigma} + \frac{i}{4}\,[\gamma^\rho,\,\gamma^\sigma]\,\gamma^\mu\,U_{j1}^{*}\partial_\rho^{(W)}\right)P_L \\
&\qquad + \left(\sqrt{2}\,M_W\,\sin\beta\,V_{j2}\,\eta^{\mu\sigma} + \frac{i}{4}\,[\gamma^\rho,\,\gamma^\sigma]\,\gamma^\mu\,V_{j1}\partial_\rho^{(W)}\right)P_R\Big]W_\sigma^{+}\,\tilde{\chi}_j^c \\
&\quad -\frac{\bar{\psi}_\mu}{M_P}\Big[\left(\sqrt{2}\,M_W\,\cos\beta\,U_{j2}\,\eta^{\mu\sigma} + \frac{i}{4}\,[\gamma^\rho,\,\gamma^\sigma]\,\gamma^\mu\,U_{j1}\partial_\rho^{(W)}\right)P_R \\
&\qquad + \left(\sqrt{2}\,M_W\,\sin\beta\,V_{j2}^{*}\,\eta^{\mu\sigma} + \frac{i}{4}\,[\gamma^\rho,\,\gamma^\sigma]\,\gamma^\mu\,V_{j1}^{*}\partial_\rho^{(W)}\right)P_L\Big]W_\sigma^{-}\,\tilde{\chi}_j
\end{aligned} \tag{A.5}$$

$$\begin{aligned}
\mathcal{L}_{\gamma\tilde{\chi}^0} &= -\frac{i}{4\,M_P}\,\bar{\psi}_\mu\,[\gamma^\rho,\,\gamma^\sigma]\,\gamma^\mu\,\partial_\rho\,A_\sigma\big[\,(\cos\theta_w\,N_{i1}^{*} + \sin\theta_w\,N_{i2}^{*})\,P_L \\
&\qquad + (\cos\theta_w\,N_{i1} + \sin\theta_w\,N_{i2})\,P_R\big]\tilde{\chi}_i^0
\end{aligned} \tag{A.6}$$

$$\begin{aligned}
\mathcal{L}_{Z\tilde{\chi}^0} &= -\frac{1}{M_P}\bar{\psi}_\mu\Big\{\big[M_Z\,(\cos\beta\,N_{i3}^{*} - \sin\beta\,N_{i4}^{*})\,\eta^{\mu\sigma} \\
&\qquad + \frac{i}{4}\,[\gamma^\rho,\,\gamma^\sigma]\,\gamma^\mu\,(\cos\theta_w\,N_{i2}^{*} - \sin\theta_w\,N_{i1}^{*})\,\partial_\rho^{(Z)}\big]P_L \\
&\qquad + \big[M_Z\,(\cos\beta\,N_{i3} - \sin\beta\,N_{i4})\,\eta^{\mu\sigma} \\
&\qquad + \frac{i}{4}\,[\gamma^\rho,\,\gamma^\sigma]\,\gamma^\mu\,(\cos\theta_w\,N_{i2} - \sin\theta_w\,N_{i1})\,\partial_\rho^{(Z)}\big]P_R\Big\}Z_\sigma\,\tilde{\chi}_i^{(0)}
\end{aligned} \tag{A.7}$$

$$\mathcal{L}_{H\tilde{\chi}} = -\frac{1}{M_P}\,\bar{\psi}_\mu\,\sqrt{2}\,i\,\partial^\mu H^+\left(\sin\beta\,U^*_{j2}\,P_L - \cos\beta\,V_{j2}\,P_R\right)\tilde{\chi}^c_j + \text{h. c.} \tag{A.8}$$

$$\begin{aligned}\mathcal{L}_{H^0\tilde{\chi}^0} = -\frac{1}{M_P}\,\bar{\psi}_\mu\Big\{ & i\left[(\cos\alpha\,N^*_{i3} + \sin\alpha\,N^*_{i4})\,P_L - (\cos\alpha\,N_{i3} + \sin\alpha\,N_{i4})\,P_R\right]\partial^\mu H^0_1\,\tilde{\chi}^0_i \\ & + i\left[(-\sin\alpha\,N^*_{i3} + \cos\alpha\,N^*_{i4})\,P_L - (-\sin\alpha\,N_{i3} + \cos\alpha\,N_{i4})\,P_R\right]\partial^\mu H^0_2\,\tilde{\chi}^0_i \\ & + \left[(\sin\beta\,N^*_{i3} + \cos\beta\,N^*_{i4})\,P_L + (\sin\beta\,N_{i3} + \cos\beta\,N_{i4})\,P_R\right]\partial^\mu H^0_3\,\tilde{\chi}^0_i\Big\}\end{aligned} \tag{A.9}$$

$$\begin{aligned}\mathcal{L}_{f\tilde{f}} = -\frac{1}{M_P}\,\bar{\psi}_\mu\,\sqrt{2}\,i\Big[& \sum_{f=\nu,e,u,d}\left(c_f\,\partial^\mu\tilde{f}^*_1 + s_f\,\partial^\mu\tilde{f}^*_2\right)P_L\,f + \\ & \sum_{f=e,u,d}\left(-s_f\,\partial^\mu\tilde{f}_1 + c_f\,\partial^\mu\tilde{f}_2\right)P_L\,f^c\Big] + \text{h. c.}\end{aligned} \tag{A.10}$$

$$\mathcal{L}_{G\tilde{G}} = -\frac{i}{4\,M_P}\,\bar{\psi}_\mu\,\left[\gamma^\rho,\,\gamma^\sigma\right]\gamma^\mu\,\partial_\rho\,G^a_\sigma\,\tilde{G}^a \tag{A.11}$$

$$\begin{aligned}\mathcal{L}_{WH^0\tilde{\chi}} = -\frac{1}{M_P}\,\bar{\psi}_\mu\,\frac{g}{\sqrt{2}}\Big[& \left(\cos\alpha\,U^*_{j2}\,P_L + \sin\alpha\,V_{j2}\,P_R\right)H^0_1 \\ & + \left(-\sin\alpha\,U^*_{j2}\,P_L + \cos\alpha\,V_{j2}\,P_R\right)H^0_2 \\ & + i\left(-\sin\beta\,U^*_{j2}\,P_L + \cos\beta\,V_{j2}\,P_R\right)H^0_3\Big]W^{\mu+}\,\tilde{\chi}^c_j + \text{h. c.}\end{aligned} \tag{A.12}$$

$$\mathcal{L}_{WH\tilde{\chi}^0} = -\frac{1}{M_P}\,\bar{\psi}_\mu\,g\,(\cos\beta\,N^*_{i4}\,P_L + \sin\beta\,N_{i3}\,P_R)\,W^{\mu+}\,H^-\,\tilde{\chi}^0_i + \text{h. c.} \tag{A.13}$$

$$\mathcal{L}_{WW\tilde{\chi}^0} = \frac{g}{4\,M_P}\,\bar{\psi}_\mu\,\left[\gamma^\rho,\,\gamma^\sigma\right]\gamma^\mu\,(N^*_{i2}\,P_L + N_{i2}\,P_R)\,W^+_\rho\,W^-_\sigma\,\tilde{\chi}^0_i \tag{A.14}$$

$$\begin{aligned}\mathcal{L}_{Wf\tilde{f}} = -\frac{1}{M_P}\,\bar{\psi}_\mu\,g\Big\{ & W^{\mu+}\left[(c_\nu\,\tilde{\nu}^*_1 + s_\nu\,\tilde{\nu}^*_2)\,P_L\,e + (c_u\,\tilde{u}^*_1 + s_u\,\tilde{u}^*_2)\,P_L\,d\right] \\ & + W^{\mu-}\left[(c_e\,\tilde{e}^*_1 + s_e\,\tilde{e}^*_2)\,P_L\,\nu + \left(c_d\,\tilde{d}^*_1 + s_d\,\tilde{d}^*_2\right)P_L\,u\right]\Big\} + \text{h. c.}\end{aligned} \tag{A.15}$$

$$\mathcal{L}_{\gamma H\tilde{\chi}} = -\frac{1}{M_P}\,\bar{\psi}_\mu\,\sqrt{2}\,e\left(-\sin\beta\,U^*_{j2}\,P_L + \cos\beta\,V_{j2}\,P_R\right)A^\mu\,H^+\,\tilde{\chi}^c_j + \text{h. c.} \tag{A.16}$$

$$\mathcal{L}_{\gamma f\tilde{f}} = -\frac{1}{M_P}\,\bar{\psi}_\mu\,\sqrt{2}\,e\,A^\mu\sum_{f=e,u,d}q_f\left[\left(c_f\tilde{f}^*_1 + s_f\tilde{f}^*_2\right)P_Lf - \left(-s_f\tilde{f}_1 + c_f\tilde{f}_2\right)P_Lf^c\right] + \text{h. c.} \tag{A.17}$$

$$\mathcal{L}_{ZH\tilde{\chi}} = -\frac{1}{M_P}\,\bar{\psi}_\mu\,\frac{g\left(\cos^2\theta_w - \sin^2\theta_w\right)}{\sqrt{2}\,\cos\theta_w}\left(-\sin\beta\,U^*_{j2}\,P_L + \cos\beta\,V_{j2}\,P_R\right)Z^\mu\,H^+\,\tilde{\chi}^c_j + \text{h. c.} \tag{A.18}$$

$$\begin{aligned}\mathcal{L}_{ZH^0\tilde{\chi}^0} \;=\; & -\frac{1}{M_P}\,\bar{\psi}_\mu\,\frac{g}{2\,\cos\,\theta_w}\Big\{\big[\,(\cos\alpha\,N^*_{i3} - \sin\alpha\,N^*_{i4})\,P_L \\ & + (\cos\alpha\,N_{i3} - \sin\alpha\,N_{i4})\,P_R\big]Z^\mu\,H^0_1\,\tilde{\chi}^0_i \\ & - \left[(\sin\alpha\,N^*_{i3} + \cos\alpha\,N^*_{i4})\,P_L + (\sin\alpha\,N_{i3} + \cos\alpha\,N_{i4})\,P_R\right]Z^\mu\,H^0_2\,\tilde{\chi}^0_i \\ & - i\left[(\sin\beta\,N^*_{i3} - \cos\beta\,N^*_{i4})\,P_L - (\sin\beta\,N_{i3} - \cos\beta\,N_{i4})\,P_R\right]Z^\mu\,H^0_3\,\tilde{\chi}^0_i\Big\}\end{aligned} \tag{A.19}$$

$$\begin{aligned}\mathcal{L}_{Zf\tilde{f}} \;=\; & -\frac{1}{M_P}\,\bar{\psi}_\mu\,\frac{\sqrt{2}\,g\,Z^\mu}{\cos\theta_w}\Bigg[\sum_{f=\nu,e,u,d} Z^f_L\left(c_f\,\tilde{f}^*_1 + s_f\,\tilde{f}^*_2\right)P_L\,f \\ & - \sum_{f=e,u,d} Z^f_R\left(-s_f\,\tilde{f}_1 + c_f\,\tilde{f}_2\right)P_L\,f^c\Bigg] + \text{h. c.}\end{aligned} \tag{A.20}$$

$$\mathcal{L}_{W\gamma\tilde{\chi}} = -\frac{g}{4\,M_P}\,\bar{\psi}_\mu\,\left[\gamma^\rho,\,\gamma^\sigma\right]\gamma^\mu\,W^+_\rho\,\sin\theta_w A_\sigma\left(U^*_{j1}\,P_L + V_{j1}\,P_R\right)\tilde{\chi}^c_j + \text{h.c.} \tag{A.21}$$

$$\mathcal{L}_{WZ\tilde{\chi}} = -\frac{g}{4\,M_P}\,\bar{\psi}_\mu\,\left[\gamma^\rho,\,\gamma^\sigma\right]\gamma^\mu\,W^+_\rho\,\cos\theta_w Z_\sigma\left(U^*_{j1}\,P_L + V_{j1}\,P_R\right)\tilde{\chi}^c_j + \text{h.c.} \tag{A.22}$$

$$\mathcal{L}_{GG\tilde{G}} = \frac{i\,g_s}{8\,M_P}\,\bar{\psi}_\mu\,\left[\gamma^\rho,\,\gamma^\sigma\right]\gamma^\mu\,f^{abc}\,\tilde{G}^a\,G^b_\rho\,G^c_\sigma \tag{A.23}$$

$$\begin{aligned}\mathcal{L}_{Gf\tilde{f}} \;=\; & -\frac{1}{M_P}\,\bar{\psi}_\mu\,\frac{g_s}{\sqrt{2}}G^{a\mu}\sum_{f=u,d}\Bigg[\left(c_f\,\lambda^{a*}\,\tilde{f}^*_1 + s_f\,\lambda^{a*}\,\tilde{f}^*_2\right)_i\,P_L\,f_i \\ & - \left(-s_f\,\lambda^a\,\tilde{f}_1 + c_f\,\lambda^a\,\tilde{f}_2\right)_i\,P_L\,f^c_i\Bigg] + \text{h.c.}\end{aligned} \tag{A.24}$$

In the above expressions, $\partial^{(W)}$, and $\partial^{(Z)}$ denote a derivative acting only on the W, and Z fields, respectively; q_f denotes the electric charge of the fermion f; $Z^f_L = \frac{1}{2},\,-\frac{1}{2}+\sin^2\theta_w,\,\frac{1}{2}-\frac{2}{3}\sin^2\theta_w,\,-\frac{1}{2}+\frac{1}{3}\sin^2\theta_w$ for ν, e, u, d, respectively; $Z^f_R = \sin^2\theta_w,\,-\frac{2}{3}\sin^2\theta_w,\,\frac{1}{3}\sin^2\theta_w$ for e, u, d, respectively; λ^a are the Gell-Mann matrices. Moreover, in some of the above expressions we have also used the identities

$$\left(\bar{\psi}_\mu\,P_L\,\tilde{\chi}_j\right)^\dagger = \bar{\tilde{\chi}}_j\,P_R\,\psi_\mu = \bar{\psi}_\mu\,P_R\,\tilde{\chi}^c_j \quad , \quad \left(\bar{\psi}_\mu\,\left[\gamma^\rho,\,\gamma^\sigma\right]\gamma^\mu\,P_L\,\tilde{\chi}^c_j\right)^\dagger = -\bar{\psi}_\mu\,\left[\gamma^\rho,\,\gamma^\sigma\right]\gamma^\mu\,P_R\,\tilde{\chi}_j \tag{A.25}$$

Appendix B

Gravitino Decay Amplitudes

Following the discussion on the CMSSM in Section 2.1, we take into account the left-right mixing for the third generation of squarks and sleptons, while we do not consider mixing among generations. We treat the neutrinos as in the Standard Model, i.e., as massless, purely left-handed neutrinos (and right-handed anti-neutrinos) only. To facilitate the description below, we rewrite eq. (A.2) in a more abstract form:

$$\begin{pmatrix} \widetilde{t}_L \\ \widetilde{t}_R \end{pmatrix} = \begin{pmatrix} U_{\widetilde{t}\,1L} & U_{\widetilde{t}\,2L} \\ U_{\widetilde{t}\,1R} & U_{\widetilde{t}\,2R} \end{pmatrix} \begin{pmatrix} \widetilde{t}_1 \\ \widetilde{t}_2 \end{pmatrix}, \tag{B.1}$$

where the transformation matrix is unitary. There are similar interaction/mass-eigenstate transformations for $\widetilde{b}$ and $\tilde{\tau}$. The other transformations of the fields between interaction- and mass-eigenstate are given in Section 2.2 and Appendix A.

First we list the amplitudes for all the two-body gravitino decay channels. We denote by m_b and m_f the masses of the final-state bosons and fermions, respectively. For $\widetilde{G} \to \tilde{\chi}_i^0\,\gamma$ and $\widetilde{G} \to \tilde{g}\,g$, we have:

$$\overline{|\mathcal{M}|^2} = \frac{1}{6\,m_{3/2}^2 M_P^2}\,|B|^2\left(3\,m_{3/2}^2 + m_f^2\right)\left(m_{3/2}^2 - m_f^2\right)^2, \tag{B.2}$$

where $B = N'_{i1}$ for the $\tilde{\chi}_i^0$ final states, with $N'_{i1} = N_{i1}\cos\theta_W + N_{i2}\sin\theta_W$, and θ_W is the weak mixing angle, and $B = 1$ for the $\tilde{g}$ final state. For $\widetilde{G} \to \tilde{\chi}_j^{\pm}\,W^{\mp}$ and $\widetilde{G} \to \tilde{\chi}_i^0\,Z$,

we have:

$$\begin{aligned}
\overline{|\mathcal{M}|^2} &= \frac{1}{12\,m_{3/2}^2 M_P^2}\Big\{12\,(C\,D+C^*D^*)\,m_{3/2}^3 m_b^2 m_f + \Big(|C|^2+|D|^2\Big) \\
&\quad\times\Big[3\,m_{3/2}^6 - m_{3/2}^4\left(5\,m_f^2+m_b^2\right) + m_{3/2}^2\left(m_f^4-m_b^4\right) + \left(m_f^2-m_b^2\right)^3\Big]\Big\} \\
&\quad + \frac{G^2}{24\,m_{3/2}^2 m_b^2 M_P^2}\Big\{\Big[m_{3/2}^4 - 2\,m_{3/2}^2\left(m_f^2-5\,m_b^2\right) + \left(m_f^2-m_b^2\right)^2\Big] \\
&\quad\times\Big[2\,\left(E\,F+E^*F^*\right)m_{3/2}m_f + \Big(|E|^2+|F|^2\Big)\Big(m_{3/2}^2+m_f^2-m_b^2\Big)\Big]\Big\} \\
&\quad + \frac{G}{6\,m_{3/2}M_P^2}\Big\{\left(DE^*+ED^*+CF^*+FC^*\right) \\
&\quad\times\Big[-2\,m_{3/2}^4 + m_{3/2}^2\left(m_f^2+m_b^2\right) + \left(m_f^2-m_b^2\right)^2\Big] \\
&\quad - 3\,(C\,E+D\,F+C^*E^*+D^*F^*)\,m_{3/2}m_f\Big(m_{3/2}^2-m_f^2+m_b^2\Big)\Big\}, \qquad \text{(B.3)}
\end{aligned}$$

where $C = V_{j1}$, $D = U_{j1}$, $E = -v_1 U_{j2}$, $F = -v_2 V_{j2}$ and $G = g$ for the $\tilde{\chi}_j^{\pm}$ final states; and $C = D = N'_{i2}$, with $N'_{i2} = -N_{i1}\sin\theta_W + N_{i2}\cos\theta_W$, $E = F = \frac{1}{\sqrt{2}}\left(-v_1 N_{i3} + v_2 N_{i4}\right)$ and $G = g/\cos\theta_W$ for the $\tilde{\chi}_i^0$ final states. In the above expression, the first and second lines come from the gauge part of eq. (2.14) (the third line), the third and fourth lines come from the matter part of eq. (2.14) (the second line), with the gauge bosons coming from the covariant derivative and the Higgs field ϕ taking its vacuum expectation value (see eq. (A.1)), and the rest of the lines come from the interference of these two parts. For $\widetilde{G} \to \tilde{f}\,f$, $\widetilde{G} \to \tilde{\chi_j}^{\pm}\,H^{\mp}$ and $\widetilde{G} \to \tilde{\chi}_i^0\,H_{1,2,3}^0$, we have:

$$\begin{aligned}
\overline{|\mathcal{M}|^2} &= \frac{1}{12\,m_{3/2}^2 M_P^2}\Big[\Big(|H|^2+|K|^2\Big)\Big(m_{3/2}^2+m_f^2-m_b^2\Big) - 2\,\left(H\,K+H^*K^*\right)m_{3/2}m_f\Big] \\
&\quad\times\Big[m_{3/2}^4 - 2\,m_{3/2}^2\left(m_f^2+m_b^2\right) + \left(m_f^2-m_b^2\right)^2\Big], \qquad \text{(B.4)}
\end{aligned}$$

where $H = K = \frac{1}{\sqrt{2}}\left(N_{i4}\sin\alpha + N_{i3}\cos\alpha\right)$ for the H_1^0 final state; $H = K = \frac{1}{\sqrt{2}}(N_{i4}\cos\alpha - N_{i3}\sin\alpha)$ for the H_2^0 final state; $H = -K = \frac{1}{\sqrt{2}}\left(N_{i4}\cos\beta + N_{i3}\sin\beta\right)$ for the H_3^0 final state; $H = U_{j2}\sin\beta$ and $K = V_{j2}\cos\beta$ for the $H^{\pm}$ final state; $H = U^*_{\widetilde{t}kR}$ and $K = U_{\widetilde{t}kL}$ for the $\widetilde{t}_k$ final state (and similarly for $\widetilde{b}_k$ and $\tilde{\tau}_k$ with their corresponding mixing matrices $U_{\tilde{b}}$ and $U_{\tilde{\tau}}$, respectively); $H = 0$ and $K = 1$ for all the $\tilde{f}_L$ and $\tilde{\nu}$ final states; and $H = 1$ and $K = 0$ for all the $\tilde{f}_R$ final states. To get the partial widths, one need to

multiply (B.4) by the phase-space factor:

$$\frac{N_c}{16\,\pi m_{3/2}^3}\sqrt{\left[m_{3/2}^2-(m_f-m_b)^2\right]\left[m_{3/2}^2-(m_f+m_b)^2\right]}\,, \tag{B.5}$$

where N_c is the color factor (3 for $q\,\tilde{q}$ channels, 8 for the $g\,\tilde{g}$ channel, and 1 otherwise).

The amplitude for the three-body decay $\widetilde{G}\to\tilde{\chi}_i^0\,\gamma^*\to\tilde{\chi}_i^0\,q\overline{q}$ is

$$\begin{aligned}\overline{|\mathcal{M}|^2} \;=\; & \frac{g^2\sin^2\theta_W Q_q^2}{3\,s^2 m_{3/2}^2 M_P^2}\left\{4\,s\,m_{\tilde{\chi}_i^0}m_{3/2}^3\left(N_{i1}'^2+N_{i1}'^{*\,2}\right)\left(s+2\,m_q^2\right)\right.\\
&+\;\left|N_{i1}'\right|^2\left[3\,m_{3/2}^6\Big(s+2\,m_q^2\Big)+m_{3/2}^4\Big(-3\,s\,(s+2\,t)+m_{\tilde{\chi}_i^0}^2\left(s-10\,m_q^2\right)\Big)\right.\\
&+\;m_{3/2}^2\Big(6\,s\,m_q^4+2\,m_q^2\big(-3\,s\,(s+2\,t)+2\,s\,m_{\tilde{\chi}_i^0}^2+m_{\tilde{\chi}_i^0}^4\big)\\
&+\;s\big(s^2+8\,st+6\,t^2-4\,m_{\tilde{\chi}_i^0}^2\,(s+2\,t)+3\,m_{\tilde{\chi}_i^0}^4\big)\Big)-\Big(s-m_{\tilde{\chi}_i^0}^2\Big)\Big(2\,s\,m_q^4-2\,m_q^2\\
&\left.\left.\times\big(2\,st+s\,m_{\tilde{\chi}_i^0}^2-m_{\tilde{\chi}_i^0}^4\big)+s\left(s^2+2\,st+2\,t^2-2\,m_{\tilde{\chi}_i^0}^2\,(s+t)+m_{\tilde{\chi}_i^0}^4\right)\Big)\right]\right\},\end{aligned} \tag{B.6}$$

where s and t are the invariant masses of the $q\overline{q}$ and $q\tilde{\chi}_i^0$ systems, respectively, $m_{\tilde{\chi}_i^0}$ is the mass of the neutralino $\tilde{\chi}_i^0$, where the LSP corresponds to $i=1$, and $Q_q=2/3$ or $-1/3$ for the corresponding quarks. The differential decay rate is

$$\frac{d\Gamma}{ds\,dt}=\frac{N_c}{256\,\pi^3 m_{3/2}^3}\;\overline{|\mathcal{M}|^2}. \tag{B.7}$$

These three-body and two-body analytic expressions were also given in [41] and [127].

For $\widetilde{G}\to\tilde{\chi}_i^0\,W^+W^-$, there are contributions from four generically different diagrams: contact, γ/Z exchange, $\tilde{\chi}_j^\pm$ exchange and H_1^0/H_2^0 exchange diagrams. The amplitude is too long to be listed here, so we just write the matrix elements for each of these diagrams (suppressing the polarization indices):

$$i\mathcal{M}_{\rm contact} \;=\; \frac{i}{4M_P}\,g\,\overline{u}(q')\,(P_R N_{i2}+P_L N_{i2}^*)\;\gamma^\mu\,[\gamma_\rho\,,\gamma_\sigma]\,\psi_\mu(p)\,\epsilon^{\rho\,*}(k)\,\epsilon^{\sigma\,*}(k')\,,$$

$$\begin{aligned}i\mathcal{M}_{\widetilde{G}\to\tilde{\chi}_i^0\gamma^*\to\tilde{\chi}_i^0 W^+W^-} \;=\; & \frac{i}{4M_P}\,\frac{1}{(k+k')^2}\,g^{\alpha\beta}g\sin\theta_W\,\overline{u}(q')\;\left(P_R N_{i1}'+P_L N_{i1}'^*\right)\;\gamma^\mu\\
&\cdot[\not{k}+\not{k}'\,,\gamma_\alpha]\,\psi_\mu(p)\times\Big[\left(2\,k+k'\right)_\sigma g_{\beta\rho}+\left(k'-k\right)_\beta g_{\rho\sigma}\\
&-\left(k+2\,k'\right)_\rho g_{\sigma\beta}\Big]\epsilon^{\rho\,*}(k)\,\epsilon^{\sigma\,*}(k')\,,\end{aligned}$$

$$
\begin{aligned}
i\mathcal{M}_{\widetilde{G}\to\tilde{\chi}_i^0 Z^*\to\tilde{\chi}_i^0 W^+W^-} &= \frac{i}{4M_P}\,\frac{1}{(k+k')^2-m_Z^2+im_Z\,\Gamma_Z} \\
&\quad\times\left(g^{\alpha\beta}-\frac{(k+k')^\alpha(k+k')^\beta}{m_Z^2}\right)g\cos\theta_W \\
&\quad\times\overline{u}(q')\Big\{\left(P_R N'_{i2}+P_L N'^{*}_{i2}\right)\gamma^\mu\left[\not{k}+\not{k}',\gamma_\alpha\right] \\
&\quad+\frac{\sqrt{2}\,g}{\cos\theta_W}\Big[P_R\left(-v_1N_{i3}+v_2N_{i4}\right) \\
&\quad+P_L\left(-v_1N^*_{i3}+v_2N^*_{i4}\right)\Big]\gamma^\mu\gamma_\alpha\Big\}\,\psi_\mu(p) \\
&\quad\times\Big[\left(2\,k+k'\right)_\sigma g_{\beta\rho}+\left(k'-k\right)_\beta g_{\sigma\rho} \\
&\quad-\left(k+2\,k'\right)_\rho g_{\beta\sigma}\Big]\epsilon^{\rho\,*}(k)\,\epsilon^{\sigma\,*}(k')\,,
\end{aligned}
$$

$$
\begin{aligned}
i\mathcal{M}_{\widetilde{G}\to W^+\tilde{\chi}_j^{-\,*}\to\tilde{\chi}_i^0 W^+W^-} &= \frac{i}{4M_P}\,\frac{1}{(p-k)^2-m^2_{\tilde{\chi}_j^\pm}+im_{\tilde{\chi}_j^\pm}\Gamma_{\tilde{\chi}_j^\pm}}\,g\,\overline{u}(q')\,\gamma_\sigma \\
&\quad\cdot\left[P_R O^R_{ij}+P_L O^L_{ij}\right]\cdot\left(\not{p}-\not{k}+m_{\tilde{\chi}_j^\pm}\right) \\
&\quad\cdot\Big\{\left(P_R V_{j1}+P_L U^*_{j1}\right)\gamma^\mu[\gamma_\rho\,,\not{k}] \\
&\quad+2g\left(P_R v_2 V_{j2}+P_L v_1 U^*_{j2}\right)\gamma^\mu\gamma_\rho\Big\}\,\psi_\mu(p)\,\epsilon^{\rho\,*}(k)\,\epsilon^{\sigma\,*}(k')\,,
\end{aligned}
$$

$$
\begin{aligned}
i\mathcal{M}_{\widetilde{G}\to W^-\tilde{\chi}_j^{+\,*}\to\tilde{\chi}_i^0 W^+W^-} &= -\frac{i}{4M_P}\,\frac{1}{(p-k')^2-m^2_{\tilde{\chi}_j^\pm}+im_{\tilde{\chi}_j^\pm}\Gamma_{\tilde{\chi}_j^\pm}}\,g\,\overline{u}(q')\,\gamma_\rho \\
&\quad\cdot\left[P_L O^{R\,*}_{ij}+P_R O^{L\,*}_{ij}\right]\cdot\left(\not{p}-\not{k}'+m_{\tilde{\chi}_j^\pm}\right) \\
&\quad\cdot\Big\{\left(P_L V^*_{j1}+P_R U_{j1}\right)\gamma^\mu[\gamma_\sigma\,,\not{k}'] \\
&\quad+2g\left(P_L v_2 V^*_{j2}+P_R v_1 U_{j2}\right)\gamma^\mu\gamma_\sigma\Big\}\,\psi_\mu(p)\,\epsilon^{\rho\,*}(k)\,\epsilon^{\sigma\,*}(k')\,,
\end{aligned}
$$

$$
\begin{aligned}
i\mathcal{M}_{\widetilde{G}\to\tilde{\chi}_i^0 H_1^{0\,*}\to\tilde{\chi}_i^0 W^+W^-} &= \frac{i}{2M_P}\,\frac{1}{(k+k')^2-m_{H_1^0}^2+im_{H_1^0}\Gamma_{H_1^0}}\,g\,m_W\cos(\beta-\alpha)\,g_{\rho\sigma} \\
&\quad\times\overline{u}(q')\left[P_R\left(\sin\alpha N_{i4}+\cos\alpha N_{i3}\right)\right. \\
&\quad\left.-P_L\left(\sin\alpha N_{i4}^*+\cos\alpha N_{i3}^*\right)\right]\gamma^\mu\left(\not{k}+\not{k}'\right)\psi_\mu(p)\epsilon^{\rho *}(k)\epsilon^{\sigma *}(k')\,, \\
\\
i\mathcal{M}_{\widetilde{G}\to\tilde{\chi}_i^0 H_2^{0\,*}\to\tilde{\chi}_i^0 W^+W^-} &= \frac{i}{2M_P}\,\frac{1}{(k+k')^2-m_{H_2^0}^2+im_{H_2^0}\Gamma_{H_2^0}}\,g\,m_W\sin(\beta-\alpha)\,g_{\rho\sigma} \\
&\quad\times\overline{u}(q')\left[P_R\left(\cos\alpha N_{i4}-\sin\alpha N_{i3}\right)\right. \\
&\quad\left.-P_L\left(\cos\alpha N_{i4}^*-\sin\alpha N_{i3}^*\right)\right]\gamma^\mu\left(\not{k}+\not{k}'\right)\psi_\mu(p)\epsilon^{\rho *}(k)\epsilon^{\sigma *}(k')\,,
\end{aligned}
\tag{B.8}
$$

where $\psi_\mu(p)$ represents the decaying gravitino with momentum p, $\overline{u}(q')$ represents the produced neutralino with momentum q', $\epsilon^{\rho\,*}(k)$ and $\epsilon^{\sigma\,*}(k')$ are the polarization four-vectors for the two W bosons with momenta k and k', respectively, $g^{\alpha\beta}$ is the flat-space Lorentz metric tensor, the Γ factors in the propagators are the total widths of the exchanged particles and $O_{ij}^L = N_{i2}V_{j1}^* - \frac{1}{\sqrt{2}}N_{i4}V_{j2}^*$ and $O_{ij}^R = N_{i2}^*U_{j1} + \frac{1}{\sqrt{2}}N_{i3}^*U_{j2}$. The Feynman rules for the vertices $W^+W^-H_{1,2}^0$ and $\tilde{\chi}_j^\pm\,\tilde{\chi}_i^0\,W^\mp$ are given in [10, 77]. The sum of the polarization states for gravitino is

$$
\begin{aligned}
\sum_{s=\pm\frac{3}{2},\pm\frac{1}{2}}\psi_\mu^s(p)\bar{\psi}_\nu^s(p) &= -\left(\not{p}+m_{3/2}\right)\left(g_{\mu\nu}-\frac{p_\mu p_\nu}{m_{3/2}}\right) \\
&\quad -\frac{1}{3}\left(\gamma_\mu+\frac{p_\mu}{m_{3/2}}\right)\left(\not{p}-m_{3/2}\right)\left(\gamma_\nu+\frac{p_\nu}{m_{3/2}}\right)\,,
\end{aligned}
\tag{B.9}
$$

and the phase space is the same as given in eq. (B.7).

A remark is in order for the process $\widetilde{G}\to\tilde{\chi}_i^0\,W^+W^-$. Because of the $1/m_W$ factors in the longitudinal polarization states of the W boson, one might worry that this process might have bad high-energy behavior. Correspondingly, if one restored the electroweak symmetry to make m_W vanish, then this process would diverge if there were still some terms proportional to negative powers of m_W in the final result. However, upon expanding the parameters in terms of m_W, that is, expanding the elements of chargino and neutralino mixing matrices N, U, V, the masses $m_{\tilde{\chi}_i^0}$, $m_{\tilde{\chi}_j^\pm}$, and the angle

α etc. (for the m_W dependence of these parameters, see, for example [128]), in the total amplitude, we have verified that all terms with negative powers of m_W cancel. As a result, this process has good high energy behavior. This is a highly non-trivial check on our calculation of the process $\widetilde{G} \to \tilde{\chi}_i^0 W^+ W^-$, verifying the relative magnitudes, signs and phases of all the individual contributions to the decay amplitudes.

We conclude by commenting on the differences between the amplitudes obtained and used here and those given [41] and [127], which are based on the gravitino interaction Lagrangian given in eq. (4.58) of [55]. This Lagrangian is different from that given in eq. (2.82) of [75], which we follow here. The latter reference uses the transformation from the two-component gravitino Lagrangian given in Wess and Bagger [8] to the four-component Lagrangian which, as pointed out at the footnote on page 205 of [10], requires a factor of i when one defines the Majorana spinors. This factor results in a sign difference when one writes down the Feynman rules using the matter part of the Lagrangian. We also note that our result for gravitino $\to Z + \chi$ differs from [127], in that it includes the Higgsino contribution.